DEVELOPMENT OF A PATIENT-SPECIFIC OCULAR MODEL FOR RISK ASSESSMENT OF GLAUCOMA DEVELOPMENT AND PROGRESSION

A thesis submitted in partial fulfillment of the requirement of

Nazarbayev University for the degree of

Doctor of Philosophy

by

Chingis Kharmyssov, MSc.

Supervisors

Yerkin G. Abdildin, Assistant Professor, PhD

Konstantinos Kostas, Assistant Professor, PhD

External Supervisors

Professor Christopher Kai Shun Leung. Chinese University of Hong Kong, Hong Kong, SAR

Professor Zaure A. Dzhumatayeva. Kazakh Research Institute of Eye Diseases, Department of Ophthalmology.

Acknowledgement

Firstly, I would like to thank my supervisors for providing their support and help in this journey. I wish to express my sincere appreciation to my lead supervisor, Prof. Yerkin Abdildin. I am deeply indebted to him for his patience, generous guidance and for his confidence in me over these past years. His stimulating questions helped me to form objective critique from multiple perspectives. I would like to thank my co-supervisor, Prof. Konstantinos Kostas, who has the substance of a genius. His insight and knowledge into the subject matter steered me through this research. Thanks for the meetings and conversations that were vital and inspiring me to think outside the box.

I would like to thank two my external supervisors, Prof. Zhumatayeva Zaure from KRIED and Prof. Leung Kai Shun Christopher from CUHK for their valuable input.

I would like to thank Prof. Luis Rojas, Prof. Prashant Jamwal and Prof. Jun Liu on my thesis examination committee for pointing out the original deficiencies of this work. Moreover, all the assistances from staff in the university are much appreciated.

Lastly, I would like to thank my family, for being supportive in every aspect of life. I always feel so blessed and lucky to have you all. I am also privileged to share my happiness with all my relatives and friends.

Abstract

Glaucoma is the leading cause of blindness worldwide. Once the retinal ganglion cell axons are lost they cannot be cured. Therefore, preventative risk assessment measures are important. To be able to perform these tasks, one needs to understand the mechanism behind the axonal blockage that leads to glaucoma. Biomechanical factors are thought to play a role in glaucoma, but the specific mechanism is not explored. In a Finite Element (FE) ocular model, the complex shape of the optic nerve components can be modeled and relevant mechanical quantities, such as stresses and strains due to intraocular (IOP) and/or intracranial (ICP) pressure, can be estimated and their effects assessed. Furthermore, optic nerve head (ONH) morphology and especially lamina cribrosa shape and properties, which are tightly linked to Glaucoma onset and development, vary greatly between individuals. This consequently suggests the development of patient-specific FE ocular models.

A method to generate patient-specific ocular models was contrived based on the geometry extracted from Optical Coherence Tomography (OCT) scans. Specifically, retinal layers were segmented using intensity and graph-based algorithms and the segmented layers were then reconstructed with a thin plate spline method. Finally, solid models were created from the reconstructed surfaces and meshed with tetrahedral elements. The geometric details of the generated ONH model correlate well with those of generic models from pertinent literature and special attention was paid to meshing so that the optic nerve region of the ocular model exhibits analysis-suitable element quality. The suggested reconstruction method is semiautomatic and although we aimed to fully capture the complete ONH region,

some anatomical structures, which are generally considered relevant and important, could not be extracted from OCT images *in vivo*. These include the pia arachnoid complex (dura mater and pia mater) that contains cerebrospinal fluid material and is considered to exert ICP. These were handled by carrying out a parametric analysis, using generic models with linear elastic material properties, to establish the degree of importance of the pia arachnoid complex. It was found that pia and dura mater properties can affect post laminar neural tissue and lamina cribrosa biomechanics. As it is currently infeasible to obtain high-quality patient-specific geometries for the pia arachnoid complex in vivo, we embed generic models of the pia and dura mater in our patient-specific ONH model. Viscoelastic material properties of dura mater and sclera were additionally retrieved from physical unidimensional tensile stress-relaxation tests. The influence of viscoelastic material properties at certain levels of ICP/IOP with a generic ocular model was examined, and results indicated, as expected, the importance of viscoelastic properties. Parametric analysis of patient-specific models was performed via the principal component analysis method deriving statistical shape models (SSM). Qualitative, quantitative and biomechanical assessments were performed with the aid of the generated SSM. For the biomechanical assessment, finite element modeling was employed and several patient-specific models, based on SSM shape modes, were generated and tested. We anticipate further enhancements and developments for this approach in the future.

Based on the so far obtained results, we find evidence that patient-specific, anatomically detailed 3D ocular models allow for a better understanding of employed biomechanics and can benefit glaucoma risk assessment.

Table of Contents

List of Abbreviations and symbols

RGC	Retinal Ganglion Cells
AMRSD	Automatic and Manual Relative Segmentation Difference
BMO	Bruch's Membrane Opening
CCT	Central Corneal Thickness
CSFP	CerebroSpinal Fluid Pressure
FEM	Finite Element Method
ICP	Intracranial Pressure
ILM	Internal Limiting Membrane
IOP	Intraocular Pressure
LC	Lamina Cribrosa
OHT	Ocular Hypertension
OCT	Optical Coherence Tomography

ONHSD	Optic Nerve Head Surface Depth
ONH	Optic Nerve Head
OPL	Outer Plexiform Layer
PC	Principal Component
PLCSD	Posterior Lamina Cribrosa Surface Depth
RPE	Retinal Pigment Epithelium
RSPP	Relative Segmentation Proportion Percentage
SAS	Subarachnoid Space
SD	Standard Deviations
SDOCT	Spectral Domain Optical Coherence Tomography
SSM	Statistical Shape Model
SVD	Singular Value Decomposition
TLPD	Translaminar Pressure Differences
TNRPE	Total Number of Retinal Pigment Epithelium
TRT	Total Retinal Distance

List of Figures

List of Tables

Chapter 1. Introduction

This chapter will introduce critical structures of human eye anatomy which are important to understand glaucoma. Brief characteristics of optic coherence tomography will be presented. It will also explain the concept of glaucoma where its clinical definitions and its causes will be explained. The thesis aims and list of published journal papers are also included.

1.1 Structure of the human eye

The human eye (Fig. 1) converts light signals into electrochemical impulses in neurons and ultimately, these are turned into three-dimensional, animated representations of our world with the help of our brains. Light passes through the cornea, anterior chamber, lens, the pupil, vitreous chamber and focuses onto the retina. Lamina cribrosa is a mesh-like structure of collagen fiber within the optic nerve head region that allows the optic nerve to pass through the sclera. The retina transforms the image into electrical neural impulses via the rod and cone cells and these are transmitted to our brain for vision generation. Retinal ganglion cells (RGC) convey visual signals to the brain through lamina cribrosa and via the axons that make up the optic nerve.

Three outer layers enclose the visual signal transmission areas and additional anatomical structures. The outer level is composed of sclera and cornea,

the middle one consists of iris, choroid, ciliary body and retinal pigment epithelium, while the inner level layer is the retina, which gets oxygenation from retinal vessels and choroid vessels.

Mammalian eyes have no bones and rigidity is maintained by the intraocular pressure (IOP). Specifically, the cornea and sclera form the corneoscleral shell which is under intraocular pressure and maintains the eye's firm shape and fixed volume. IOP is regulated with production and drainage of a watery, transparent fluid, called aqueous humor, through the trabecular meshwork. The corneoscleral shell acts like the balloon membrane and its mechanical behavior depends both on the material properties and its geometrical shape.

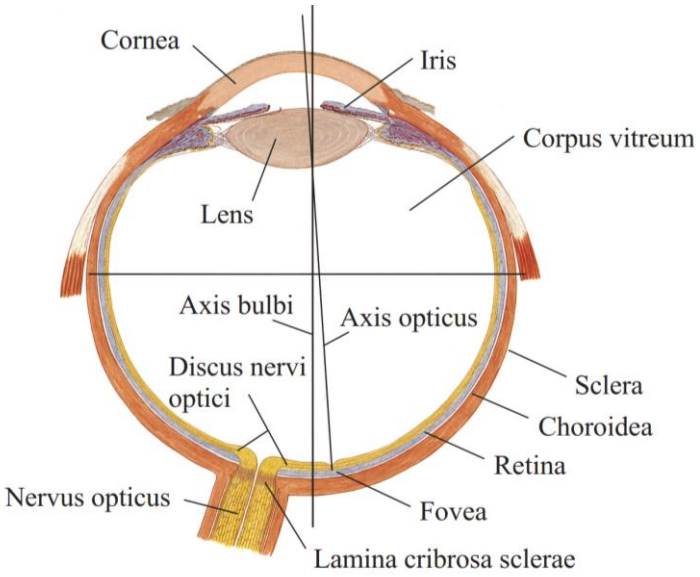

Figure 1. Human eye structure. Light enters through the cornea, passes through vitreous humor to retina. Optic nerve fibers transmit visual information to brain. The fibers converge in the optic nerve head and pass through lamina cribrosa. Reproduced from [6], [7].

1.1.1 Sclera

The sclera is the opaque white outer layer of the human eye containing mainly collagen fiber [1]. Its thickness is not uniform; assuming the maximum thickness at the back and decreasing gradually at the equator. The sclera is attached to the extraocular muscles and protectively balances internal and external forces and maintains the shape of the eye globe. Human sclera also performs functions facilitating rotation of the eyeball without distortion. Its rigidity is important to provide relatively constant conditions to keep intraocular pressure without fluctuations.

1.1.2 Lamina cribrosa

The human lamina cribrosa (LC) is a mesh-like semi-independent connective tissue structure located at the optic nerve head, which forms part of the eyewall separating intraocular pressure from intracranial pressure [2]. It mechanically supports and surrounds retinal ganglion cell axons that form the optic nerve exiting the eye. Glaucomatous nerve damage is generally believed as remodeling of the retinal ganglion cells and the death of the connective tissues at the LC [3]. Displacement and deformation of the LC have been associated with this effect which is the primary cause of glaucomatous optic neuropathy [4].

1.1.3 Cornea

The human cornea is a transparent tissue in the eye that measures approximately 10.5 mm vertically and 11.5 mm horizontally. It is the main

refractive element in the eye and also acts as a barrier to fluid and pathogens. The cornea is avascular since transparency is of prime importance. Nutrients are transported via aqueous humor from the inside surface and tear from the outside surface. It borders with the sclera through the corneal limbus and forms the corneoscleral shell.

1.2 Glaucoma

A group of eye disease, called glaucoma may lead to the development of progressive visual field loss and end with blindness. It is considered an optic neuropathy associated with the death of a substantial number of axons and retinal ganglion cells in the retina [5]. Relevant structural change can be visualized with ophthalmoscopy by comparing the optic cup to the overall disc size ratio; see Fig. 2A, B. Association with this disorder is made when at least one eye exhibits visual field loss or optic disc damage, i.e., having functional or structural deficits. Retinal ganglion cell nerve fiber thinning is a sign of structural loss of axons. The progress of glaucoma leads to blindness and affect significantly patient's quality of life.

Early detection of glaucoma and understanding its pathogenesis is the principal motivation in pertinent research works, including the work presented in this thesis. As mentioned before, glaucoma is a leading eye disease than can lead to blindness. It has been estimated that the number of people affected by glaucoma will increase from approximately 76 million people today (2020) to 111.8 million

people by 2040 [6]. The risk of being affected depends on race and ethnicity, e.g., African American subjects had substantially higher glaucoma prevalence (23.2% to 9.4%) over Caucasian subjects of the same age group (over 75 years old) in the USA [7, 8]. The Barbados Eye Study identified peak prevalence in the black population were among 50 years or older, one in eleven, and one in six among 70 years or older, had glaucoma [9].

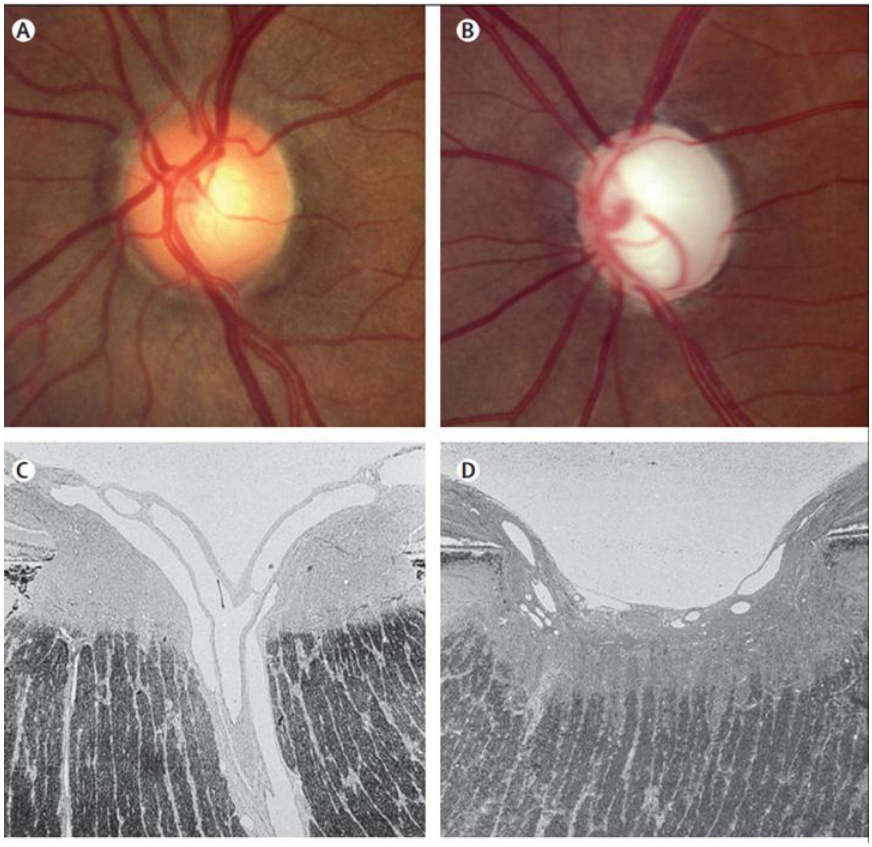

Figure 2. A) Optic disc image, acquired via ophthalmoscopy, of A) an individual without glaucoma and B) a glaucoma patient. In B) the glaucomatous optic cup occupies a higher proportion of the disc, the optic disc rim fades, and the optic cup deepens. C) Histological image of the normal optic nerve head. D) Histological image of glaucomatous optic nerve head with deep optic cup and tissue loss. Reproduced from [13].

Glaucoma can be classified into open-angle, closed-angle (or angle-closure) and normal-tension glaucoma (NTG). The mechanism of open-angle glaucoma is believed to be the slow exit of aqueous humor through the trabecular meshwork, while in closed-angle glaucoma the iris blocks the trabecular meshwork. Normal-tension glaucoma shows all the characteristics of "traditional" glaucoma except one: the elevated intraocular pressure. These types can be further divided into primary and secondary, with secondary types referring to the ones caused by other pathologic causes. Primary open-angle glaucoma (POAG) refers to the situations where the outflow of aqueous humor is hindered as a result of the open iridocorneal angle. Primary angle-closure glaucoma (PACG) refers to the state in which iris blocks aqueous outflow leading to gradual or acute eye pain and vision loss. In both types of glaucoma, there is no significant difference in optic disc topography, although visual field damage is more diffuse in PACG [10]. An exhaustive review of glaucoma management is out of the scope of this Ph.D., as the work contained in this thesis aims to evaluate biomechanical characteristics of human subject's ONH.

1.3 The role of intraocular and intracranial pressure

Intraocular pressure (IOP) is the fluid pressure inside the globe and abnormal levels constitute a principal risk factor for the development of glaucoma. IOP varies between 10-21mmHg and averages to 15 mmHg in most populations [11]. In the past, elevated values of IOP was a constituent part of glaucoma definition [12], which, however, was later changed and it is no longer considered an essential

finding [13]. Many subjects with elevated IOP (more than 21 mmHg) may not develop glaucoma [14]. This state is referred to as ocular hypertension (OHT). In other cases, as mentioned before for normal-tension glaucoma, patients may have normal IOP levels (less than 21mmHg) but still develop glaucoma. Despite this variation in its correlation to the disease, IOP still seems to play a central role in the development of glaucoma. Therefore, researchers and medical professionals work on its reduction pharmaceutically or surgically due to its importance [15]. The work contained within this thesis focuses on studying ocular hypertension and normal-tension form of glaucoma since it has been suggested that the optic nerve biomechanical structure of an individual may dictate safe levels of IOP [16].

Furthermore, large IOP fluctuations in subjects with glaucoma have led researchers to examine additional factors affecting disease appearance and development [17]. It has been well established that biomechanical, biological and vascular factors determine an individual's susceptibility to the disease [18]. Optic nerve head separates areas with intraocular pressure, intracranial pressure, and the central nervous system; see Fig. 3. Many studies have demonstrated that intracranial pressure may also play a role in the disease [19]. A case-control study reported that ICP is lower than average values in cases with normal-tension glaucoma and may be elevated in hypertension patients [20]. Lamina cribrosa (LC) is sensitive to such pressures and fluctuations which lead to adverse effects for the rest of the ocular region.

The difference between cerebrospinal fluid pressure, which largely defines retrolaminar tissue pressure, and the intraocular pressure occurs across the

LC [21]. It is well known that elevated intracranial pressure influences the occurrence of intracranial hypertension, normal-tension glaucoma, and papilledema. c. The sectional shape of the complex system in the SAS varies along its length with the widest section found near the ocular globe (Fig. 4) [22]. Dura mater lies external and pia mater lies internal to the SAS.

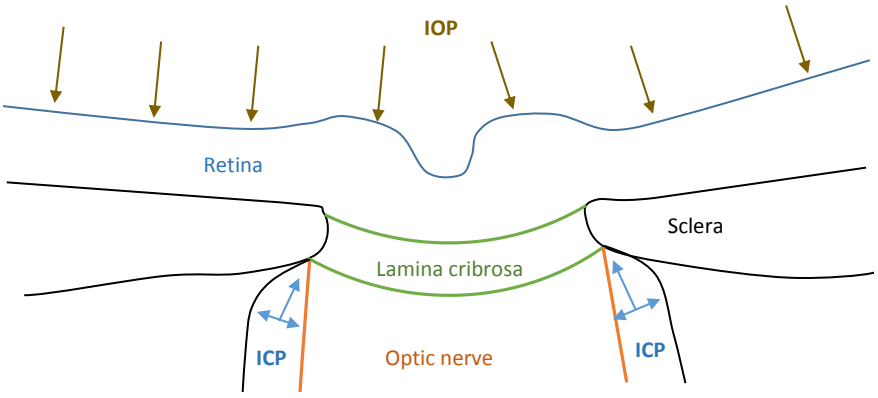

Figure 3. Optic nerve head diagram showing areas with intracranial pressure (ICP - blue) and intraocular pressure (IOP - brown). ICP acts circumferentially in the subarachnoid space while IOP acts on the retina.

Although IOP increases with age for several individuals, this does not mean that elderly people with high IOP will have glaucoma [23]. However, the proportion flowing out through these systems in humans and primates is unknown (Fig.4). Cerebrospinal fluid pressure (CSFP) is pulsatile in nature, having a small phase difference with IOP. CSFP is out of sync with IOP having a peak slightly before the ocular pulse [24]. IOP levels are rather stable and independent of posture, while CSFP levels depend on it, e.g., an increase of 2 to 4mmHg can be measured when a sitting person lies down [25].

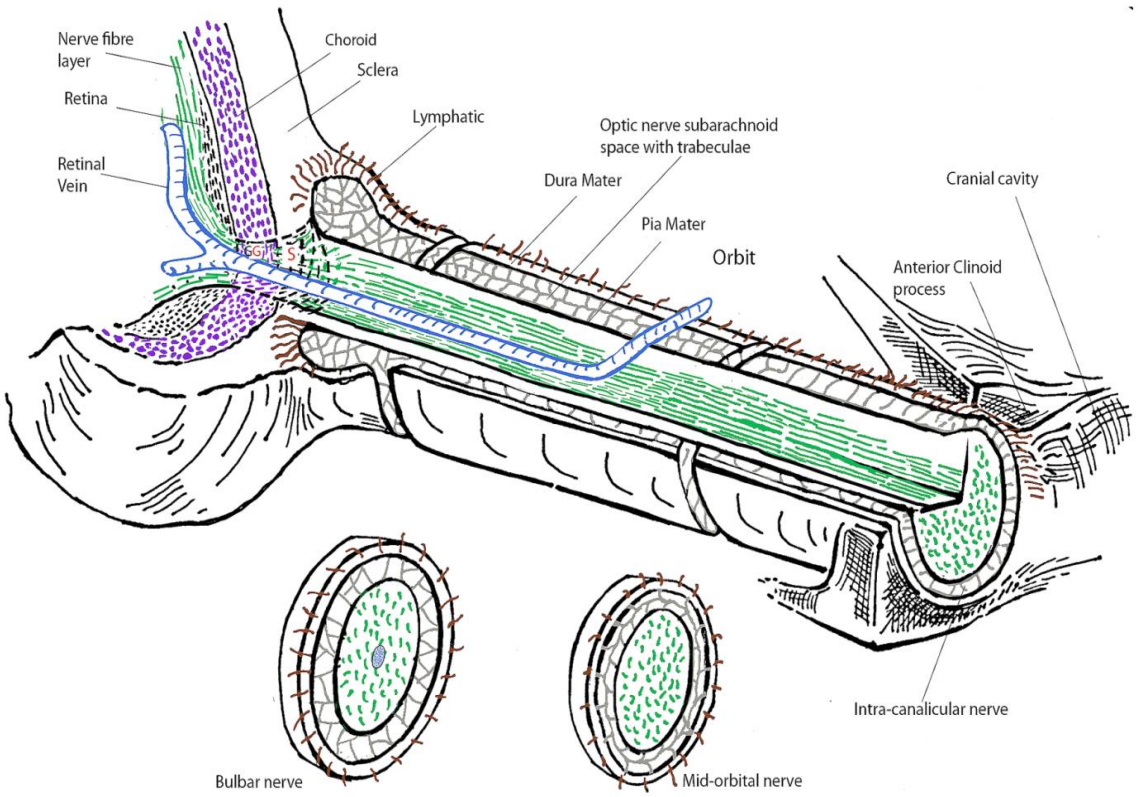

Figure 4. Optic nerve head key anatomic structures in relation to subarachnoid space. Scleral and glial lamina cribrosa are marked with S and G, respectively. Reproduced from [28].

Studies have demonstrated that increased ICP may play a protective role against glaucoma progression as it may lead to a compensating effect across lamina cribrosa [20, 26]. For example, in hypertensive subjects, high ICP can counterbalance IOP keeping translaminar pressure difference low. Contrarily, in cases of normal tension glaucoma patients, high ICP can lead to a high-pressure difference at lamina cribrosa, making the eye prone to glaucoma appearance and progression; see Fig. 3 for the regions that ICP and IOP are exerted. Further investigation is required to understand how ICP acts in hypertension and normal tension glaucoma and whether it plays truly a protective or disruptive role,

respectively. Finite element modeling is well-established and can help researchers to characterize biomechanics of the ONH and potentially the interaction between ICP and IOP in the same area.

1.4 Optical coherence tomography

Optical Coherence Tomography (OCT) is a non-invasive imaging technique using low-coherence interferometry to produce two- and three-dimensional images of biological tissues. It was first introduced in 1991 [27] and it has since developed rapidly with the relevant market exhibiting significant growth. In vivo imaging of optic nerve head including lamina cribrosa is now possible with OCT.

Initial OCT devices implemented A-scans[1] that can operate in time and frequency domain [27]. Time-domain OCT, which was implemented earlier, performs depth scans moving scanning reference mirror and photodetector with a limited scanning speed of 400Hz; see Fig. 5. Spectral-domain OCT uses an interferometer with a spectrometer that can separate spectral components with static scanning reference mirrors; see Fig. 6. This improved data acquisition speed and resolution compared to the initial version of the OCT described in [27]. c

[1] A-scan is one-dimensional (one column of image) OCT image where sum of A scans will become B-scan

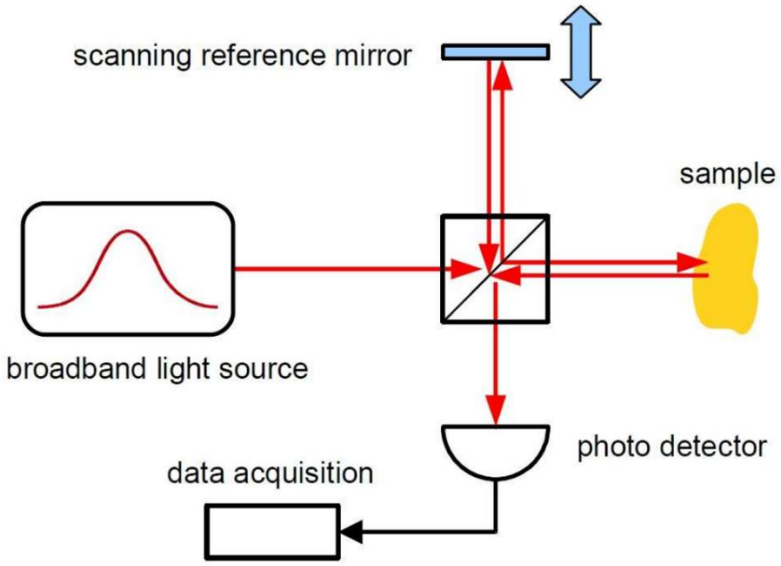

Figure 5. Time-domain OCT system based on backscattered and reflected light. Adapted from [27].

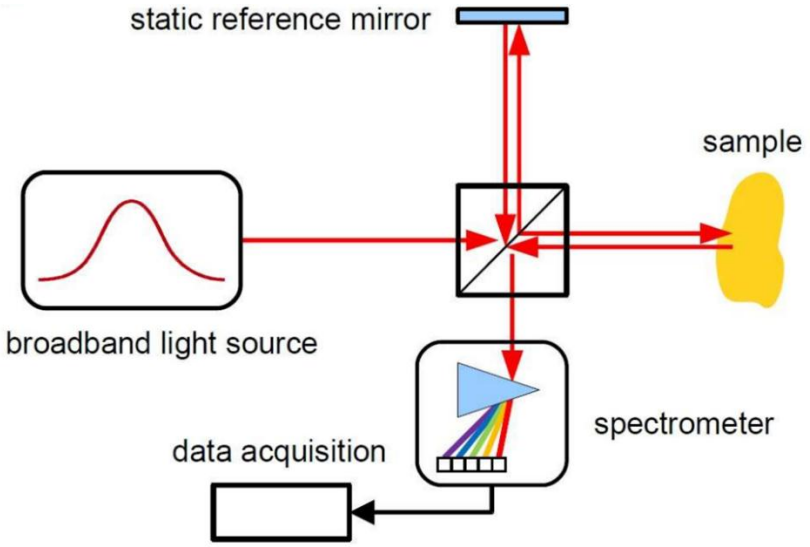

Figure 6. Spectral-domain OCT. Adapted from [27].

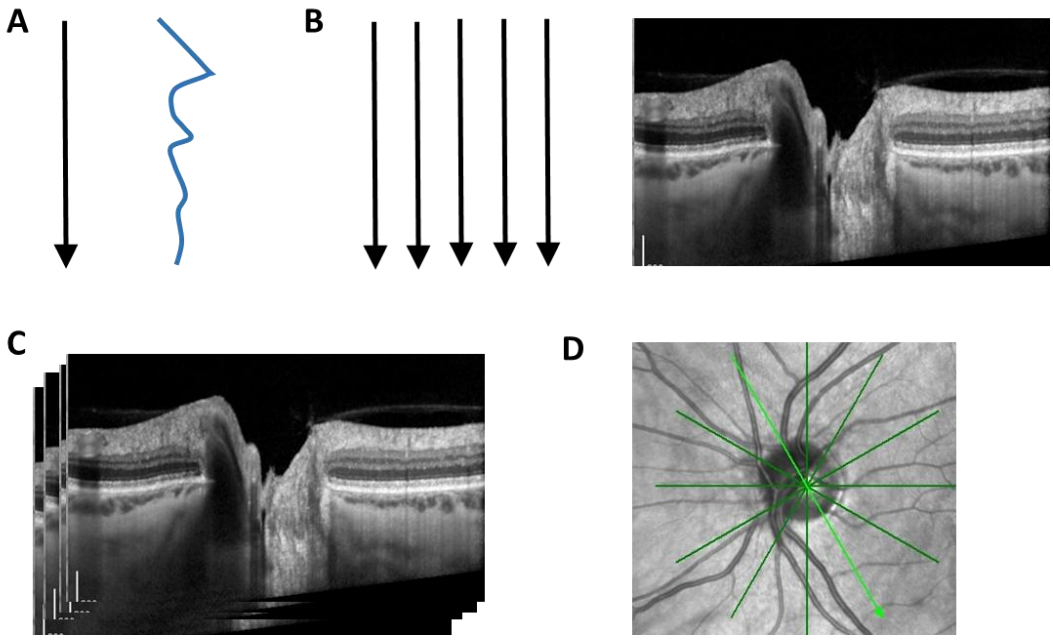

Figure 7. Diagram of the scan acquisition process used in this study. A) A-scans represent a one-dimensional depth scan. Blueline shows a graphical representation of the reflectivity profile along the beam axis. B) B-scan of ONH cross-section, a linear collection of A-scans. C) A series of B-scans form a 3D volume. D) Top view of the generated 3D volume

1.5 Thesis aims

This work aims to study the effect of geometric and material properties in ONH biomechanics using generic and patient-specific ocular models. Intracranial pressure was also included since it was hypothesized that it can also play an important role, especially for hypertensive and normal-tension glaucoma subjects. We hypothesized that ICP levels may affect IOP's effects and deformations in lamina cribrosa. To test this hypothesis, we split our work into four sub aims, described below:

Aim 1: Perform parametric analysis with generic 3D ocular models and study the effect of intracranial pressure on hypertensive subjects. Numerous studies have suggested that ICP and mechanical properties of the ONH may influence the optic nerve head's biomechanical behavior. However, mechanical stresses and exact conditions causing optic nerve damage due to such influences are not well known. Understanding how these mechanical properties and pressure levels can influence glaucomatous damage requires a systematic characterization. In this context, a generic model can be initially used to perform the corresponding parametric analysis. The effect of cornea characteristics is also included in the study since it was hypothesized that cornea plays an important role in patients with ocular hypertension.

Aim 2: Develop and evaluate an automated method for ONH segmentation and analysis. Due to the complexity in ONH/retinal layers, manual segmentation can be both time-consuming and error-prone since a certain degree of subjectivity is introduced by the person processing the images. In this context, we aim to develop and validate an automated segmentation and quantification method for ONH layers, which will reduce processing time and remove subjectivity from the procedure. Further to this, it will allow us to easily develop patient-specific ocular models and permit the examination of potential effects of patient-specific geometry.

Aim 3: Characterize the effect of intraocular (IOP) and intracranial pressure (ICP) on the optic nerve head (ONH) and their correlation to patient-specific geometric

characteristics. In this part, we employ the proposed algorithm from Aim 2 the aforementioned segmentation method to reconstruct patient-specific ONH models and embed them into the generic cornea-scleral shell from Aim 1. The patient-specific models are compared to the generic model developed initially and the effects of IOP and ICP are also assessed for patient-specific geometries.

Aim 4: Perform parametric analysis with patient-specific optic nerve head geometry embedded into the generic corneoscleral shell using a statistical shape model. Finally, we aim to develop statistical shape models using the patient-specific data delineated in Aim 2. Biomechanical assessment using the statistical models is also performed.

Published journal articles:

1) **Kharmyssov, C.**, Ko, M. W. L., & Kim, J. R. (2019). Automated segmentation of optical coherence tomography images. Chinese Optics Letters, 17(1), 011701.

2) **Kharmyssov, C**., Abdildin, Y. G., & Kostas, K. V. (2019). Optic nerve head damage relation to intracranial pressure and corneal properties of the eye in glaucoma risk assessment. Medical & biological engineering & computing, 1-13.

Chapter 2. Literature review

This chapter will introduce the basic principles of optic nerve head biomechanics and its relation to glaucoma. It will also explain modeling approaches used by the pertinent research community to understand the glaucoma mechanism.

2.1 Optic nerve head biomechanics

Biomechanics refers to the study of biological systems using mechanical principles. ONH is of particular interest for its weak structure is surrounded by the strong cornea-scleral shell. Furthermore, lamina cribrosa is the primary site of damage to the optic nerve where RGC axons are blocked in glaucoma [28] and is reasonable to assume that biomechanics of the ONH play an important role in the onset and development of the disease. In the sequel, we briefly present the mechanics principles and relevant definitions that are employed in our work.

Stress is defined as the ratio of load/force across a "small" surface element over the area of that element. Stresses can vary from region to region due to surface geometry and/or non-uniform loads, and the same is true for biological tissues [29]. Stresses can generally have any direction relative to the surface of application and are commonly decomposed into normal (compression and tension) and tangential stress (shear). Being derived from a fundamental physical quantity (force/) and a purely geometrical quantity (area), stress is also a fundamental quantity that can

be quantified and analyzed without explicit consideration of the nature of the material or its physical causes.

Strain is a measure of local deformation, induced commonly by stresses, on a "small" surface element. Strains can be also decomposed into shear (parallel deformation concerning the surface element) and normal (perpendicular to the surface element) components. The amount of stretch or compression along material line elements or fibers is the normal strain, and the amount of distortion associated with the sliding of plane layers over each other is the shear strain, within a deforming body. This could be applied by elongation, shortening, or volume changes, or angular distortion. Depending on the amount of strain, or local deformation, the analysis and measurements may require significantly different handling. Large strain theory is commonly employed when the undeformed and deformed configurations of the continuum are significantly different, which is typically the case when elastomers, plastically-deforming materials, and other fluids and biological soft tissue are considered. On the other hand, small strain theory is commonly applied to cases where deformed and undeformed configurations of the continuum can be assumed identical, e.g., the common mechanical strain used in examining steel or concrete bodies.

Stresses and strains are different quantities and are related to each other through constitutive equations, e.g., Hooke's law, which depends on relevant material properties such as the ability of a tissue to resist deformation under applied force [30]. Material properties are dependent on fiber orientation (isotropic anisotropic behavior), linearity or nonlinearity (concerning the deformation and

load relationship) and time-dependency of deformation (e.g., viscoelastic vs elastic materials).

The relationship between biomechanics and glaucoma can be explained by how RGC axons and supporting tissues (endothelial cells, astrocytes, glia), connective tissue pathophysiology (lamina cribrosa, scleral canal wall, and peripapillary sclera) is influenced by IOP-related strains and stresses within ONH [18, 31, 32]. A conceptual framework of ONH as a biomechanical structure was proposed in [18]; see Fig. 8. This framework assumes that IOP-related stresses and strains influence ONH blood flow and the delivery of nutrients through connective tissues. Non-IOP related factors such as retro-bulbar determinants of ONH blood flow and inflammatory or autoimmune insults can damage ONH within normal IOP [29].

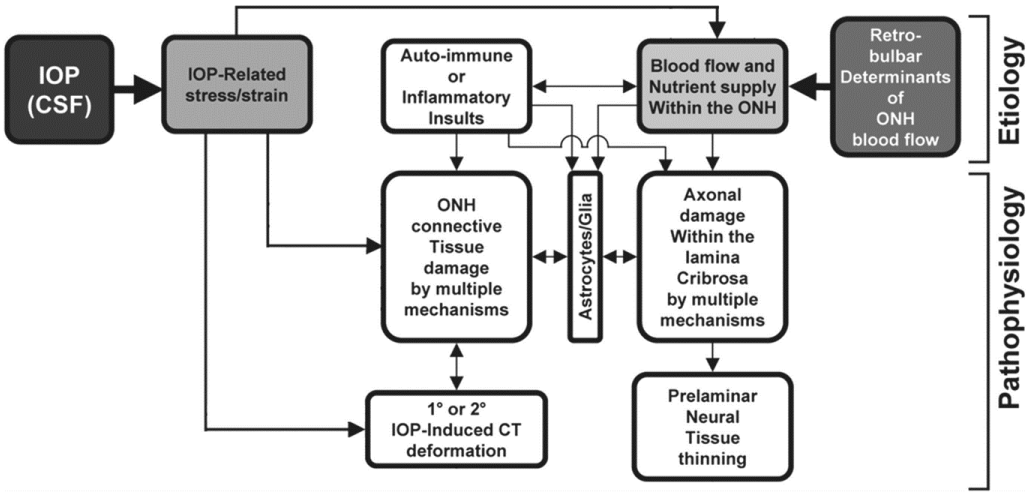

Figure 8. The biomechanical theory of glaucoma.

Adapted from [18].

Geometric and material properties may play a role in an individual's susceptibility to glaucoma. Blood flow pressure within lamina cribrosa capillaries is

also a likely factor that influences the distribution of nutrients to astrocytes. The response of glia and astrocytes to strain may also be important within the biomechanical environment. Aging is also a factor in ONH biomechanics. It was proposed that older connective tissues are commonly stiffer than younger ones [33]. In an aged patient, stiff lamina becomes more resistant to higher strain. However, as a result, its trabeculae may also become brittle.

IOP is regulated by vessels with outflow and inflow facilities normal to the surface of the eyewall generating circumferential stresses. The main burden of keeping this stress which is also called "hoop stress" is taken by the sclera. Peripapillary sclera mainly regulates lamina cribrosa connective tissue biomechanics. The stress generated by translaminar pressure is fifteen times less than the hoop stress, which is the difference between IOP in ONH and cerebrospinal pressure [34].

The study of the biomechanical environment is complicated due to several characteristics of ocular tissues. For instance, the three-dimensional morphology of lamina cribrosa is subject-specific and regionally complex [35–38]. Sclera thickness may differ in various regions from the equator to the peripapillary [39]. Lamina cribrosa, cornea, and sclera have complex elastin and collagen fiber orientation. Therefore, mathematical and experimental material characterization is complex. Lamina cribrosa and sclera material and geometric properties are also connected to pathologic and age-dependent factors.

2.2. Modelling Biomechanics, the influence of sclera

Modeling approaches are divided into numerical and analytical. A detailed description of analytical methods in biomechanics is beyond the scope of this thesis, however, a brief description is provided here. In analytical models, stresses and strains are estimated directly by corresponding mathematical expressions. Laplace's law is the simplest version of such models that have been employed to describe the mechanics of the sclera and cornea. The Laplace relation: $\sigma = IOP\ R/(2h)$ estimates wall stress as a function of wall thickness (h), the radius of the sclera (R) and pressure (IOP) in a thin vessel [40]. The same law has been adapted to explain the biophysics of hollow organs and the mechanics of cardiac chambers [41]. Another approach is based on ocular rigidity, which relates to the change in IOP with intraocular volume changes [42]. This approach is useful for calculating pulsatile ocular blood flow from IOP pulsations. However, due to complex geometry and varying material properties of the ONH, these analytical models fail to provide accurate and detailed estimations, since several prerequisites, such as homogeneity, hollowness, etc. are not satisfied. Therefore, due to complexity and variance in ONH geometry and material properties, most researchers have switched to numerical methods.

The most common numerical method employed in the determination of the complex eye mechanical structure is the finite element method (FEM). It allows computing deformations of an object, if its geometry, material properties, and loading are known. Both generic and patient-specific models have been used to

study ocular biomechanics with FEM. The introduction of the general finite element modeling approach in this area occurred in Bellezza et al. [34]. Specifically, a generic eye model was used to study the relationship between IOP and IOP-related stresses within ONH. Bellezza et al. [34] found that stresses within connective tissues of the ONH can be high even at low IOP values. More extensive work was then performed by Sigal et al. in [43] with a more realistic generic model that incorporated pia mater, pre/post laminar neural tissue, and retinal vessel. They found that strain in lamina cribrosa may contribute to the development of glaucomatous optic neuropathy and that lamina cribrosa behavior depends strongly on sclera properties. A schematic illustration of the influence of sclera on ONH deformations is shown in Fig. 9. In the case of the stiff sclera, an increase in IOP induced posterior bowing of the lamina cribrosa. A compliant sclera exhibited large deformations. Systematic analysis with a generic model was later performed by Sigal et al. in [30] to study geometric and material properties that affect ONH biomechanics. They used 21 input factors in their generic model and quantified effects via a set of 29 outcome measures including strain within each tissue. Five input factors had the highest influence in the following order: sclera stiffness, eye radius, Young's Modulus for lamina cribrosa, IOP and sclera thickness. This study was performed using a single parameter at a time method, however, it was the first study that highlighted the importance of sclera. Sigal et al. then extended this work with simultaneous systematic analysis of material and geometric properties using finite element modeling in [44]. They found that ONH deformation is mostly

affected by sclera stiffness and that sclera's thickness plays an important role when sclera is compliant.

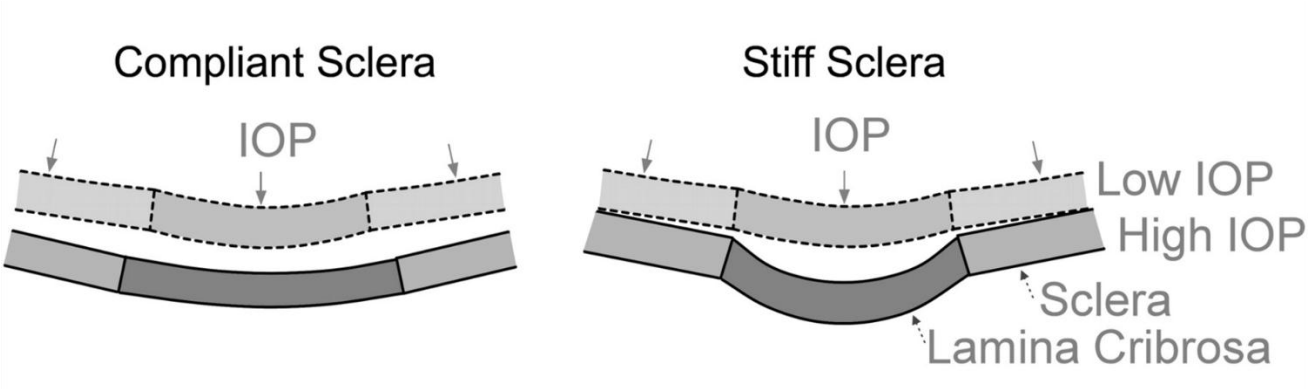

Figure 9. A schematic illustration of the effect of sclera on ONH biomechanics. Adapted from Sigal et al. [45]

In [46], Girard et al. studied peripapillary and posterior sclera orientation with a hyperelastic and anisotropic generic model. Collagen fiber orientation was described with a fiber concentration factor. Results showed that meridional fiber orientation in sclera increased scleral canal expansion, whereas the opposite was observed with circumferential fiber organization. Perez et al. [47] used also a generic model to simulate viscoelastic effects of sclera and cornea to investigate factors due to micro volumetric changes, without however including the ONH. The viscoelastic properties of sclera and cornea, which include relaxation time constants, equilibrium modulus, instantaneous modulus, were varied to study the effect of IOP at different rates of volumetric changes. The results showed that the relative significance of a parameter was highly dependent on the rate of change and the profile of dynamic IOP was mostly influenced by viscoelastic properties. They concluded that it is important to characterize the ocular shell using viscoelastic properties. Ayyalasomayajula et al. [48] developed a generic porohyperelastic model

of the human eye to study changes in the permeability of trabecular meshwork, Bruch's choroid complex, sclera, and uveoscleral pathway. They found that lamina cribrosa strain decreased when tissue permeability increased. This has opened a new dimension for studies since tissue porosity and permeability were identified to play a role in understanding glaucoma.

Patient/Subject-specific ocular models have been also developed to study ONH biomechanics. Sigal et al. [49, 50] have developed subject-specific models from ex vivo subjects to explore more accurately strains in ONH. They found that sclera stiffness was again the most important factor in ONH biomechanics, which supported the findings using the generic model [43, 45]. Norman et al. [51] created a subject-specific cornea-scleral shell with generic ONH to characterize the effects of sclera differences. Results showed that decreased thickness of peripapillary sclera increased lamina cribrosa strains.

An important experimental measurement of collagen microstructure including an inverse finite element model was done by Coudrillier et al. in [52]. They developed a specimen-specific anisotropic sclera model with generic lamina cribrosa. Results showed that the peripapillary sclera region produces significant changes in the ONH deformation. This was not the case for mid posterior sclera, which can be modeled as isotropic. Campbell et al. [53] created generic models with specimen-specific connective tissue beams of the lamina cribrosa imaged with micro-computed tomography. They compared non-homogeneous and homogeneous laminae cribrosae and found that anisotropy in the connective tissue beams has little effect on deformation. Zhang et al. [54] studied the effect of circumferential

fiber organization of peripapillary sclera and concluded that this type of organization is effective in reducing deformation in lamina cribrosa. Voorhees et al. [55] proposed a tangential collagen fiber organization that has a biomechanical advantage over circular collagen organization; see Fig. 10.

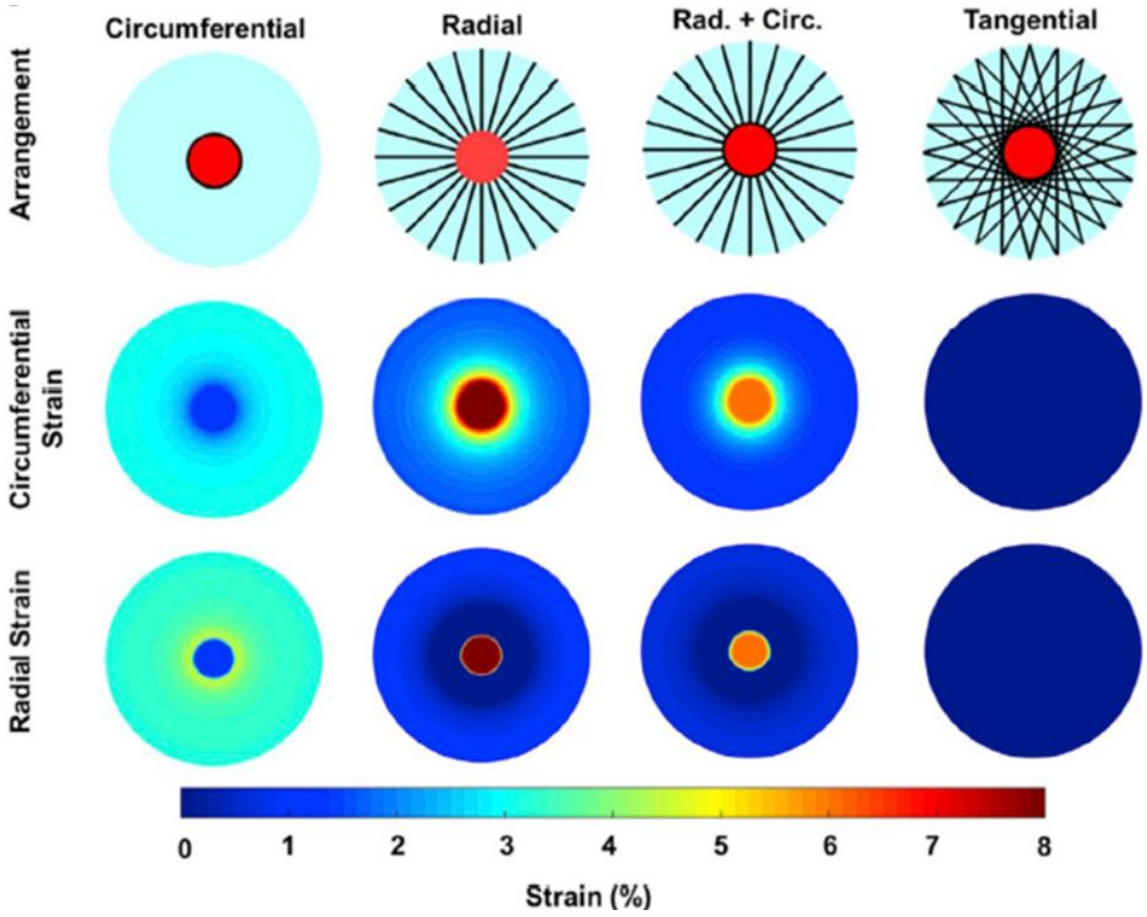

Figure 10. Four simulated collagen fiber orientations. Black lines correspond to collagen fibers. Tangential fiber organization exhibited the best biomechanical response leading to lower lamina cribrosa deformation. Adapted from Voorhees et al. [55]

Chapter 3. Effect of intracranial pressure and cornea in ocular hypertension

In this chapter, the results of numerical simulations of the biomechanics of the optic nerve head (ONH) during exposure to elevated intraocular (IOP) and/or intracranial pressure (ICP) with generic models are presented. A variety of geometric and material properties and their association with higher IOP and ICP values were studied simultaneously. Such experiments were conducted on an improved eye model of 3D geometry and visualization, which enables the reaction of the human eye to be captured realistically. Our primary concern was to quantify the potential damage to ONH that can result from a shear failure by calculating the affected ONH fraction. In addition to the potential role of Central Corneal Thickness (CCT) in clinical evaluation and treatment in patients with ocular hypertension (OHT) the findings show a significant role of ICP in the post laminar neural tissue failure. In particular, at an early stage of eye damage, CCT was established as influencing ONH, and the scleral modulus in the lama cribrosa in specific OHT conditions appears to result in lower shear failures. Such findings suggest that CCT tests can be used in OHT patients as a screening method for glaucoma.

3.1 Introduction

Optic nerve head biomechanics are believed to play a role in glaucoma [56]. Lamina cribrosa (LC) is a collagenous meshwork where optic nerves pass through to the brain [57, 58]. Retinal dysfunction is believed to occur primarily in the site of LC [57]. Cerebrospinal fluid continuously surrounds post-laminar neural tissue and exerts pressure on them and meninges. Retinal ganglion cells pass though LC and post-laminar neural tissue where the cerebrospinal fluid pressure exerted.

Intraocular pressure is one of the main factors affecting axonal bundles in the LC to shear and bow sclera posteriorly as shown by experiments [59]. Optic neuropathy caused by high IOP values that affect optic nerve head biomechanical environment [60, 61], however, Ocular Hypertension (OHT) subjects do not have signs of glaucoma event with an elevated level of IOP [18] [62].

Glaucoma is related to biomechanical properties of the eye including and not limited to cornea [63]. Central Corneal Thickness (CCT) is one of the geometric properties of the cornea, which may also be used to determine glaucoma [64]. CCT may play an important role in ocular hypertension patients for glaucoma risk assessment[65]. Corneal Elasticity (CE) has also demonstrated its protective function against pressure rises due to IOP [63].

Although the cornea is located far from LC, which is the main site of concern in glaucoma, biomechanical properties of the cornea are related to the stiffness and thickness of sclera, which is believed to be one of the main key factors in ONH

biomechanical environment [30]. Hence, it is necessary not to underestimate the importance of corneal biomechanical properties.

Computational models were used to test IOP's biomechanical effect on glaucoma to ONH [19, 30]. To characterize the sensitivity of ocular biomechanics to glaucoma, a better comprehension of IOP and its interrelations with ICP and corneal biomechanical properties is required. The contribution of this chapter is twofold: a) the effect of corneal biomechanical properties on ONH biomechanical responses in association with acute IOP elevations for OHT conditions were studied, and b) the effect of increased ICP and IOP on ONH's biomechanical environment was characterized.

3.2 Material and methods

3.2.1 Ocular geometry

This analysis involves comparing a set of eyeball models with various geometric and material properties where the finite element (FE) method was used in their assessment. An axisymmetric three-dimensional eyeball (see Figure 11) was constructed in Solidworks 2017 (Dassault Systemes, SolidWorks Corporation, Concord, MA) using dimensions for its constituting components from pertinent literature [30, 66]. Table 1 contains the complete set of measurements and material properties used together with references. The model was then imported to ANSYS 15 (ANSYS, Canonsburg, PA) and automatically meshed. The mesh was refined in

the ONH region until the results' convergence; the final values are in agreement with Sigal's [45] study.

This model is an extended version of the ocular model developed by Leung et. al [66] which also included dura to study the influence of ICP on the optic nerve. Scleral shell thickness of the globe is assumed 0.8 mm with a 12 mm internal radius and attenuated tapering down to 0.4 mm at canal with an angle of 30 degrees from the vertical axis; see Figure 11. The eye globe and adipose tissue are assumed axisymmetric around the central axis of the LC. The adipose tissue is set to cover 140 degrees of the sclera and is modeled with a thickness of 4.6 mm [67, 68].

The thickness of lamina cribrosa is set at 0.3 mm while the radius of the anterior surface is set at 0.9 mm as described in [30]. LC is constructed as a spherical shell section and concentric to the scleral shell. The region beneath LC - post-laminar neural tissue is modeled using a taper angle of 80 degrees from the horizontal axis [30]. The PLNT starts with a retinal shell thickness of 0.24 mm and ends up with 0.2 mm at the equator while following the contour extracted from image data published in [69].

The dura mater and pia mater thicknesses are assumed to be 0.255 mm and 0.06, respectively [19]. The geometry of the subarachnoid space meets the same image data [69] with a thickness of 0.15 mm [19] between dura and pia. The study did not include the elastic component of the pia-arachnoid substance, as it is generally considered extremely soft [70]. The central retinal artery is modeled according to the literature [19] to include the effect of blood pressure. The vessel is

modeled as a tube with an external wall diameter of 0.18 mm and 0.05 mm for its thickness [19].

Cornea geometric and material properties were set according to average population values [71]: diameter at 11 mm, curvature radius at 7.8 mm and central corneal thickness at 0.5 mm [71]. Blindspot is located 15 degrees nasally from the fovea and therefore angle between ONH central axis and corneal central axis was set to 165 degrees [72].

Table 1. Summary of ocular model parameters used for the eyeball model in the FEA code.

Parameters	Unit	Baseline value	Sources/References
Retinal thickness	mm	0.24	[30]
LC radius (at canal)	mm	0.9	[30]
LC depth below rim axis	mm	0.1	[69]
LC thickness at axis	mm	0.3	[30]
Pia mater thickness	mm	0.06	[73]
Distance between pia and dura mater	mm	0.15	[19]
Dura mater thickness	mm	0.26	[19]
Vessel external diameter	mm	0.35	[19]
Vessel wall thickness	mm	0.05	[19]
Corneal radius of curvature	mm	7.8	[74]
Corneal diameter	mm	11	[71]
Central corneal thickness	mm	0.5	[71]
Central retinal artery wall thickness	mm	0.05	[19]
Central retinal artery outer diameter	mm	0.18	[19]
Subarachnoid space gap	mm	0.15	[19]
Optic nerve angle	deg	80	[30]
Canal wall angle to the vertical	deg	30	[30]
Peripapillary rim height	mm	0.3	[30]
IOP	mmHg	15	[19]
BP	mmHg	50	[69]
ICP	mmHg	15	[19]
CDR	-	0.45	[75]
Poisson's ratio of all materials	-	0.49	[30]
Elastic modulus of cornea	MPa	0.29	[76]
Elastic modulus of pia mater	MPa	3	[30]
Elastic modulus of prelaminar neural tissue	MPa	0.03	[30]
Elastic modulus of post-laminar neural tissue	MPa	0.03	[30]
Elastic modulus of adipose tissue	MPa	0.047	[67, 68]
Thickness of adipose tissue	mm	0.46	[67, 68]
Elastic modulus of dura mater	MPa	9	[19]
Elastic modulus of artery	MPa	5	[69]
Elastic modulus of sclera	MPa	3	[19]
Elastic modulus of lamina cribrosa	MPa	0.3	[30]

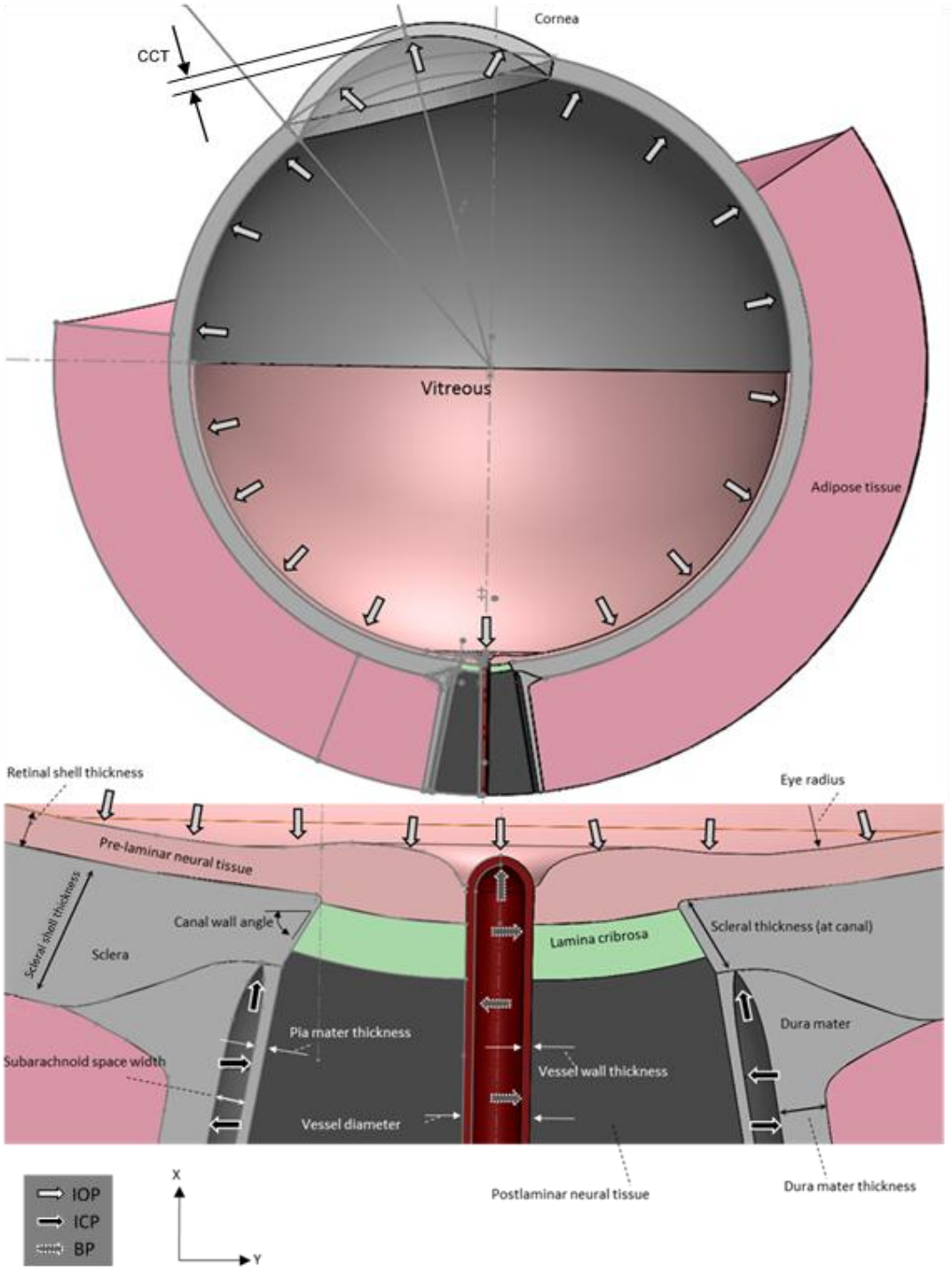

Figure 11. FE model geometry. Bottom: Zoom-in view of the optic nerve head region with definitions. Top: the whole eyeball model geometry. See Table 1 for input parameters.

All tissues are assumed to be homogeneous, isotropic, incompressible and linearly elastic. The baseline material properties were adapted for each tissue as following as shown in Table 1: 5 MPa for artery, 9 MPa for dura mater, 3 MPa for pia mater, 0.29 MPa for cornea, 0.047 MPa for adipose tissue, 0.03 MPa for post-laminar and prelaminar neural tissues [30, 67–69, 76].

3.2.2 Fractional factorial designs of experiments method

Taguchi method [77] which is a fractional factorial design method was employed to perform parametric analysis for screening the most important factors affecting lamina cribrosa deformation and stress at two levels. Taguchi method used to optimize several experiments to reduce the experimental data set without losing the efficiency of the factor analysis. More complex experimental design methods can be used in the future, such as Doehlert matrix (DM), central composite designs (CCD) and three-level designs such as the Box-Behnken design (BBD) for further characterization of the significant factors [78–80]. However, here we use Taguchi factorial design with two levels for multiple factors to perform a screening test in which our major concern is to identify the important factors without any detailed analysis.

The ocular model 's sensitivity to many factors such as material and geometrical qualities of its subcomponents was evaluated against greater levels of IOP and ICP. Particularly, a two-level orthogonal matrix layout ($L_{16}(2)^{14}$) with fourteen factors was used, causing sixteen various cases gained by Statistica (v13.3, StatSoft) application package. ($L_{16}(2)^{14}$) is an orthogonal matrix design which may

be represented as a two-dimensional array, in which all of the input factors show up in numbers that are equal in every vertical column as well as disperse equally the pairwise combinations [81]. Here, sixteen denotes the number of instances, fourteen the number of elements and two corresponds to the amount levels. This approach enables screening of a lot of variables as well as attaining fine estimates of every factor 's outcome with a moderately small study case set.

Table 2. Geometric and material properties were used as input factors. Baseline value with its high and low-level values used in the Taguchi experimental design.

	Input factor description	Baseline value	Low Level -20% value (Level 1)	High Level +20% value (Level 2)
Geometry				
A	Scleral thickness at canal, mm	0.4	0.32	0.48
B	Lamina cribrosa radius (at canal), mm	0.95	0.76	1.14
C	Lamina cribrosa thickness, mm	0.3	0.24	0.36
D	Pia mater thickness, mm	0.06	0.048	0.072
E	Dura mater thickness, mm	0.255	0.204	0.306
F	Central corneal thickness, mm	0.5	0.4	0.6
G	Retinal thickness, mm	0.2	0.16	0.24
Material property				
H	Sclera modulus, MPa	3	2.4	3.6
I	Lamina cribrosa modulus, MPa	0.3	0.24	0.36
J	Prelaminar neural tissue modulus, MPa	0.03	0.024	0.036
K	Pia mater modulus, MPa	3	2.4	3.6
L	Dura mater modulus, MPa	9	7.2	10.8
M	Cornea modulus, MPa	0.29	0.232	0.348
N	Post-laminar neural tissue modulus, MPa	0.03	0.024	0.036

Table 2 summarizes fourteen input factors used with the finite element analysis. The input factors represent two separate groups. The first group includes material properties and the second group shows geometric properties. The seven material properties are scleral modulus (H), LC modulus (I), prelaminar neural tissue modulus (J), pia mater modulus (K), dura mater modulus (L), corneal modulus (M), and post-laminar neural tissue modulus (N). Geometric properties are scleral thickness at the canal (A), LC radius (B), LC thickness (C), pia mater thickness (D), dura mater thickness (E), central corneal thickness. The corneal material and geometric properties are included as reported in the literature [69]. The range of the sensitivity was set to vary by ±20% from the baseline values.

3.3 Criteria for optic nerve damage

Optic nerve damage is mostly linked to shear stresses as shown in [59, 82]. Experiments show that optic nerve damage is mostly caused by shear stresses in lamina cribrosa periphery caused by mechanical forces [59]. Tresca failure criterion was initially used by Leung et al. [66] where they reasonably studied the effect of ocular stiffening due to age on optic nerve damages. The effect of radial oriented fibrils in the LC periphery reinforced the LC against transversal shear stresses is widely studied by the computational remodeling approach [83, 84]. Therefore, in this chapter, we are calculating ONH possible damage with peak maximum shear stress values in optic nerve and lamina cribrosa. Table 3 shows the calculated peak maximum shear stresses in the LC and PLNT influenced by fourteen input factors in the sixteen case studies. Classical shear Tresca failure criterion was employed to

carry nerve damage prediction [66, 85]. More complex damage models that account for age dependence, nerve fiber anisotropy could be added, but as a first criterion, the classical Tresca criterion appears to be sufficient since it modeled observed behavior [66]. The nerve is categorized as damaged when local maximum shear stress in lamina cribrosa exceeds threshold value. In mild ocular hypertension (LC modulus: 0.12 MPa, cornea modulus: 0.17 MPa, sclera modulus: 1.84 MPa, IOP: 21 mmHg) nerve damage is negligible [66]. The peak maximum shear stress in lamina cribrosa was 0.0032 MPa (τ_{max}) at ocular hypertension, thus, the Tresca criterion (τ_c) was taken so that τ_{max} does not exceed τ_c (0.0035 MPa). The number of nodes with MSS values higher than 0.0035 MPa is represented as LC shear failure and defined as the fraction of failure nodes over the total amount of nodes.

IOP of 15 mmHg is applied to the internal surface of sclera and cornea, the external surface of prelaminar neural tissue for the base model. Constant arterial pressure of 55 mmHg of constant arterial pressure was applied to the vessel. 15 mmHg of intracranial pressure was applied to the subarachnoid complex space [86]. These values correspond to a normal adult human.

3.4 Results and Discussion

Table 3 clearly shows that shear stresses in a relatively soft PLNT are considerably lower than corresponding values observed in a relatively stiff lamina cribrosa for all sixteen cases. The peak MSS in PLNT ranges from 0.0261 MPa to

0.0476 MPa, whereas MSS in LC is generally is much higher and varies from 0.2205 MPa to 0.5365 MPa.

Two-factor level results are collectively depicted in Table 4. K_n (n=1, 2) corresponds to the average of eight values for each factor of the peak MSS for each factor level shown in Table 3. K_2 represents the effect of a high level (i.e. +20%) and K_1 represents the effect of low level (i.e. -20%) eight values of each factor.

As an example, for input factor B, $K_1 = 0.3879$ is an average of the peak MSS values in LC corresponding to B = 0.76 in Table 3. Range value, *R,* is the difference between K_1 and K_2 for each factor. Large *R*-values signify factors with great influence on the peak MSS in LC or PLNT. Sensitivity analysis results are depicted in Figure 12, where *R*-values are plotted for each factor. Elastic moduli of LC and PLNT had the highest *R*-values, and, therefore, can be considered the most influential parameters among the selected factors. On the other hand, one may observe that although CCT is the sixth influential factor in LC, it comes second when considering PLNT shear stresses.

3.4.1 Effect of intracranial pressure

Cerebrospinal fluid pressure was identified as an important parameter which mostly affects post laminar neural tissue [87]. Figure 13 depicts the results of calculations of maximum shear stresses in lamina cribrosa and post laminar neural tissue at a constant IOP value of 15 mmHg. The figure reveals that higher ICP

values have a beneficial effect on the whole range of LC modulus values. On the other hand, elevated levels of ICP induce extra stresses on PLNT, which is consistent with observations from the literature [19]. Shear stresses in LC with increasing modulus were lower in ICP values of 15 mmHg, whereas shear stress values were higher when the ICP value was 7 mmHg (Figure 13, a). ICP of 15 mmHg induced extreme shear stresses in PLNT leading to the more dominant effect of ICP than its stiffness (Figure 13, b) which is consistent with findings in pertinent literature [69].

Table 3. Assignment of 14 input factors in an orthogonal array and calculated peak maximum shear stress in the lamina cribrosa (LC) and post-laminar neural tissue (PLNT).

	Input factors														Peak maximum shear stress (MPa)	
Case no	**A**	**B**	**C**	**D**	**E**	**F**	**G**	**H**	**I**	**J**	**K**	**L**	**M**	**N**	**LC**	**PLNT**
1	0.48	1.14	0.24	0.072	0.204	0.4	0.24	2.4	0.24	0.036	2.4	10.8	0.348	0.024	0.2607	0.0357
2	0.48	1.14	0.24	0.072	0.204	0.4	0.24	3.6	0.36	0.024	3.6	7.2	0.232	0.036	0.3570	0.0370
3	0.48	1.14	0.24	0.048	0.306	0.6	0.16	2.4	0.24	0.036	3.6	7.2	0.232	0.036	0.2708	0.0445
4	0.48	1.14	0.24	0.048	0.306	0.6	0.16	3.6	0.36	0.024	2.4	10.8	0.348	0.024	0.3161	0.0325
5	0.48	0.76	0.36	0.072	0.204	0.6	0.16	2.4	0.36	0.024	2.4	10.8	0.232	0.036	0.5037	0.0398
6	0.48	0.76	0.36	0.072	0.204	0.6	0.16	3.6	0.24	0.036	3.6	7.2	0.348	0.024	0.3026	0.0313
7	0.48	0.76	0.36	0.048	0.306	0.4	0.24	2.4	0.36	0.024	3.6	7.2	0.348	0.024	0.5365	0.0363
8	0.48	0.76	0.36	0.048	0.306	0.4	0.24	3.6	0.24	0.036	2.4	10.8	0.232	0.036	0.2877	0.0440
9	0.32	1.14	0.36	0.072	0.306	0.4	0.16	3.6	0.24	0.024	2.4	7.2	0.348	0.036	0.3326	0.0410
10	0.32	1.14	0.36	0.072	0.306	0.4	0.16	2.4	0.36	0.036	3.6	10.8	0.232	0.024	0.4061	0.0346
11	0.32	1.14	0.36	0.048	0.204	0.6	0.24	3.6	0.24	0.024	3.6	10.8	0.232	0.024	0.2205	0.0261
12	0.32	1.14	0.36	0.048	0.204	0.6	0.24	2.4	0.36	0.036	2.4	7.2	0.348	0.036	0.3730	0.0367
13	0.32	0.76	0.24	0.072	0.306	0.6	0.24	3.6	0.36	0.036	2.4	7.2	0.232	0.024	0.3820	0.0320
14	0.32	0.76	0.24	0.072	0.306	0.6	0.24	2.4	0.24	0.024	3.6	10.8	0.348	0.036	0.3274	0.0411
15	0.32	0.76	0.24	0.048	0.204	0.4	0.16	3.6	0.36	0.036	3.6	10.8	0.348	0.036	0.4125	0.0476
16	0.32	0.76	0.24	0.048	0.204	0.4	0.16	2.4	0.24	0.024	2.4	7.2	0.232	0.024	0.3507	0.0349

Table 4. Range analysis for the peak maximum shear stress (MSS) in the (LC) and post-laminar neural tissue (PLNT)

Input factors	Peak MSS in the LC (%)			Peak MSS in the PLNT (%)		
	K_1	K_2	R	K_1	K_2	R
A	0.3506	0.3544	0.0038	0.0367	0.0376	0.0009
B	0.3879	0.3171	0.0708	0.0386	0.0360	0.0026
C	0.3346	0.3703	0.0357	0.0382	0.0362	0.002
D	0.3460	0.3590	0.013	0.0378	0.0366	0.0012
E	0.3476	0.3574	0.0098	0.0361	0.0382	0.0021
F	0.3680	0.3370	0.031	0.0389	0.0355	0.0034
G	0.3619	0.3431	0.0188	0.0383	0.0361	0.0022
H	0.3786	0.3264	0.0522	0.0379	0.0364	0.0015
I	0.2941	0.4109	0.1168	0.0373	0.0371	0.0002
J	0.3681	0.3369	0.0312	0.0361	0.0371	0.001
K	0.3508	0.3542	0.0034	0.0371	0.0373	0.0002
L	0.3631	0.3418	0.0213	0.0367	0.0377	0.001
M	0.3473	0.3577	0.0104	0.0366	0.0378	0.0012
N	0.3469	0.3581	0.0112	0.0329	0.0415	0.0086

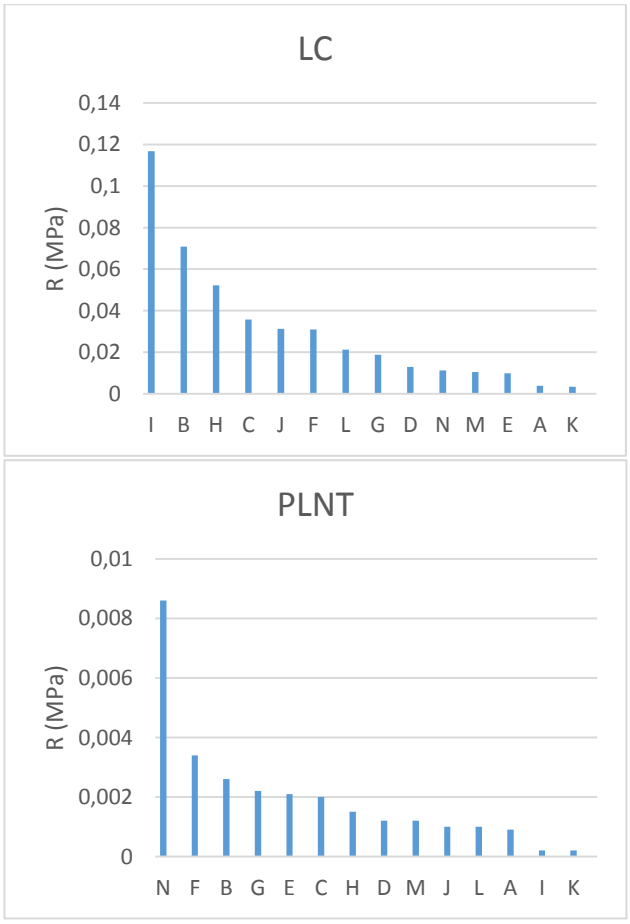

Figure 12. Pareto chart of peak maximum shear stress (MSS) in lamina cribrosa (LC) and post-laminar neural tissue (PLNT) concerning selected input factors:

A-scleral thickness at the canal (mm), B- lamina cribrosa radius (at canal) (mm),

C-lamina cribrosa thickness (mm), D- pia mater thickness (mm),

E- dura mater thickness (mm), F- the central corneal thickness (mm),

G- the retinal thickness (mm), H- sclera modulus (MPa),

I-lamina cribrosa modulus (MPa), J- prelaminar neural tissue modulus (MPa),

K- pia mater modulus (MPa), L- dura mater modulus (MPa),

M- cornea modulus (MPa), N- post-laminar neural tissue modulus (MPa).

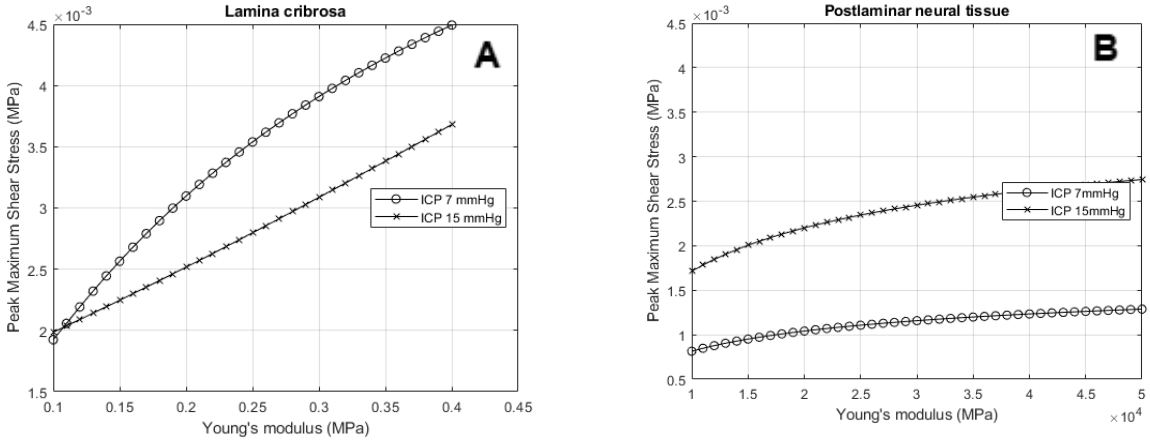

Figure 13. Effects of variation in ICP (7 mmHg and 15 mmHg) on peak maximum shear stress as a function of stiffness for a) LC and b) PLNT at a constant IOP value of 15 mmHg.

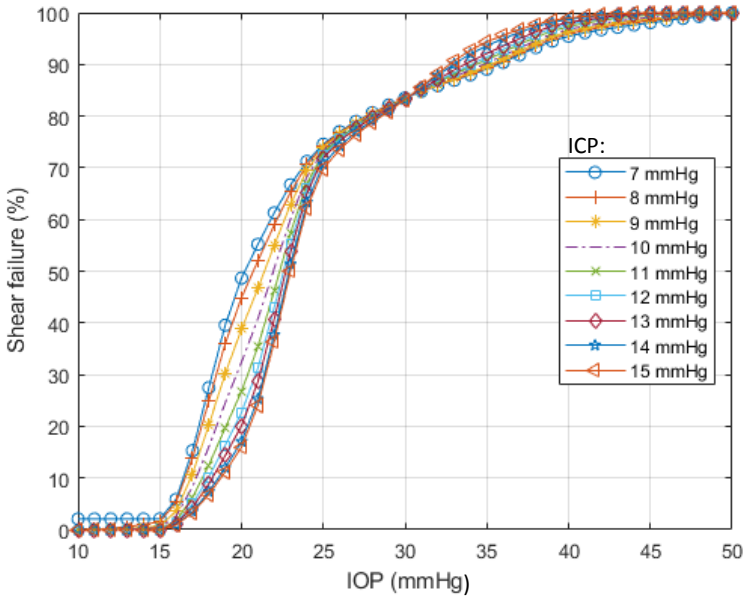

Figure 14. Effect of variations in intraocular pressure (IOP) on shear failure in lamina cribrosa (LC) at different intracranial pressures.

Shear failure values in lamina cribrosa for various values of IOP and ICP, in hypertension condition, are depicted in figure 14. At IOP level of 20 mmHg and when ICP level drops from 15 mmHg to 7 mmHg the LC shear failure increased from 17% to 48%. In this case, it shows that ICP may play a counter-pressure role against IOP. High translaminar pressure or the pressure difference in the lamina cribrosa is caused by abnormally low ICP (7mmHg) and resulted in higher shear failure. This finding is consistent with the case-control study [88], which included over 6000 subjects and compared ICP in patients with and without glaucoma, revealed that ICP was higher (12.6 ± 0.85 mmHg) in subjects with OHT than in age-matched control group (10.6 ± 0.81 mmHg). Contrary, similar observations of a prospective study by [89] found that ICP measures were significantly lower in normal-tension glaucoma subjects.

The influence of ICP on LC shear failure is also examined at increased corneal, scleral and LC moduli; see Figures 15 and 16. The elastic modulus values for lamina cribrosa vary between 0.12 and 0.67 MPa, while the cornea elastic modulus takes values in the range of 0.17 and 1.43 MPa (Figure 15). Finally, the modulus values for sclera are between 1.84 to 3.72 MPa. These biomechanical property values are adopted from pertinent literature [90]. As we may observe in Figure 15, shear failure exhibits a decrease with increasing ICP values for corneal modulus values between 0.31 MPa and 0.73 MPa, with a higher reduction of around 12% occurring at a corneal stiffness of 0.31 MPa. Increasing ICP values have a reverse effect on higher corneal modulus values, i.e., shear failure increases.

However, in this range of higher-valued moduli, the ICP-influence is less prominent, and the estimated shear failure is high even with low ICP values.

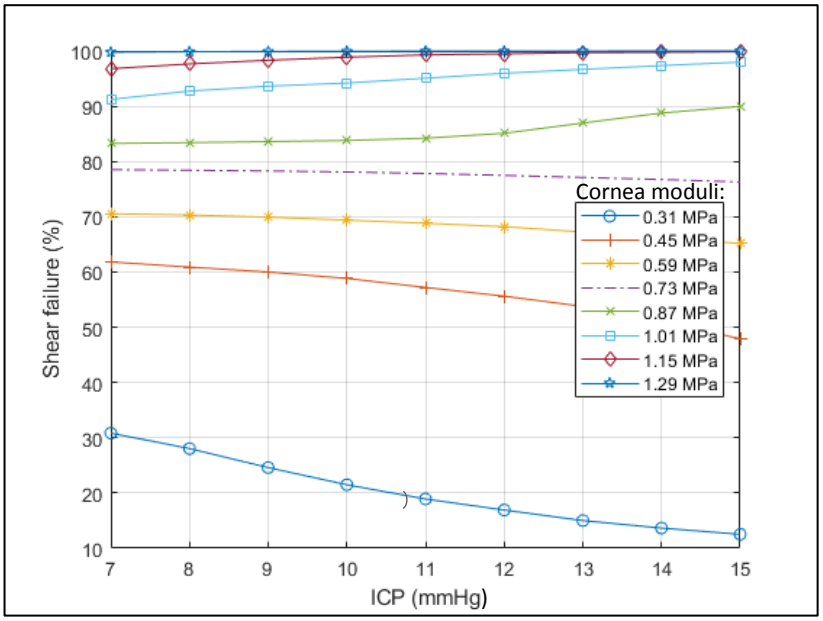

Figure 15. Effect of intracranial pressure (ICP) on shear failure in lamina cribrosa. Elastic modulus of cornea varies from 0.31 MPa to 1.29 MPa.

3.4.2 Effect of central corneal thickness

Brandt et al. [91] recruited 1636 patients and compared central corneal thicknesses in participants with and without glaucoma. They found that primary open-angle glaucoma subjects had thinner cornea whereas patients with ocular hypertension had thicker corneas. In our study, we also tried to identify the conditions in which corneal thickness plays a significant role. Specifically, we examined shear failure for corneal thicknesses between 0.4 mm and 0.6 mm at a constant IOP value of 25 mmHg. At the same time, we tested varying levels of Sclera thickness, LC radius at the canal, LC Young's modulus to establish the

conditions that render CCT's role more important. LC shear failure value for each case was calculated, and results are summarized for all examined cases in Table 5.

Table 5. Effect of CCT variation at a different range of factors on LC shear failure.

Factors	±20% range	CCT = 0.4 mm	CCT = 0.6 mm	Deviation (%)
		LC shear failure (%)		
LC Young's modulus, MPa	0.24	9.87	13.20	33.74
	0.36	73.73	74.02	0.39
LC radius (at canal), mm	0.76	46.14	46.17	0.07
	1.14	45.30	46.60	2.87
Sclera Young's modulus, MPa	2.4	63.85	62.95	1.41
	3.6	23.17	28.00	20.85
Sclera thickness, mm	6.4	70.88	71.24	0.51
	9.6	21.29	21.30	0.05

It is easy to see that CCT value affects LC shear failure significantly in the presence of the lower LC modulus value and the high-valued sclera modulus. Another interesting observation in the same table can be made for scleral stiffness' effect on LS shear failure. As can be seen in Table 6, when we consider a greater value for sclera's modulus, the expected shear failure percentage is significantly reduced to at least half the value attained with a softer sclera. Experimental studies [92] back up this evidence as they also reveal a beneficial effect of the stiffened sclera in reducing LC strain at increased IOP. Finally, Norman et al. (2010) reported that glaucomatous eyes appear to have thinner sclera when compared with normal eyes, and this is in agreement with our results, which show high LC shear failure in lower sclera thicknesses; see last two rows in Table 5.

To better illustrate the effect of two CCT values (0.6 mm and 0.4 mm) on LC shear failure, we plot LC shear failure as a 3D surface concerning sclera and lamina cribrosa moduli values; see Figures 16 a, b, which correspond to CCT values of 0.6

and 0.4 mm, respectively. Figures 16c corresponds to shear failure surfaces shown in Figure 16a while Figure 16d corresponds to 16b. Both figures (Figs. 16 c, d) depict a top view of the corresponding shear failure surface along with its isolines. In these figures, one may easily observe that the 10% to 70% isolines are shifted upwards for the larger CCT value and that the transition area between low and high failure rates is generally narrower when compared to the case of low-valued CCT. Hence, stiffer sclera and LC will generally protect the eye and especially for the case of a thicker cornea.

A thicker cornea allows us to remain in the "safe area" for a wider range of LC and sclera moduli, whereas a thinner cornea shrinks this range; see Fig. 16c,d. For example, with a sclera modulus of 8MPa, the LC modulus can vary from 0.1 to 0.4MPa with shear failure remaining below 10% for the thicker CCT (0.6mm). On the other hand, and for the same sclera modulus, the thinner CCT (0.4mm) allows a significantly smaller LC modulus variation, i.e., between 0.1-0.3MPa. It can be also seen in Figs. 16c,d that the shear failure is estimated at 10% for a CCT=0.6mm when LC and sclera moduli are 0.45 and 9MPa, respectively, whereas at CCT=0.4mm the shear failure increases to 40% for the same LC and sclera moduli. This indicates that thinner central cornea can be hazardous and may lead to glaucoma development and progression. This is in agreement with the ocular hypertension treatment study by Gordon et al. [93] where participants with POAG had thinner central corneal thickness. However, one may observe that the deviation between the isolines for the thick and thin CCT diminishes as we approach high failure percentages, which indicates that the protective role of a

thick CCT occurs at low shear failure values, i.e., when ONH is starting to get damaged (initial stage), and this role is reversed at the very last stages where the thinner cornea seems preferable.

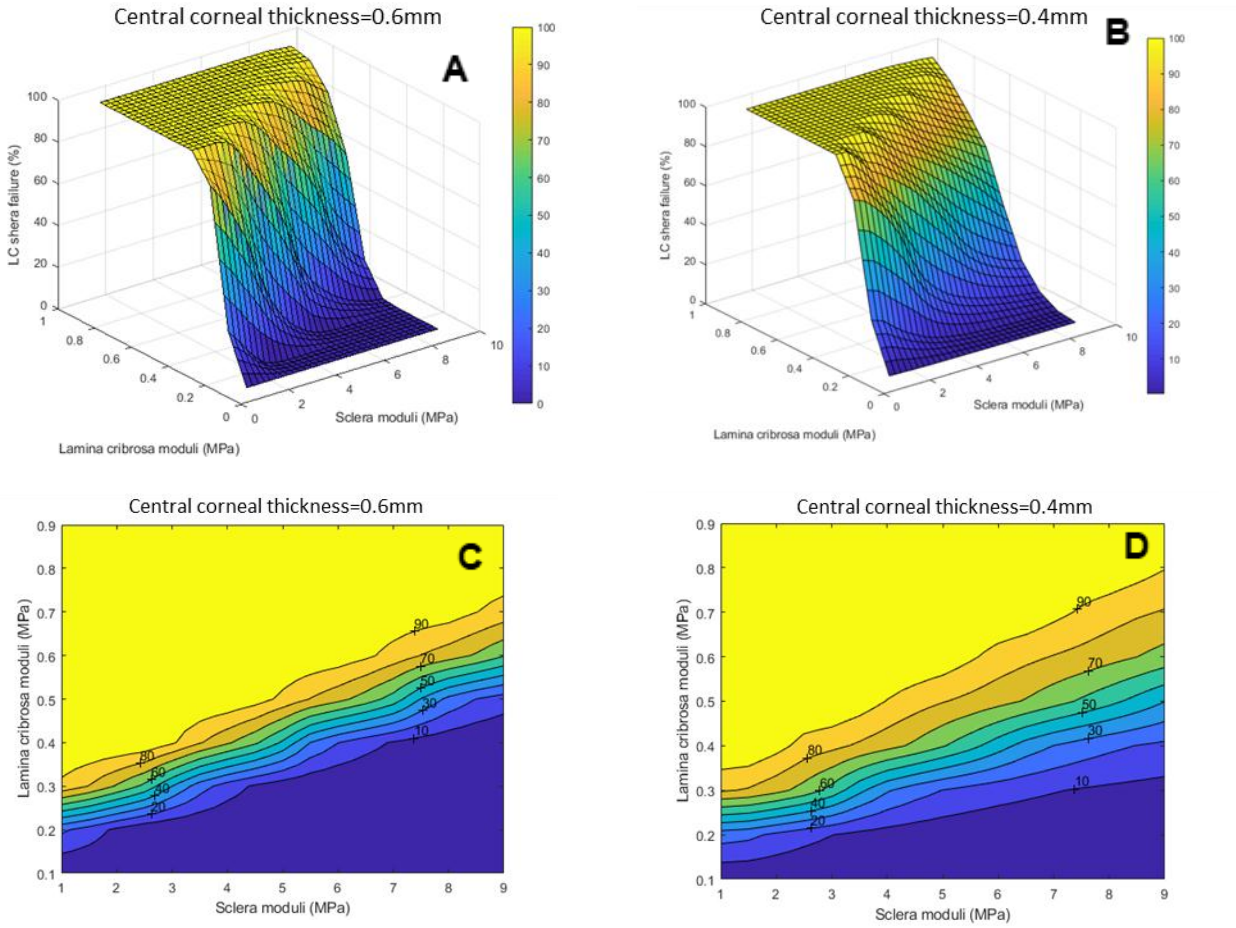

Figure 16. Three-dimensional plots (a, b) and isolines (c,d) of LC shear failure at different levels of LC and sclera moduli. Left column results correspond to a CCT value of 0.6 mm, while the right column corresponds to the thinner cornea value of 0.4 mm.

Glaucomatous vision loss starts from periphery and progresses towards the center [72, 94] with damaged nerves shown to be sheared [59, 95]. Results from our model show that shear stresses are higher in the periphery at IOP=25mmHg; see Fig. 17. The same figure depicts a shrinkage in the affected area when ICP reaches

15mmHg. This can be attributed to the reduction of the higher translaminar pressure difference (IOP-ICP). Several studies have provided clinical evidence in support of the theory that reduced ICP may play role in the pathogenesis of normal tensional glaucoma [96, 97].

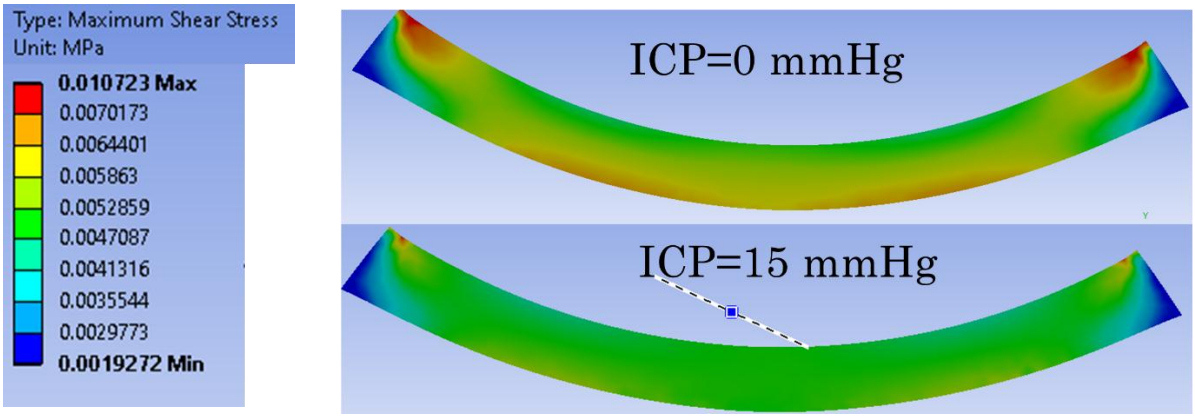

Figure 17. Computed Maximum Shear Strain patterns observed on lamina cribrosa cross section for the case of IOP=25mmHg with ICP values of 0 and 15 mmHg.

Besides, it is well documented by Johnson et al. [98] that thicker corneas lead to IOP overestimation when measured with applanation tonometry, and OHT patients would be diagnosed with normal pressure if the corneal thickness was taken into account. We need to note, that based on our findings, a thicker CCT will have a protective role for a generally stiff sclera and soft LC. Thicker corneas seem to prolong glaucoma's initial stage, especially in OHT patients with increased IOP.

3.4.3 Limitations of the study

This work includes several limitations. The model was calculated with linear and isotropic mechanical properties and axisymmetric geometric properties, which is rather an oversimplification. Another limitation of this study is that we assumed a uniform variation range of ±20% for all geometric and material parameters' values. This simplifying assumption may result in a slightly distorted image regarding the significance of some factors which may not differ that much from the considered base values. Third, all outcomes are considered only in terms of shear stress, whereas first and third principal strains and stresses should also be considered. Fourth, axonal damage is a slow and biologically mediated process, therefore using the Tresca failure criterion may not consider biological and age-related axonal disruption.

3.5 Conclusion

In this work, we have employed an eyeball model to investigate several factors contributing to optic nerve head damage under different levels of intraocular and intracranial pressure in ocular hypertension conditions. Finite element analysis calculations were used in this work to identify important factors influencing ONH biomechanics. Acute elevations in intraocular and intracranial pressures were utilized to quantify optic nerve head damage in lamina cribrosa. Our results indicate that intracranial pressure induces higher shear stress on post-laminar neural tissue than in lamina cribrosa. We have also studied the material and geometric properties of the cornea. Our findings indicate that a thicker cornea may

increase the risk of optic nerve head damage at an early stage of glaucoma. However, the cornea is much less influential than tissues closer to the optic nerve, such as peripapillary sclera.

Chapter 4. Automated Segmentation and Analysis of Optical Coherence Tomography Images

In this chapter, an algorithm to segment the retinal pigment epithelium (RPE) and internal limiting membrane (ILM) layer from the Spectral Domain Optical coherence tomography (SDOCT) image is developed. The proposed hybrid algorithm has two stages: the initial stage is based on intensity thresholding and the second stage utilizes a graph-based algorithm to fulfill the initial stage. Comparison results showed a good agreement between the segmented layer profiles using the proposed hybrid algorithm and manual segmentation relative difference: 1.49% ± 0.01%. The processing time of the proposed hybrid algorithm and the sole intensity algorithm used at initial stage did not show substantial change; however, the latter one could not segment all the points on that layer and did require additional processing, such as graph method which was the ambition to develop the proposed algorithm. The processing time of the sole graph algorithm (34.3s) is about four times higher than the processing time of the proposed algorithm (9.3s). The Dice's coefficients of the sole graph-based algorithm and the proposed algorithm are 74.1±14.8% and 96.7%±1.6% respectively. After automatic segmentation, the layers were automatically reconstructed.

4.1 Introduction

Optic nerve head image segmentation and analysis are important for the understanding of cell degeneration in glaucoma and the development of new diagnostic approaches [99]. Segmentation of optical coherence tomography (OCT) images is a challenging task. OCT is an imaging modality that generates cross-sectional images of the optic nerve head and retina. Application of image analysis into clinical use requires several actions: 1) validate the automated algorithm if the gold standard has not been renowned, 2) to select suitable values for image parameters and algorithms to design the specific OCT clinical data, 3) to run the algorithm with suitable parameters to set specific properties of the input data [100].

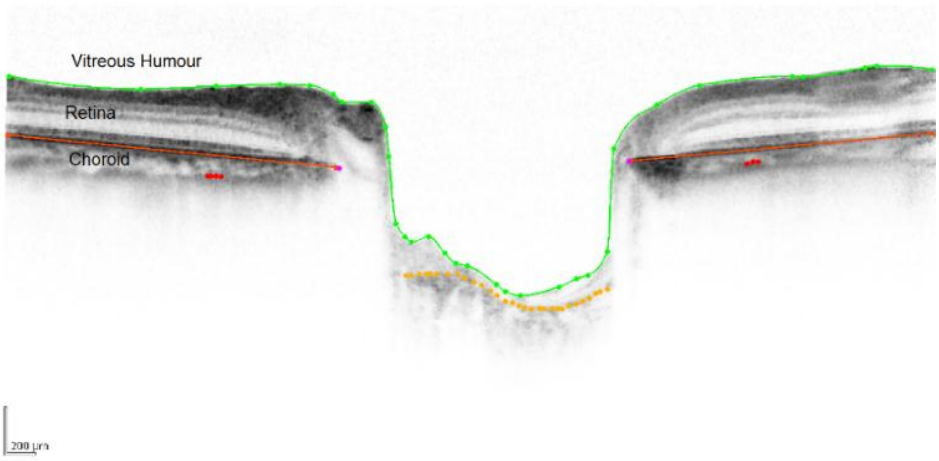

Figure 18. SDOCT image with retinal pigment epithelium layers (RPE–solid red line), internal limiting membrane (ILM–solid green line), and choroid representation.

Internal limiting membrane (ILM) (solid green line in Fig. 18) forms a membrane between the retina and the vitreous. Distance between the ILM and retinal pigment epithelium (red line in Fig.18) is a measure of retinal thickness [101]. Several segmentation methods have been proposed for OCT images of the macula region. 1D

based approaches find gradient peaks (intensity thresholding algorithms of the layer boundaries) [102]. 2D based methods for layer boundary segmentation such as edge detection [103], and 3D based methods [104].

OCT segmentation is a crucial part of image analysis. Loss of retinal ganglion cell axons in the region of the retina is a characteristic feature of ONH in glaucoma. The retina can be segmented and three-dimensionally reconstructed for further biomechanical analysis with the finite element analysis method [105]. Girard et al. [106] manually segmented and automatically reconstructed nine glaucoma patients to establish associations between retinal sensitivity and ONH strain. Therefore, the development of an automatic ONH retinal layer segmentation algorithm for SDOCT images is beneficial, as manual labeling of the layers is time-consuming and is a subjective operation.

4.2 Retinal layers automatic segmentation algorithm.

Optic nerve head region was imaged with Spectralis Optical Coherence Tomography (OCT) (super-luminescent diode laser center wavelength: 870 nm; scan speed: 40 000 A-scans per second; Germany, Heidelberg, Heidelberg Engineering). Six sections radial 1024 A-scans at 30 degrees angle with cross-sections positioned at the center. The cross-sections center was positioned manually by an operator using the eye-tracking system to estimate the clinical disc margin. The image signal-to-noise ratio was increased using automatically averaging software of fifteen B-scans. Scan quality score of each image was at least equal to 20. The OCT data

sets were collected from 20 patients recruited for a study investigating lamina cribrosa and ONH deformation in glaucoma [99]. The OCT images were manually segmented by a clinician using custom software developed in MATLAB (R2016b, MathWorks, Inc.) to serve as a reference standard for evaluation of the agreement of the proposed hybrid segmentation algorithm (Fig. 18).

First, the ILM and RPE layers were segmented by intensity thresholding algorithm. However, the intensity values varied within columns and therefore, continuous detection of points with thresholding technique was challenging, especially in diseased eyes. A graph-based algorithm [107] was then used to further process the image to ensure continuous segmentation labeling lines. The processing of a single image by using only graph-based algorithm took a substantial amount of time to segment the entire layer (421 seconds, computed with a computer with CPU i5 core 6.60GHz, 4GB RAM) due to the high resolution of the image and high computational power demand of the algorithm. The processing time of a hundred images would take up to several hours, hence it does not apply to daily routine clinical imaging and diagnosis. Therefore, the proposed hybrid algorithm aims to combine the intensity thresholding method with the graph-based algorithm to decrease computational processing time while maintaining a good segmentation accuracy. Sections A to E describes the proposed hybrid segmentation algorithm. The schematic overview of the proposed hybrid algorithm is shown in Fig. 19.

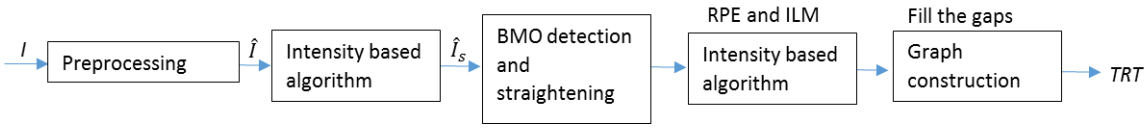

Figure 19. The overview of the automatic segmentation of the ILM and RPE layers in SDOCT images.

A. Preprocessing: To suppress the thermal and electronic noise, the original SDOCT image indicated as $I(x,y)$ or $(x,y) \in [1,N_c] \times [1,N_r]$, where N_c is the number of columns and N_r is the number of rows, was first convolved with a 2-D Gaussian smoothing kernel with a standard deviation of 2, which is a common filtering method where authors [108, 109] used for B-scan modes. The image was then convolved with a 10×10 median filter by linear low pass filtering averaging across edges. The image after the combination of these two filtering methods denoted as $\hat{I}(x,y)$,, gave adequate segmentation results with suppressed local image speckle.

B. Intensity-based algorithm: The principle of finding the RPE layer was based on the intensity of the backscattered light that appears lowest compared with other layers. It is easily visible and easy to detect, so the pixels with lowest intensities in the A-scans were assigned as the boundary of RPE, denoted as LRPE and defined by the local minima point,

$$L_{RPE} = \left\{(x, y_{RPE}) | x \in [1, N_c], y_{RPE} = min\left(\hat{I}(x,u)\right)\right\} \quad (1)$$

where $u \in [1,N_r]$ and it is related to the intensities of the de-noised image $\hat{I}$ in the corresponding column. To distinguish the points caused by noise and blood vessels, a 4th order polynomial, $f_{BM}(x) = \widetilde{p_4}x^4 + \widetilde{p_3}x^3 + \widetilde{p_2}x^2 + \widetilde{p_1}x + \widetilde{p_0}$ was used to create a smooth and continuous curve to eliminate randomly appeared RPE points (leave it empty) as a result of abrupt transitions of the delineated boundary. The principle of

finding ILM is based on automatically performs clustering-based image thresholding [110].

C. Search region limitation: The outlier structures with analogous characteristics often prevent the algorithm segmenting accidentally outer plexiform layer (OPL) and inner plexiform layer (IPL) instead of RPE. It is beneficial to limit the search region that helps to exclude any external layers to a valid target layer. The intensity-based algorithm, described in section B, has limitations when finding the RPE boundary, where empty spaces need to be fulfilled (Fig. 20). These empty spaces were used to limit the search region in the form of a box with 5 pixels up and 5 pixels down from the start (where the gap begins) and end (where the gap ends) points of the RPE empty areas. Considering the mentioned drawbacks, the pixels, which could not be delineated by the intensity-based algorithm or wrongly delineated, were demarcated afterward by the graph-based algorithm.

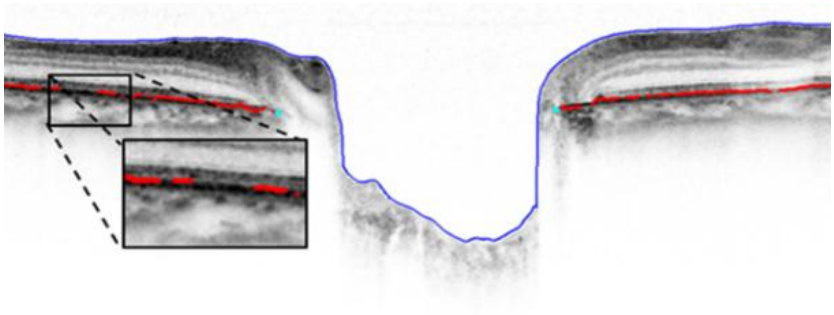

Figure 20. An example of the ILM layer (blue line) and RPE layer (red line) segmentation with the solely intensity-based algorithm

Start and endpoints were selected and estimated from the specific layer. This endpoint selection was performed at two ends of the image. So, if the empty part of

the segmentation line is at the beginning of the end, then an extra column of nodes is added to both sides of the image. Minimal weights were assigned arbitrarily to the intensity values in the vertical direction. Once it was segmented, the additional columns were removed. As the RPE layer represents the darkest line it had a lower weight as a function of pixel intensity.

D. Graph weights calculation: A minimum weighted path was found using Dijkstra's algorithm [111] to find the associated with edges connecting two endpoints of graphs. Set of pixels in each image characterized as an undirected graph of nodes $G = (V, E)$, where every pair of the nodes formed an edge in the image space. The key to accurately cut graphs is to set up weights on the edges connecting nodes according to their similarity. Borders of the objects to be segmented are given lower weights to separate it from other features of that object.

Graph weights in the literature [112] represented as intensity variation and geometric distance. Weights were assigned to individual edges to reflect the possibility that two pixels belonged to the same line. The SDOCT images used in this study had a relatively high resolution. As a result of plane change between adjacent pixels, each node is related to its eight neighbor pixels and is disassociating with geometric distance weights. The type of graph was defined to be undirected to half of the adjacency matrix size.

$$w_{ab} = 2 - (g_a + g_b) + w_{min} \qquad (1)$$

where g_a is the vertical image gradient of point a, g_b is the vertical image gradient of point b, w_{min} is the minimum weight in the graph, which is equal to 10^{-5} extra number for system stabilization, w_{ab} is the weight of lines connecting vertices a and b. After construction of adjacent matrix and graph G with appropriately weighted nodes with minimum total length, the empty parts as shown in Fig. 20 were cut using Dijkstra's algorithm [111]. Equation (2) shows weights calculation based on intensity gradients. It assigns high values to node pairs with low vertical gradients, where g_a and g_b are stabilized in the range of values between 0 and 1. Segmented image with the hybrid algorithm is shown in Fig. 21 which combines intensity-based and graph-based algorithms.

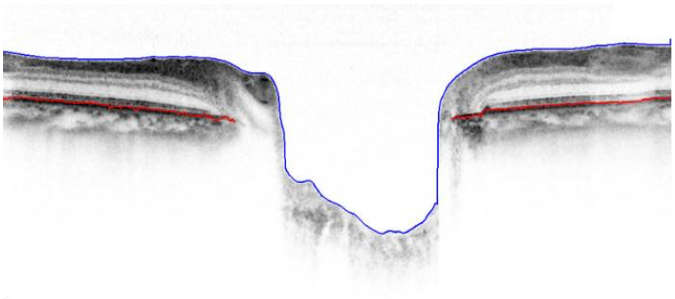

Figure 21. Segmentation RPE (red line) and the result of ILM (blue line) of the hybrid algorithm, which is a combination of solely intensity and graph-based algorithms, after filling RPE gaps with the graph-based approach.

E. Dice's coefficient and segmentation errors: Three performance metrics, including Dice's coefficient, Automatic and Manual Relative Segmentation Difference (AMRSD) and Relative Segmentation Proportion Percentage (RSPP) were used to evaluate the accuracy of the algorithms compared to the manually segmented layer profile.

The distance between the upper (ILM) and lower (RPE) boundaries is represented as Total Retinal Distance (TRT) and used as a reference standard to evaluate the accuracy of

the automatic algorithm [113]. The manually labeled TRT region between ILM^0 to RPE^0 represents the reference standard, denoted as TRT^0.

Dice's coefficient ($Dice_{TRT}$) is used as a performance metric to evaluate the variability of the whole profile of the algorithms with the manually ground truth expert segmented image results and it was defined as,

$$Dice_{TRT} = \frac{2|TRT \cap TRT^0|}{|TRT| + |TRT^0|} \quad (3)$$

The high value of $Dice_{TRT}$ indicates a lower difference with the results from manual segmentation, thus better performance of the automatic algorithm [114].

Automatic and Manual Relative Segmentation Difference (AMRSD) was defined as the relative segmentation error of the whole profile between RPE^0 (manually segmented layer) and RPE (automatically segmented layer). A higher value of AMRSD represents a higher relative error.

$$AMRSD_{RPE} = |RPE^0 - RPE| \times 100\% \quad (4)$$

Relative Segmentation Proportion Percentage (RSPP) calculates a number of the ILM^0 and RPE^0 points relative to automatically segmented RPE and ILM that can be segmented by the hybrid algorithm, intensity thresholding algorithm, and graph-based algorithm, defined as the ratio of a total number of retinal pigment epithelium (TNRPE) and a total number of automatically segmented internal limiting membrane (TNILM) pixels and manually segmented values ($TNILM^0$ and $TNRPE^0$). The higher value of RSPP represents more data points (pixels) to be segmented by an automatic algorithm.

$$RSPP_{RPE} = \frac{TNRPE}{TNRPE^0} \times 100\% \qquad (5)$$

$$RSPP_{ILM} = \frac{TNILM}{TNILM^0} \times 100\% \qquad (6)$$

One hundred and twenty SDOCT B-scans of twenty glaucoma patients were included for analysis. For each SDOCT B-scan, the RPE and ILM layer boundary pixels were first labeled manually by a clinician.

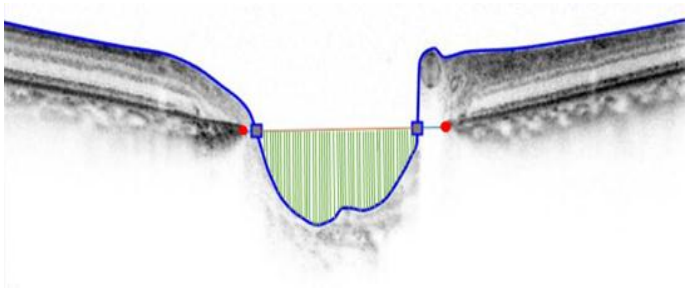

Figure 22. A depiction of the ONHSD which represents an average of perpendicular distances from a red line joining two BMO points to the ILM layer.

The performance of automated segmentation obtained with the three algorithms (intensity thresholding algorithm, graph-based algorithm and proposed hybrid algorithm) was compared with the 120 manually segmented layer profiles. Fig. 18 shows the manually segmented layer profile outlined by a clinician and Fig. 21 shows the automated segmentation results of the hybrid algorithm from a selected patient.

Table 6. Summary of the processing time of one image, the mean and standard deviation of ILM and RPE comparison of relative difference with manual segmented image and Dice coefficients of hundred and twenty image

Algorithm	Processing time (s)	AMRSD (μm)	Dice Coefficient (%)
Intensity thresholding algorithm	3.7	5.42±0.03	96.8±1.7
Graph-based algorithm	34.3	24.7 ± 0.23	74.1 ± 14.8
Proposed Hybrid algorithm	9.3	5.73 ± 0.03	96.6 ± 1.6

The average processing time, AMRSD and Dice's coefficient are summarized in Table 6. As shown in Table 6, the intensity thresholding algorithm was 9.27 times faster than the graph-based algorithm and the hybrid algorithm. AMRSD for the intensity thresholding algorithm and the proposed hybrid algorithm fell in a similar range and had a comparable value, whereas the graph-based algorithm showed the highest AMRSD.

The Dice's coefficient of the graph-based algorithm was considerably lower, compared with the Dice's coefficient of the other two algorithms (>96%) and has a value of 74.1 ± 14.8%. There were no detectable differences in Dice's coefficients between hybrid and intensity thresholding algorithms.

Table 7 shows a summary of RSPP, which varies across RPE and ILM layers.

RSPP results for RPE and ILM with intensity thresholding algorithm were 52.2 ± 18.5% and 84.6 ± 12.8% respectively. The intensity algorithm could segment about only half of the RPE points and more segmented pixels for ILM. Slightly larger RSPP was noted for the graph-based algorithm compared with the intensity thresholding algorithm, segmented about the same amount of points for RPE and ILM. The largest RSPP of the RPE and ILM were noted in the proposed hybrid algorithm.

Table 7. Summary of RSPP comparison for RPE and ILM layers of hundred and twenty images

Algorithm	RPE†	ILM†
Intensity thresholding algorithm	52.2 ± 18.5	84.6 ± 12.8
Graph-based algorithm	76.9 ± 15.9	76.9 ± 12.4
Proposed Hybrid algorithm	88.3 ± 9.5	88.5 ± 9.8

† percentage (mean ± standard deviation)

Optic nerve head surface depth (ONHSD) (green lines) represents average perpendicular distances from a line joining Bruch's Membrane Opening (BMO) points (red points and brown line) to the ILM surface (blue line) (Fig. 22). ONHSD was calculated as an average for the analysis. ONHSD agreement between the manually detected surface (i.e. ILM layer) and proposed hybrid algorithm is shown in the Bland-Altman plot in Fig. 23.

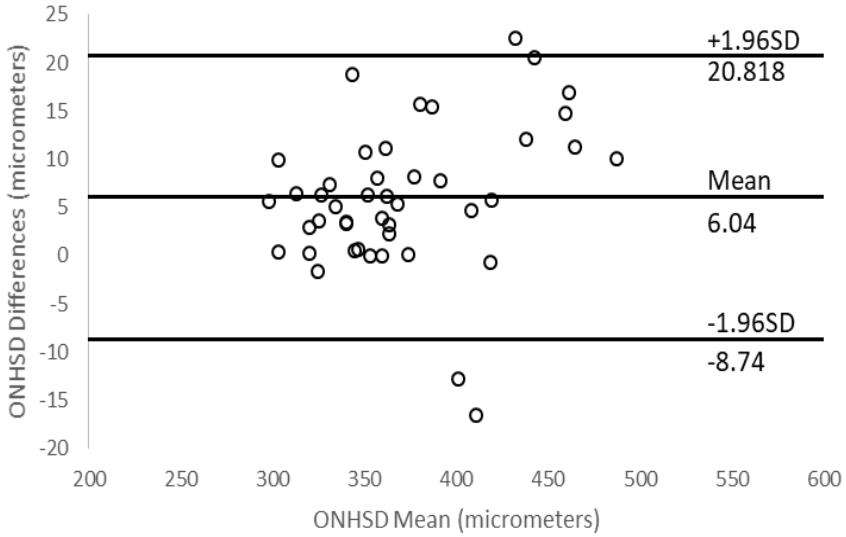

Figure 23. Bland-Altman plot of the ONHSD measurement between the proposed hybrid algorithm and manual segmentation.

The average difference of ONHSD was 1.58% ± 1.87%, which shows good agreement between the manually traced and automatically delineated surfaces.

A graph-based approach for the segmentation of SDOCT images is an efficient algorithm that warrants the total optimality of the results concerning the cost function. High resolution and a large number of SDOCT images require substantial computational power and processing time for the calculation. The processing time with a graph-based algorithm could be reduced in multiple ways. In this study, a hybrid algorithm was proposed, which integrated the ability to incorporate fast and simple intensity-thresholding algorithm and the robustness of the graph-based approach in the presence of noise as well as disease-induced disruptions. This study aims to increase segmentation accuracy and reduce the computational processing time for the segmentation of RPE and ILM layers in the SDOCT images.

The results show the hybrid algorithm is accurate and reproducible. The processing time of the graph-based algorithm (34.3s) was about four times slower than the average processing time of the proposed hybrid algorithm (9.3s) and the intensity thresholding algorithm required 3.7s, which was the fastest algorithm among these three algorithms. However, 52% of data points of the RSPP of the intensity thresholding could be segmented by intensity thresholding algorithm compared with the manual segmented ILM layer profile. The RSPP of the proposed hybrid algorithm showed the highest value in both ILM and RPE layers compared to the intensity thresholding algorithm and graph-based algorithm (both>88%).

AMRSD of the proposed hybrid algorithm (5.73 ± 0.03 μm) was lower than that of the graph-based algorithm (24.7 ± 0.23 μm) and showed a comparable value with that of the intensity algorithm. The proposed hybrid algorithm assumes the RPE layer is continuous. However, this layer can be distorted by disease and the artifacts. The algorithm can digress from the RPE layer, which results from gradient changes instead of smooth segmentation.

The Dice's coefficient of the proposed hybrid algorithm is 96.6% ± 1.6%, which shows substantially higher consistency with the manually segmented image in comparison with the graph-based algorithm (74.1 ± 14.8%). The proposed hybrid algorithm robustly segmented both the RPE and ILM layers in SDOCT images. This method has certain limitations when applying to the RPE segmentation task when finding BMO points. The Dice's coefficients varied through different images due to different image noise levels. The Dice's coefficient standard deviation was 1.6 among the images. The

variability of the graph algorithm was significantly lower showing a standard deviation of 14.8.

In summary, we have proposed and presented a fast and accurate hybrid algorithm integrated the fast and simple intensity thresholding algorithm and the robustness of the graph-based approach for the segmentation of RPE and ILM layers in SD-OCT images. Comparative studies of the hybrid algorithm segmented profiles with the segmentation results from the intensity thresholding algorithm, graph-based algorithm and manual segmentation in a hundred and twenty SD-OCT images showed good accuracy of 96.6%. The processing time of one image by the hybrid algorithm is 9.3 sec, which is only one-fourth of processing time required for graph algorithm, which is a great advance to bring real-time image analysis into a clinical routine application.

Chapter 5. Patient-specific modeling and analysis

In this chapter, the effect of intraocular (IOP) and intracranial pressure (ICP) on the optic nerve head (ONH) and their correlation to patient-specific geometric characteristics are analyzed. Optical coherence tomography images were obtained from six patient eyes. Corresponding three-dimensional models of the ONH region were reconstructed from the OCT images and embedded into a generic cornea-scleral shell to create a complete model of the eye. The finite element analysis method was employed to quantify the effects of acute changes in IOP and ICP on the ONH biomechanical environment. Maximum principal and maximum shear strains were computed and used for assessing ONH damage. Results reveal substantial shear strains in lamina cribrosa and also indicate that the inter-individual geometric variations affect ONH biomechanics. Finally, cerebrospinal fluid pressure applied to patient-specific ONH models revealed a wider range of deformations that are not captured by a generic eye model.

5.1 Introduction

As already mentioned in previous chapters, FEM modeling has been proven an effective tool for studying glaucoma-related ONH problems [16, 30, 34, 43, 83, 115]. The commonly followed approach involves the construction of a generic eye model with statistically-induced geometric and material properties and running FEM analysis to obtain stress-strain information. However, actual human-eye geometry can substantially differ from the generic models constructed based on average values and idealized geometries, which may render the results acquired from generic models questionable. This potential issue has been recognized by the pertinent community, but it has not been studied to the full extent yet. Certainly, one may address this issue by employing patient-specific models when conducting the relevant ONH biomechanical behavior studies. Sigal et al. [116] used ex vivo digital photographs of human eye samples for 3D reconstruction and studied strains in ONH induced by IOP change. However, the influence of the translaminar pressure gradient was not considered in that study. Another work on individual-specific models was recently presented by Schwaner et al. [117], where a methodology for individual-specific modeling of rat ONH biomechanics was proposed. However, it is commonly accepted that rat ONH differs considerably from human ONH [118, 119], and; therefore, these results may be inapplicable to human glaucoma studies.

From the discussion above, we can easily deduce the potential scientific merit in studying the IOP-ICP induced ONH deformations using patient-specific human

ONH models. In this part, we present a methodology for the 3D reconstruction of patient-specific ONH models from Spectral-Domain Optical Coherence Tomography (SD-OCT) B-scan images. OCT is a noninvasive imaging technique based on the interference of reflected laser light. SD-OCT, an enhanced OCT technology, has allowed the reconstruction and quantification of peripapillary retinal nerve fiber layer thickness [120–122]. In our study, we applied the compensation algorithm [123] to SD-OCT images for improving the LC visibility. This allowed us to enhance the accuracy of the acquired geometry in patient-specific models. Finally, the reconstructed patient-specific models were used in studying the effect of geometry on the generated strains under a combined application of IOP and ICP.

5.2 Segmentation and three-dimensional reconstruction of ONH

In this section, we briefly describe the employed image delineation technique along with the steps followed for the 3D reconstruction of the patient-specific components which are later incorporated into a complete human-eye model.

5.2.1 Image delineation

Optical coherence tomography scans of six anonymized patients with enhanced depth imaging (EDI) taken in the Kazakh Institute of Eye Diseases for ONHs were used in our work. Each set of images comprised of six radial B scans centered on the ONH and rotated using 30 degrees angle-step. An example image of

the OCT scans acquired by the employed Spectralis OCT device is shown in Fig. 24 below. Images were chosen so that at least 80% of the posterior lamina cribrosa surface could be depicted.

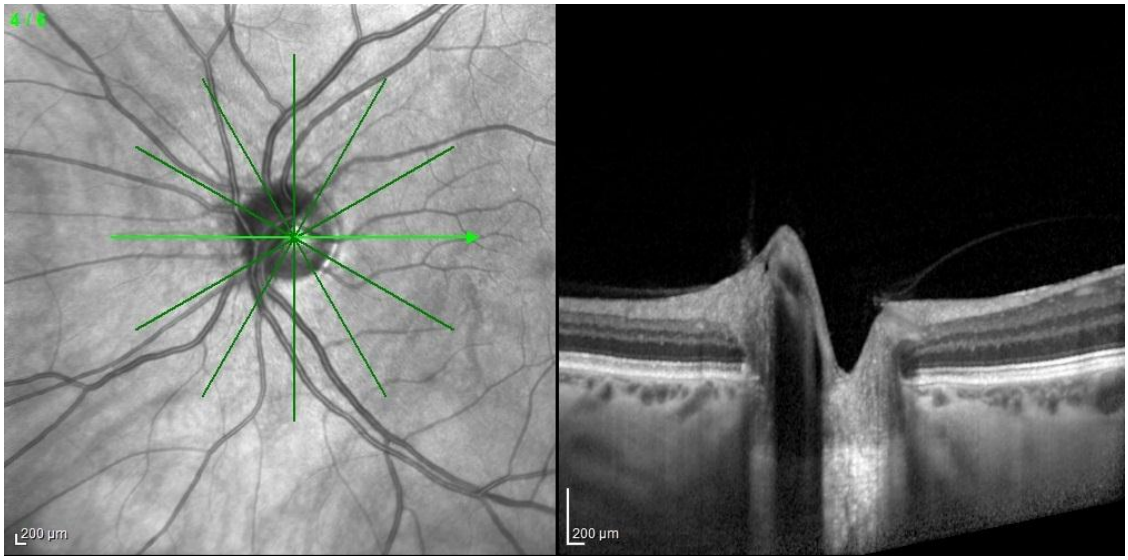

Figure 24. Original OCT image with EDI obtained with Spectralis OCT device.

Prelaminar tissue surface and Bruch's membrane were segmented with the hybrid algorithm described in chapter 4 and anterior/posterior lamina surfaces were segmented manually with the aid of a customized MATLAB script (R2019a, MathWorks, Inc, Natick, MA) processing radial sections of the optic disk. Raw OCT images were first enhanced using the compensation algorithm proposed in [123]. Specifically, the following equation was employed:

$$I_{i,j}^{comp} = \frac{1}{2\sum_{k=i}^{n} I_{k,j}^{n} \times I_{i,j}^{n}}, \qquad (7)$$

where i is the pixel number of A-scan which is ranging from 1 to N and $2\sum_{k=i}^{n} I_{k,j}^{n} \times I_{i,j}^{n}$ is the compensation factor and j is a column. After the algorithm's application,

lamina cribrosa anterior and posterior surfaces were manually delineated. Example OCT image with segmented layers post-compensation algorithm applied is shown below in Fig. 25.

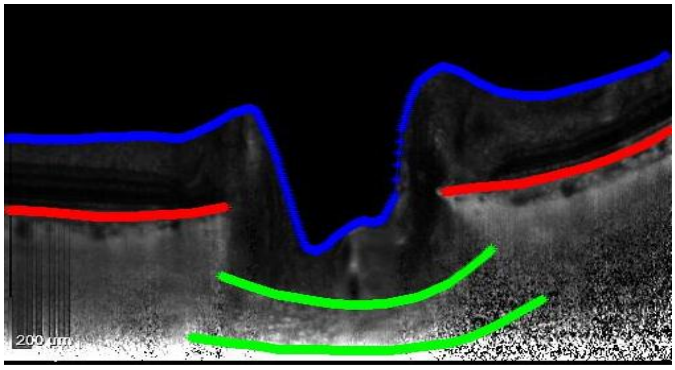

Figure 25. Typical OCT B scan from Spectralis OCT showing retinal pigment epithelium (RPE) (red), internal limiting membrane (ILM) (blue) layers and lamina cribrosa anterior/posterior surfaces (green).

Anterior and posterior lamina cribrosa surfaces were defined by a sharp increase in signal intensity below optic disc up to peripapillary sclera [124]. EDI in concert with compensation algorithm improved lamina cribrosa visibility [125]. Anterior lamina cribrosa surface after application of the compensation algorithm + EDI made possible to be visible in all 26 patient images. Regions where lamina cribrosa was not visible, were left unmarked.

5.2.2 Three-dimensional reconstruction

After delineation of ILM, RPE and lamina cribrosa, the points representing optic nerve head structures were rotated counterclockwise with rotation matrix (equation 8) and placed in a three-dimensional Euclidean space (Fig. 26) through an angle $\theta=30^0$:

$$Z = \begin{bmatrix} cos\theta & -sin\theta \\ sin\theta & \cos\theta \end{bmatrix} \times \begin{vmatrix} x \\ y \end{vmatrix} \quad (8)$$

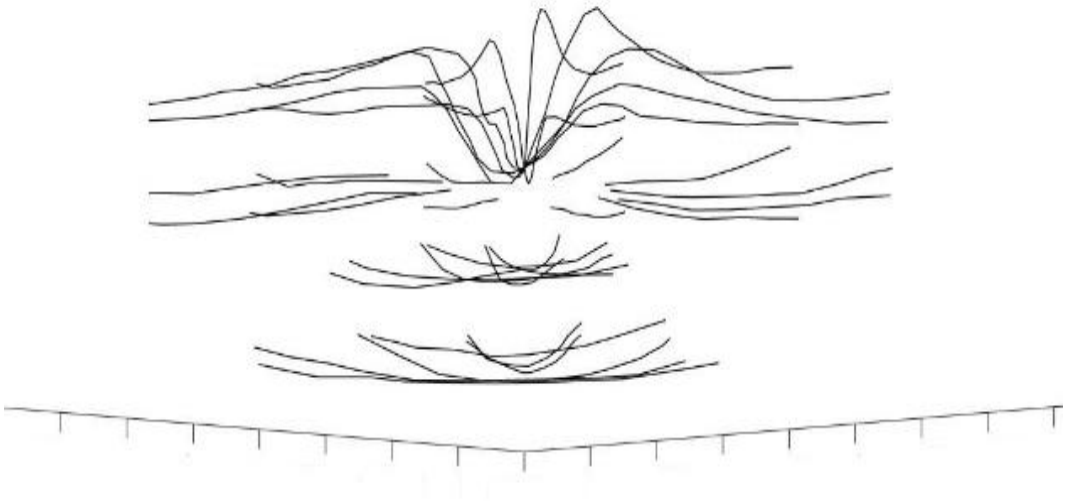

Figure 26. Full set of 6 radial curve delineations for a human optic nerve head (ONH)

After rotation, ONH points were three-dimensionally reconstructed (Fig. 27). A thin plate spline method was used to generate a best-fitting surface corresponding to the segmented ONH points. A proper scaling adjustment (micrometer/pixel) for each B-scan was applied to secure an accurate 3D reconstruction of ONH geometry. Lamina cribrosa edge points were fitted using least-squares fit on ellipse using the "fit ellipse" function [126]. Example data points and the fitted ellipse is shown in figure 27.

The center of each ONH surface curves was aligned with the optic disc center, which was used for image registration

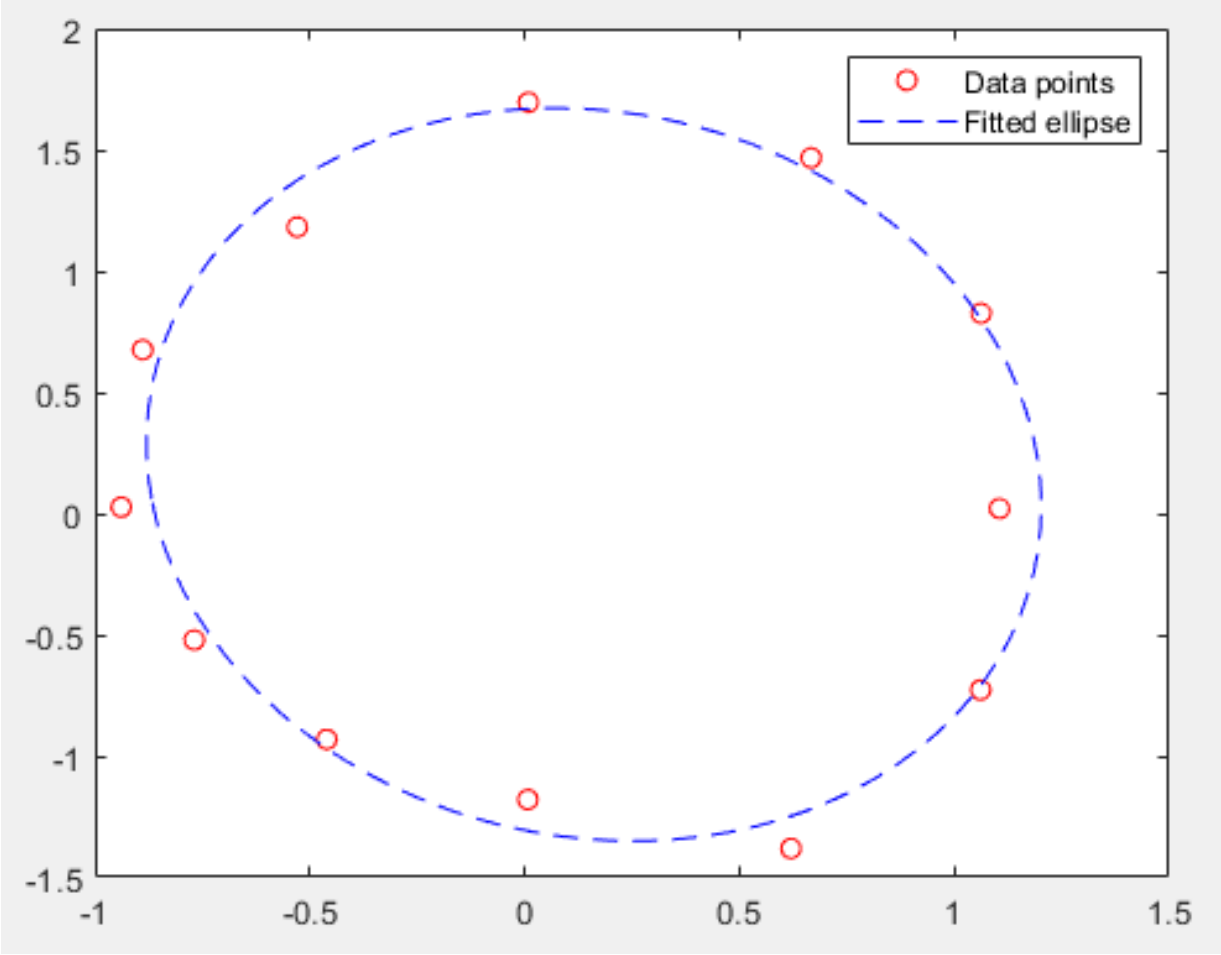

Figure 27. Example data points and fitted ellipse.

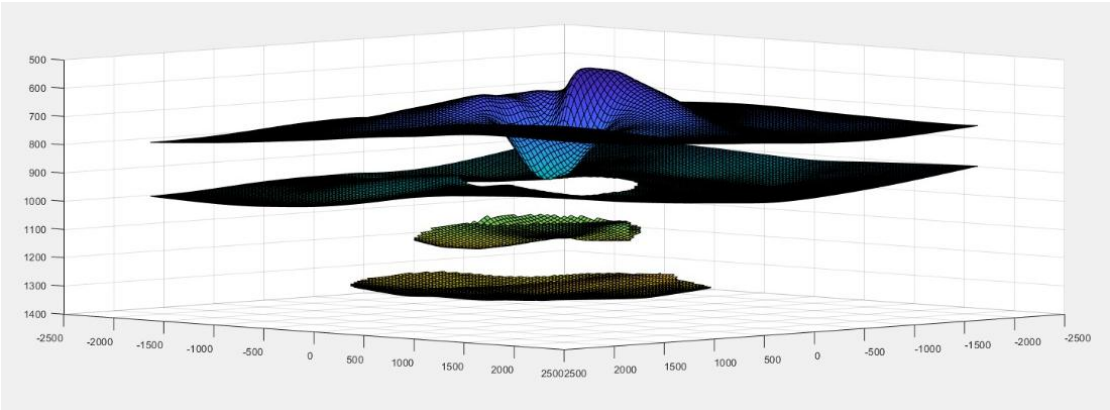

Figure 28. Visualization of reconstructed surfaces of ONH layers.

5.3 Building patient-specific and generic models

The resulting 3D point clouds (Fig. 29), describing ONH geometry, were used for surface fitting within Solidworks[2] CAD software package; see Figs. 30. BMO and anterior LC surface edges were then connected with a surface loft operation. The complete set of surfaces was then used to generate the solids representing the corresponding tissues (Fig. 30). This procedure can lead to some small overlaps among tissues, which are treated by removing the overlapping parts with Boolean differences between the offending solids. Specifically, pia mater, sclera and PLNT boundaries are adjusted to the patient-specific ONH to ensure valid topologies and that adjacent tissues share common boundary surfaces.

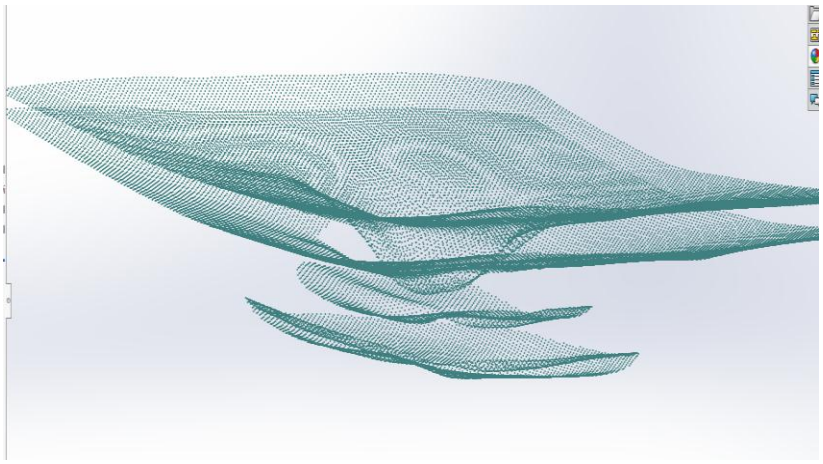

Figure 29. Point clouds produced from fitted delineations of radial sections.

[2] SolidWorks 3D CAD from Dassault Systems, https://www.solidworks.com/

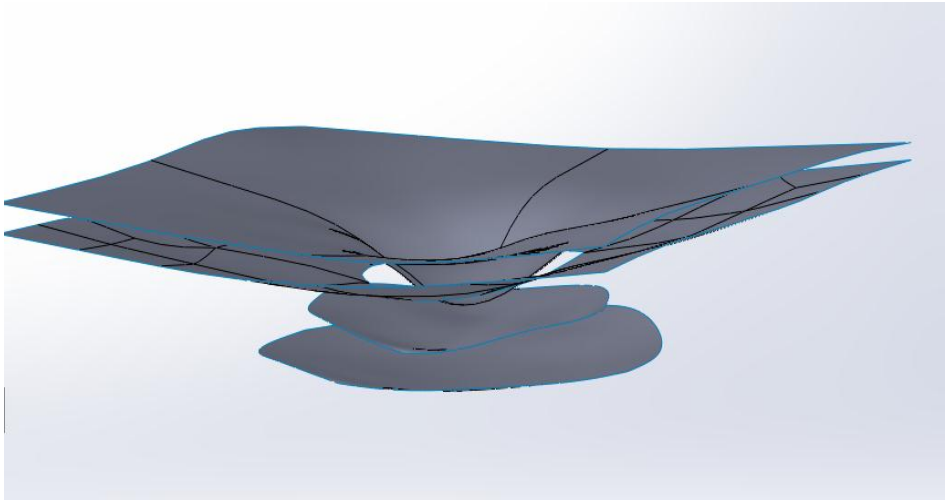

Figure 30. ONH surfaces constructed from 3D point clouds.

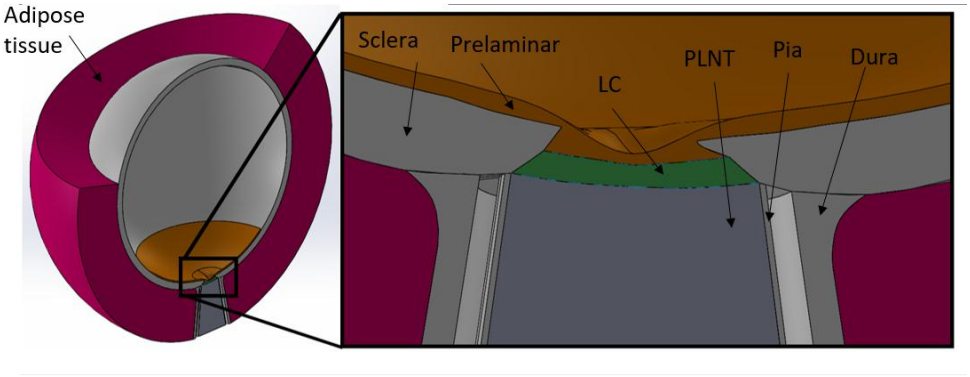

Figure 31. 3D patient-specific model of the eye embedded into the generic corneoscleral shell.

Dura and pia mater follow the representation from generic models found in the literature [19] and are also included in our eye model allowing for a more accurate cerebrospinal fluid pressure modeling. Finally, the reconstructed patient-specific ONH models were embedded into a generic cornea-scleral shell, identical to the one described in [62].

Apart from the patient-specific model, a generic eye model (Fig. 32) was employed in our studies based on shapes and dimensions obtained from pertinent

literature [19, 43]; see Table 1. Specifically, sclera was considered as a 0.8 mm thick shell with an external radius of 12.8 mm outside of the ONH region. LC was modeled as a 0.3 mm thick disk with diameters of 1.8 and 2.14 mm for the posterior and anterior faces, respectively. Finally, the thickness of the axisymmetric adipose tissue was set to 4.6 mm. The inclusion of the generic model allows us to assess the effect of patient-specific geometry in lamina cribrosa.

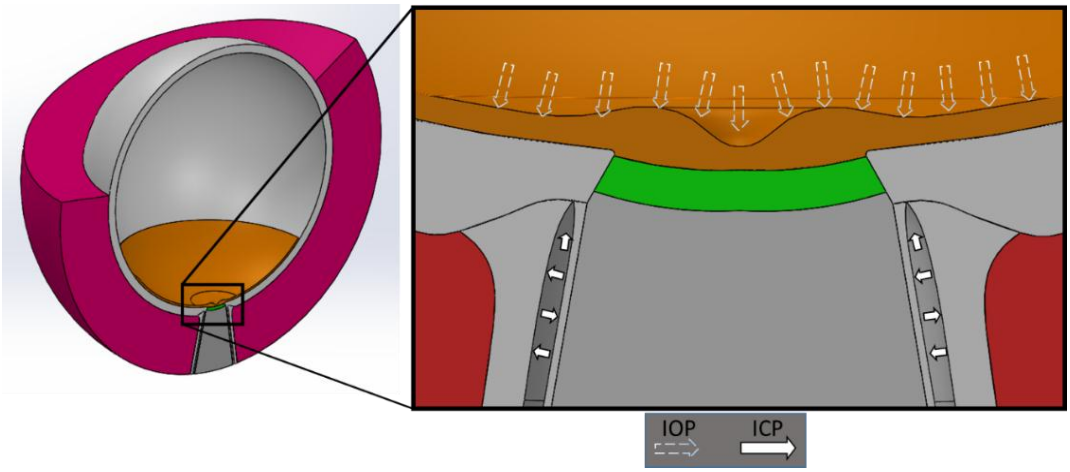

Figure 32. Generic eyeball model with intraocular pressure (IOP) and intracranial pressure (ICP) denoted with dashed and solid arrows, respectively.

5.4 Meshing and loads

All tissue solids were then exported to FEA software (ANSYS Simulation, 19.1) for producing appropriate meshes and performing the required computations. Simulations were run on a high-performance workstation with 50×Intel Core I7@2.6GHz CPUs and 500 GB of RAM. Results were post-processed within ANSYS and additional MATLAB scripts.

Meshing was performed with mostly tetrahedral elements and special attention was paid to the ONH region, which was refined successively till the convergence criteria were met. Bonded contacts without friction were applied among all inner surfaces. The outer part of the adipose tissue was modeled as a fixed boundary condition.

5.5. Material properties.

In terms of material properties, this study consists of two parts: 1) study the effect of static IOP and ICP with linear elastic material properties; 2) study the effect of static IOP and ICP with viscoelastic material properties of sclera and dura mater and compare with the first part. This will allow seeing the difference of the results taken with linear elastic and viscoelastic material properties. A model with viscoelastic material properties will also be helpful to perform dynamic simulations in the future to see the effect of pulsatile heart or pulsatile ICP.

5.4.1 Linear Elastic material properties

All tissues were considered isotropic, linear elastic (Table 1) and incompressible solids with a Poisson's ratio of 0.49 [30, 127]. IOP values of 20 and 25 mmHg were applied to the inner part of the sclera surface to represent acute glaucomatous pressure, and ICP values of 5, 10 and 15 mmHg were applied in the subarachnoid space (Fig. 31) representing ICP fluctuation in an eye of a typical adult individual

[128]. The effects of a constant 10 mmHg translaminar pressure difference (TLPD = IOP-ICP) were studied for the following pairs of IOP and ICP pressure values: (25, 15) and (20, 10) mmHg.

5.4.2 Viscoelastic material properties: Stress relaxation tests on sclera and dura mater

Viscoelastic behavior of the sclera and dura mater of the sheep eye was studied employing stress relaxation experiments. The tests were conducted in uniaxial loading apparatus MTS Criterion™ Model 43 (Figure 33a). This apparatus allows us to apply up to 30 kN rated force at a maximum of 1020 mm/min test speed and obtain results at 1000 Hz rate. Inflow and outflow tubes are connected to the testing chamber (Figure 33b) so that 37 degrees of saline water is constantly circulated during the test.

Eyes of eight ewes taken from a local abattoir, just after they were slaughtered and then transported to the laboratory in a sealed container with ice. A strip of sclera from all eyes was dissected along a meridional stretch 5mm apart from ONH, which led to its rectangular shape. For the Dura mater, which is the tough outer layer with a length at least ten times longer than its radius, a strip of ewe dura sheath was taken along the longitudinal direction and was subjected to a mechanical uniaxial test. The required sections of the dura mater and sclera were cut and fixed between two clips of the apparatus. Preconditioning with 100 cycles of 5% strain was conducted before each test. The tissues were stretched to the defined

strain value at 0.1/s rate and allowed to settle for 100 s. Both dura mater and sclera were stretched to 10 %. Average stress relaxation results are shown in Figure 34.

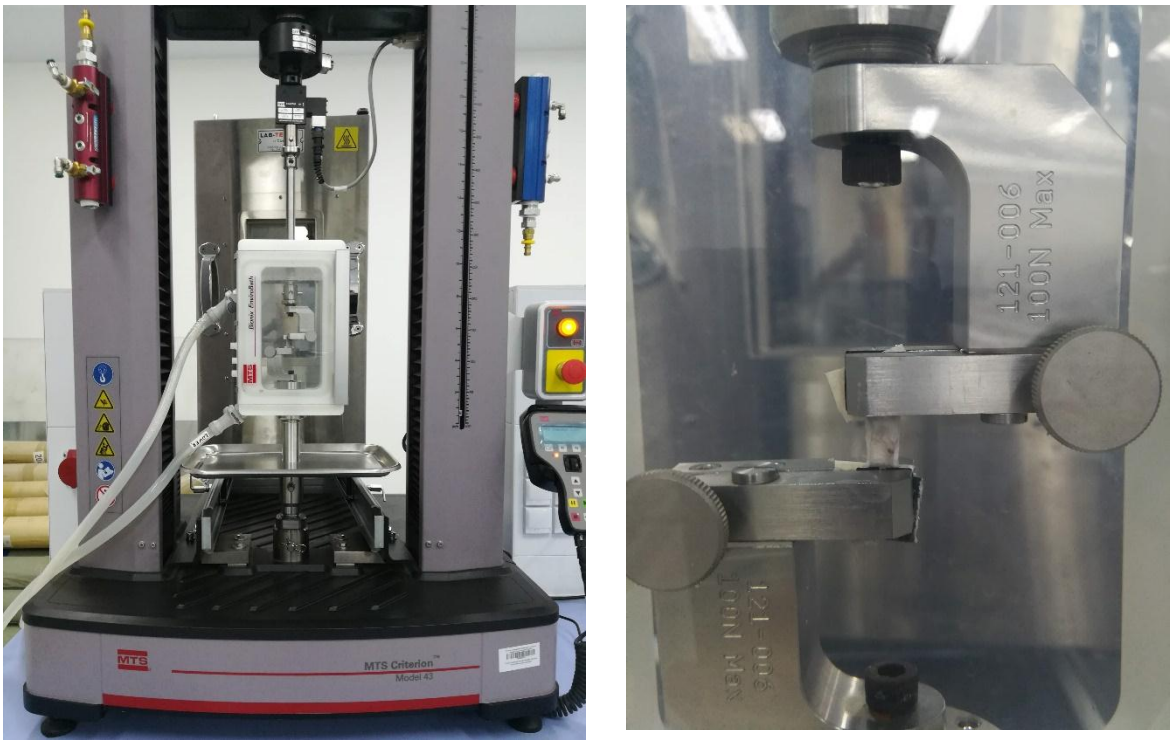

a) b)

Figure 33. Uniaxial loading apparatus

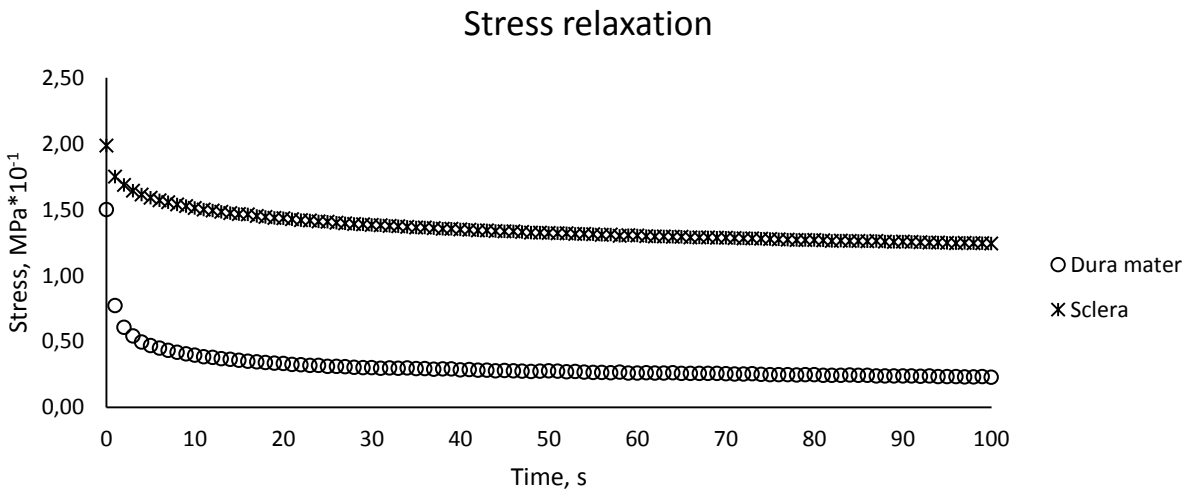

Figure 34. Stress relaxation experimental results of dura mater and sclera

5.4.2. Viscoelastic properties as input for Finite Element Modelling

Viscoelastic properties of sclera and dura mater from the stress-relaxation test were used as input parameters for Finite Element Modelling for the second part of this study. The technique was adapted from Machiraju et al., (2006). The terminal load value, terminal strain value, relaxation time and load values corresponding to the passing time are recorded.

Relaxation modulus E of the specimen at each time step can be calculated as follows

$$E(t) = \frac{F(t)}{A\varepsilon_{max}} \qquad (9)$$

where ε_{max} – terminal strain value, $F(t)$ – load at time t.

Wiechert's constitutive model consists of springs and dashpots connected in series, and the couples connected in parallel (Fig.35). The elastic part is described by the spring and the viscous part is described by the dashpot.

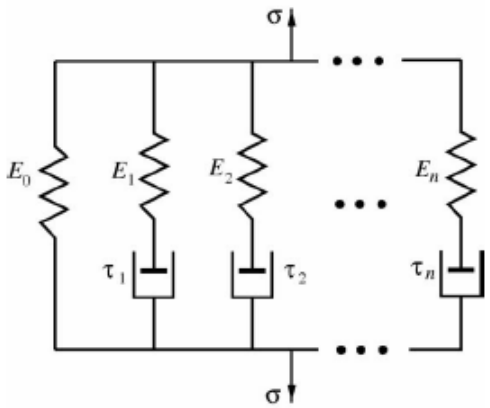

Figure 35. Wiechert model.

Total stress $\sigma(t)$ experienced by the specimen can be described by Weichert model as the following:

$$\sigma(t) = E(t)\varepsilon_{max} \tag{10}$$

Relaxation modulus $E(t)$ can be described by using the Prony series:

$$E(t) = E_0 + \sum_{i=1}^{n} E_i e^{-\frac{t}{\tau_i}} \tag{11}$$

where E_0 – relaxation modulus at time zero, t – time, τ_i – the relaxation time of ith dashpot, E_i – relaxation modulus of ith dashpot, ε_{max} – terminal strain applied to the specimen.

Relaxation modulus values from experimental data for dura mater can be used to find constants in the Prony series in Eq.(11). For that, we select twenty relaxation times and extract the corresponding relaxation modulus values from the experimental results as shown in Table 8.

Table 9. Relaxation modulus from the experiment of dura mater

Relaxation time	(s)	Relaxation modulus	(MPa)
τ_1	5	$E(\tau_1)$	0.467
τ_2	10	$E(\tau_2)$	0.393
τ_3	15	$E(\tau_3)$	0.354
τ_4	20	$E(\tau_4)$	0.333
τ_5	25	$E(\tau_5)$	0.31
τ_6	30	$E(\tau_6)$	0.3
τ_7	35	$E(\tau_7)$	0.29
τ_8	40	$E(\tau_8)$	0.28
τ_9	45	$E(\tau_9)$	0.28
τ_{10}	50	$E(\tau_{10})$	0.27
τ_{11}	55	$E(\tau_{11})$	0.263
τ_{12}	60	$E(\tau_{12})$	0.258
τ_{13}	65	$E(\tau_{13})$	0.256
τ_{14}	70	$E(\tau_{14})$	0.253
τ_{15}	75	$E(\tau_{15})$	0.247
τ_{16}	80	$E(\tau_{16})$	0.246
τ_{17}	85	$E(\tau_{17})$	0.241
τ_{18}	90	$E(\tau_{18})$	0.237
τ_{19}	95	$E(\tau_{19})$	0.232
τ_{20}	100	$E(\tau_{20})$	0.227

Following Table 8, we can construct the set of equations:

$$E_0 + E_1 + E_2 + \cdots + E_{19} + E_{20} = E(0) \tag{12}$$

$$E_0 + E_1 e^{-\frac{5}{5}} + E_2 e^{-\frac{5}{10}} + \cdots + E_{19} e^{-\frac{5}{95}} + E_{20} e^{-\frac{5}{100}} = E(5) = 0.467 \tag{13}$$

$$E_0 + E_1 e^{-\frac{10}{5}} + E_2 e^{-\frac{10}{10}} + \cdots + E_{19} e^{-\frac{10}{95}} + E_{20} e^{-\frac{10}{100}} = E(10) = 0.393 \tag{14}$$

$$E_0 + E_1 e^{-\frac{15}{5}} + E_2 e^{-\frac{15}{10}} + \cdots + E_{19} e^{-\frac{15}{95}} + E_{20} e^{-\frac{15}{100}} = E(15) = 0.354 \tag{15}$$

•

•

•

$$E_0 + E_1 e^{-\frac{95}{5}} + E_2 e^{-\frac{95}{10}} + \cdots + E_{19} e^{-\frac{95}{95}} + E_{20} e^{-\frac{95}{100}} = E(95) = 0.237 \tag{16}$$

$$E_0 + E_1 e^{-\frac{100}{5}} + E_2 e^{-\frac{100}{10}} + \cdots + E_{19} e^{-\frac{100}{95}} + E_{20} e^{-\frac{100}{100}} = E(100) = 0.227 \tag{17}$$

Solving Eqs. (12) - (17) results in determination of twenty-one coefficients $E_0 \ldots E_{20}$ (Table 10).

Table 11. Prony series' coefficients for dura mater

E_0	-1.88E+09	MPa	τ_0	0 s
E_1	2.28E+03	MPa	τ_1	5 s
E_2	-2.00E+06	MPa	τ_2	10 s
E_3	2.49E+08	MPa	τ_3	15 s
E_4	-7.95E+09	MPa	τ_4	20 s
E_5	7.9E+10	MPa	τ_5	25 s
E_6	-2.4E+10	MPa	τ_6	30 s
E_7	-3.8E+12	MPa	τ_7	35 s
E_8	2.29E+13	MPa	τ_8	40 s
E_9	-5.6E+13	MPa	τ_9	45 s
E_{10}	5.03E+13	MPa	τ_{10}	50 s
E_{11}	3.25E+13	MPa	τ_{11}	55 s
E_{12}	-1.1E+14	MPa	τ_{12}	60 s
E_{13}	1.29E+14	MPa	τ_{13}	65 s
E_{14}	-1.2E+14	MPa	τ_{14}	70 s
E_{15}	3.58E+13	MPa	τ_{15}	75 s
E_{16}	5.25E+13	MPa	τ_{16}	80 s
E_{17}	0.118693	MPa	τ_{17}	85 s
E_{18}	-6.8E+13	MPa	τ_{18}	90 s
E_{19}	3.3E+13	MPa	τ_{19}	95 s
E_{20}	0	MPa	τ_{20}	100 s

Thus, Prony series in Eq.(11) takes the following form:

$$E(t) = -1.88 \cdot 10^9 + 2.28 \cdot 10^3 e^{-\frac{t}{5}} - 2 \cdot 10^6 e^{-\frac{t}{10}} + 2.49 \cdot 10^8 e^{-\frac{t}{15}} - 7.95 \cdot 10^9 e^{-\frac{t}{20}} + 7.9 \cdot 10^{10} e^{-\frac{t}{25}} - 2.4 \cdot 10^{10} e^{-\frac{t}{30}} - 3.8 \cdot 10^{12} e^{-\frac{t}{35}} + 2.29 \cdot 10^{13} e^{-\frac{t}{40}} - 5.6 \cdot 10^{13} e^{-\frac{t}{45}} + 5.03 \cdot 10^{13} e^{-\frac{t}{50}} + 3.25 \cdot 10^{13} e^{-\frac{t}{55}} - 1.1 \cdot 10^{14} e^{-\frac{t}{60}} + 1.29 \cdot 10^{14} e^{-\frac{t}{65}} - 1.2 \cdot 10^{14} e^{-\frac{t}{70}} + 3.58 \cdot 10^{13} e^{-\frac{t}{75}} + 5.25 \cdot 10^{13} e^{-\frac{t}{80}} + 0.119 e^{-\frac{t}{85}} - 6.8 \cdot 10^{13} e^{-\frac{t}{90}} + 3.3 \cdot 10^{13} e^{-\frac{t}{95}} + 0 e^{-\frac{t}{100}}$$

The experimental and predicted values of the relaxation modulus are shown in Fig. 36.

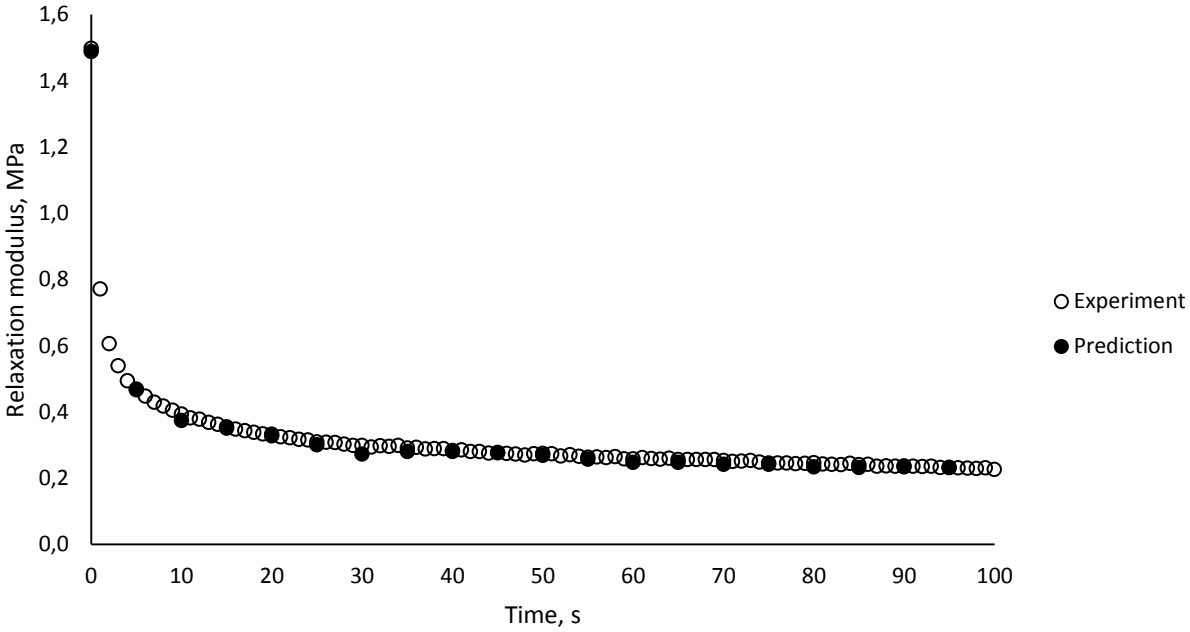

Figure 36. Relaxation modulus

It can be seen that experimental data could be well predicted by the determined relaxation times τ_i and corresponding coefficients E_i, and will be used as an input into FEM software (ANSYS Mechanical) for further analysis.

A similar procedure was conducted on the stress relaxation test results of the sclera in this study and the following constants were obtained:

Table 12. Prony series' coefficients for the sclera:

E_0	MPa	2.61E+09	τ_0	0 s
E_1	MPa	-1.94E+03	τ_1	5 s
E_2	MPa	1.68E+06	τ_2	10 s
E_3	MPa	-1.66E+08	τ_3	15 s
E_4	MPa	2.23E+09	τ_4	20 s
E_5	MPa	7.22E+10	τ_5	25 s
E_6	MPa	-1.8E+12	τ_6	30 s
E_7	MPa	1.6E+13	τ_7	35 s
E_8	MPa	-6.7E+13	τ_8	40 s
E_9	MPa	1.41E+14	τ_9	45 s
E_{10}	MPa	-1.2E+14	τ_{10}	50 s
E_{11}	MPa	-5.8E+13	τ_{11}	55 s
E_{12}	MPa	1.81E+14	τ_{12}	60 s
E_{13}	MPa	-1.4E+14	τ_{13}	65 s
E_{14}	MPa	1.19E+14	τ_{14}	70 s
E_{15}	MPa	-9E+13	τ_{15}	75 s
E_{16}	MPa	-1.3E+13	τ_{16}	80 s
E_{17}	MPa	-0.12627	τ_{17}	85 s
E_{18}	MPa	6.91E+13	τ_{18}	90 s
E_{19}	MPa	-3.7E+13	τ_{19}	95 s
E_{20}	MPa	0	τ_{20}	100 s

5.5 Results

Results were taken for 1) models with all linear elastic properties and 2) for FEM models with viscoelastic properties for sclera and dura mater.

5.5.1 FE models with all linear elastic material properties

The simulation results with linear elastic material properties are mainly presented in the form of strain distributions within lamina cribrosa volume. In Fig.

37, we include our results for all models (patient-specific and generic) with an IOP and ICP value equal to 25 mmHg and 5 mmHg, respectively. The depicted curves capture the percentage of lamina cribrosa volume (y-axis) exhibiting a deformation greater than the corresponding strain value along the x-axis. For instance, point A in Fig. 37a can be interpreted as 60% of lamina cribrosa's volume for the 5th model exhibits a deformation, which is greater than 2.8% of the maximum shear strain.

The histograms for maximum principal and maximum shear strain values in lamina cribrosa are shown in Figure 38. Strain values between 3% and 4% are exhibited for around 40% of lamina cribrosa's volume for all patient-specific models (with some slight variations), whereas the generic model exhibits a significantly higher volume percentage (~64%) for this strain range. In the maximum principal strain histogram (Fig. 38b), although variations exist among the examined models, the 1-1.5% strain range is the prevailing one in all cases.

In Fig. 39, strain distributions within the lamina cribrosa are depicted for the generic model, and patient-specific models 2 and 5, for varying ICP values (5 mmHg, 10 mmHg, and 15 mmHg) and a constant IOP value of 25 mmHg. This study focuses on the effect of ICP on LC deformation under constant IOP, which results in translaminar pressure differences (TLPD = IOP-ICP) of 20 mmHg, 15 mmHg, and 10 mmHg. All models (generic and the 6 patient-specific ones) demonstrated the same behavior, i.e., deformations follow the increase in TLPD; however, we display in Fig. 39 only two patient-specific models, which exhibit the least and most prominent deviation from the generic model's behavior.

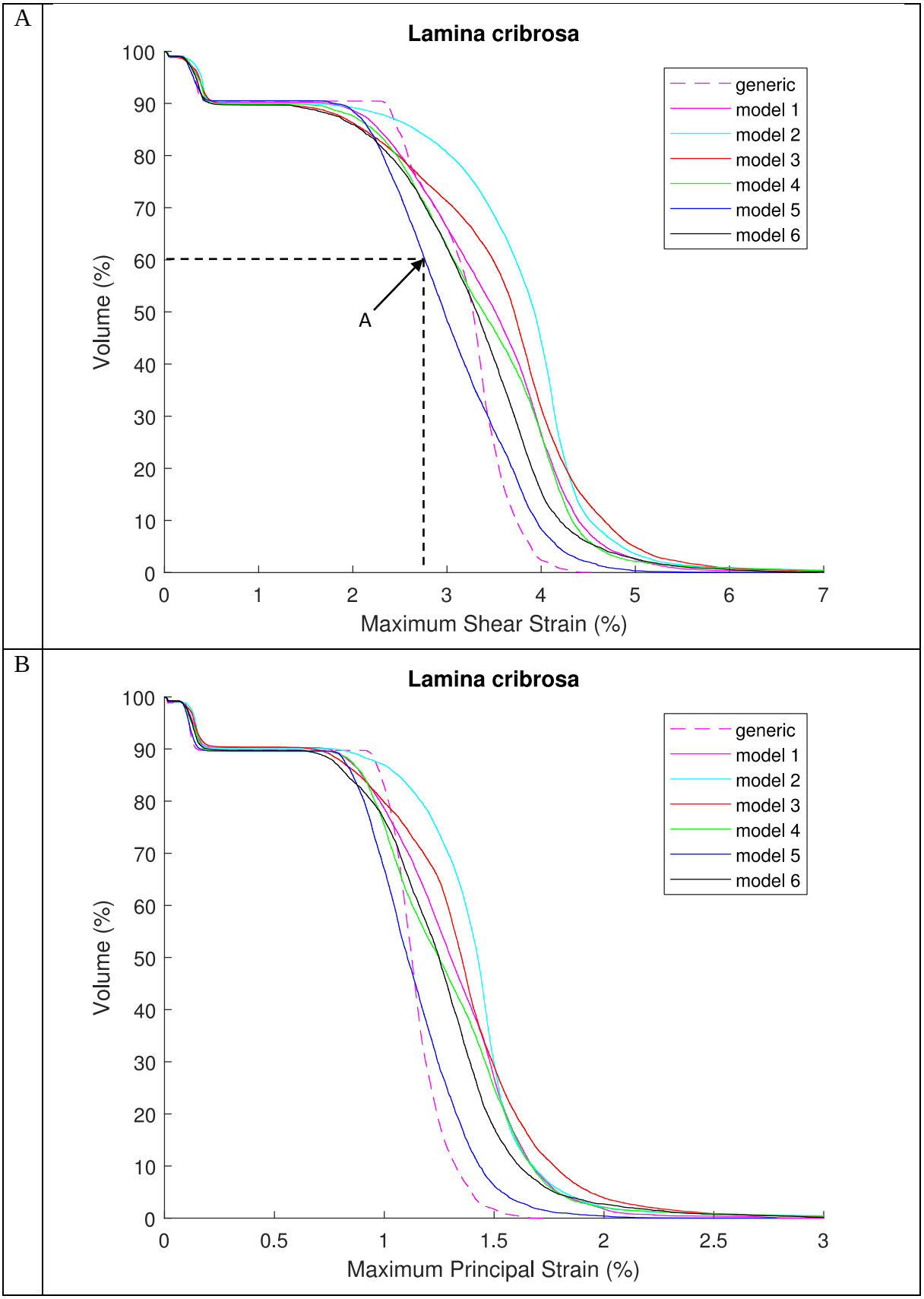

Figure 37. Strain distribution across LC volume.

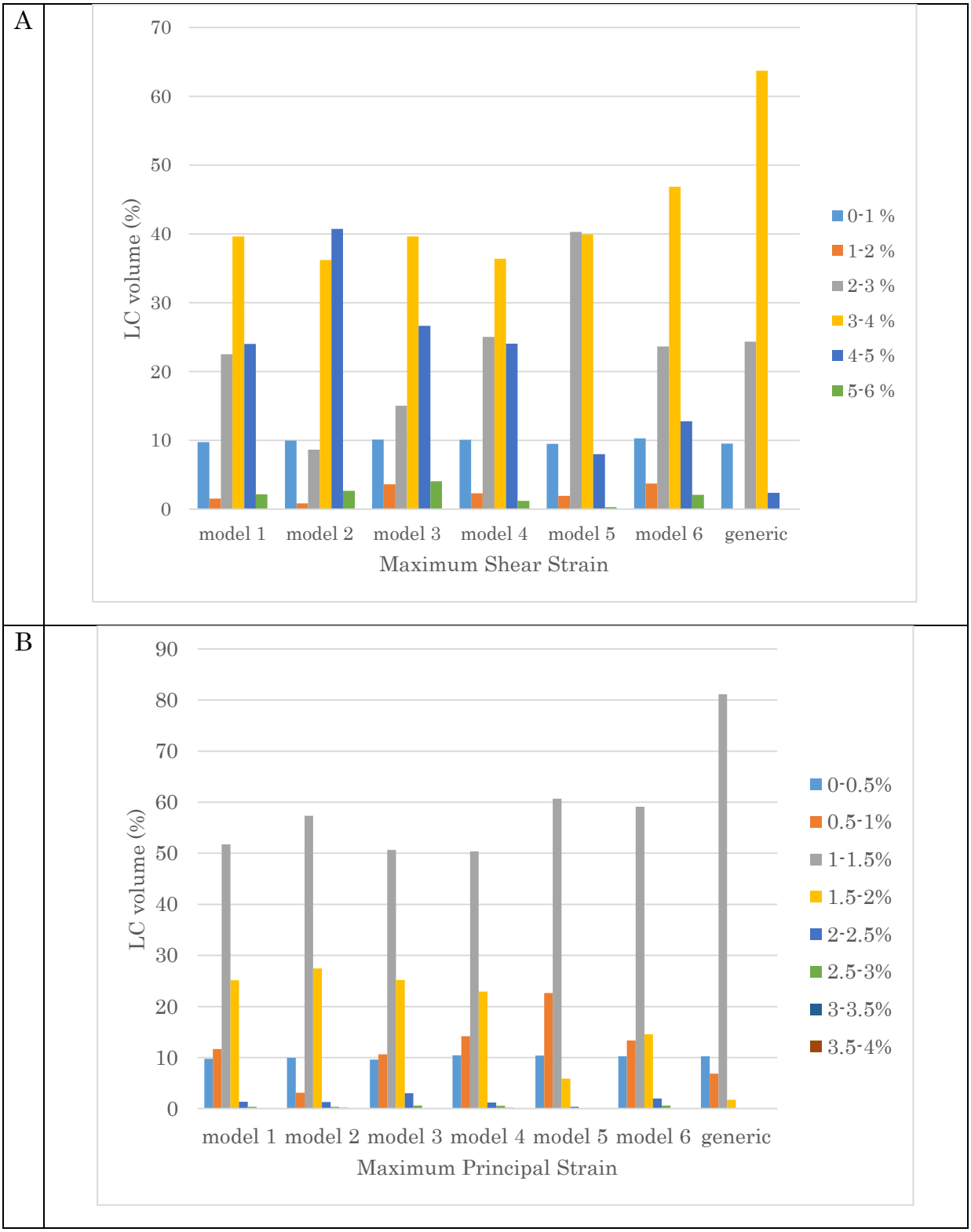

Figure 38. Lamina cribrosa volume and corresponding percentage strains

A

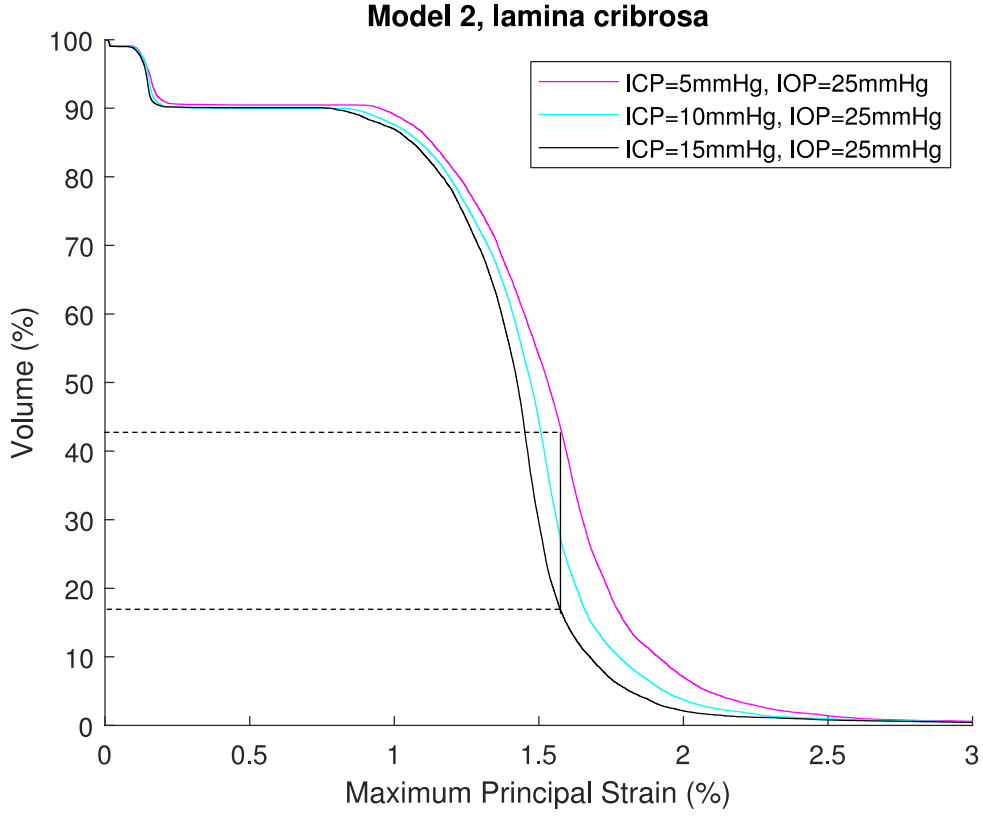
Model 2, lamina cribrosa
ICP=5mmHg, IOP=25mmHg
ICP=10mmHg, IOP=25mmHg
ICP=15mmHg, IOP=25mmHg
Volume (%)
Maximum Principal Strain (%)
0
10
20
30
40
50
60
70
80
90
100
0
0.5
1
1.5
2
2.5
3

B

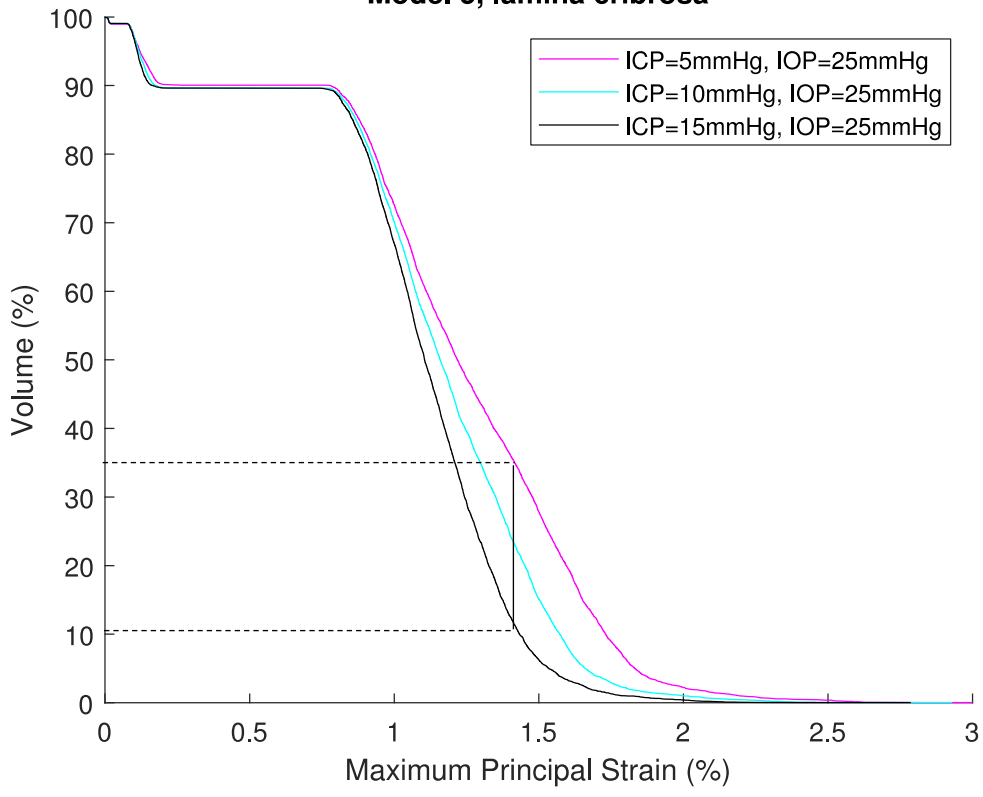
Model 5, lamina cribrosa
ICP=5mmHg, IOP=25mmHg
ICP=10mmHg, IOP=25mmHg
ICP=15mmHg, IOP=25mmHg
Volume (%)
Maximum Principal Strain (%)
0
10
20
30
40
50
60
70
80
90
100
0
0.5
1
1.5
2
2.5
3

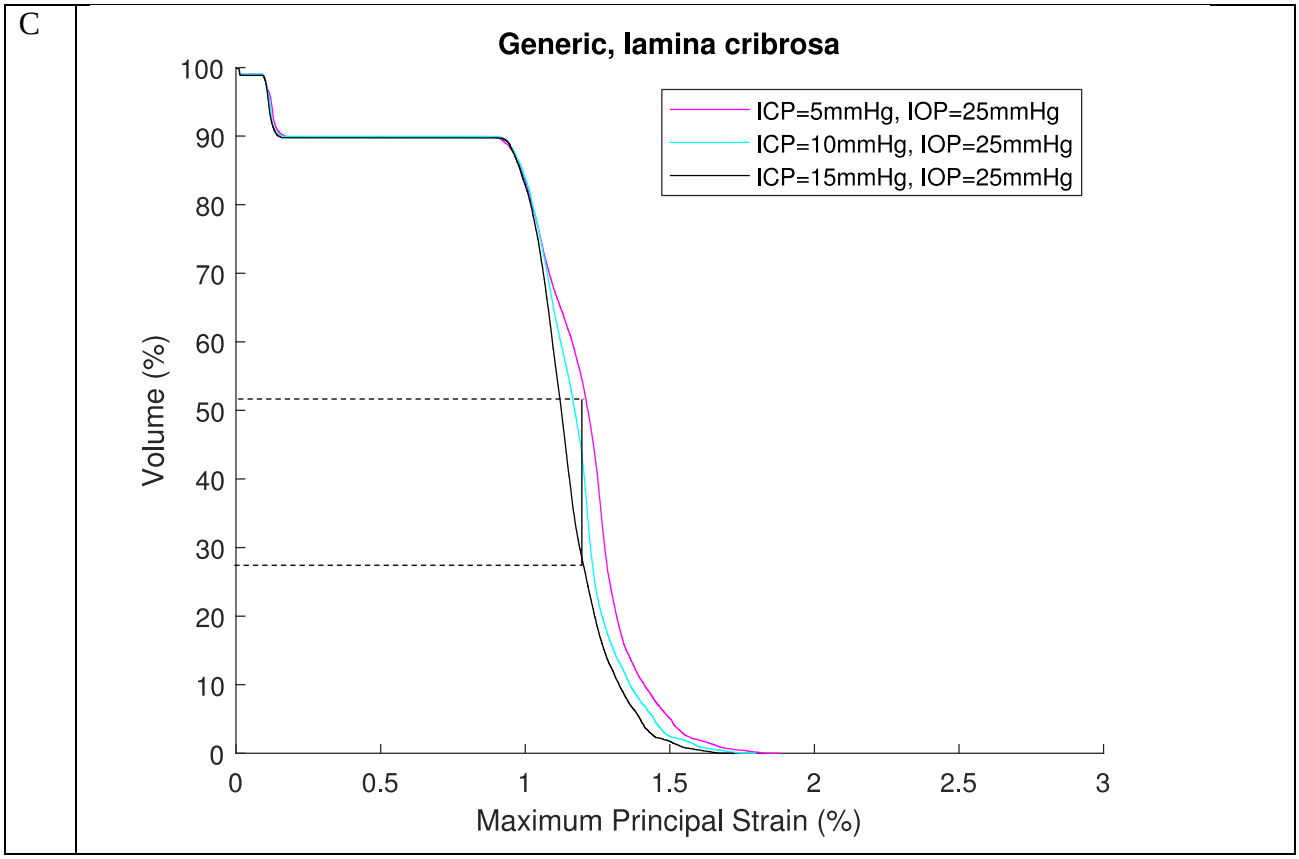

Figure 39. Effect of ICP on LC deformation

Finally, the simulations were carried out further for a fixed TLPD value of 10 mmHg and varying values for both IOP and ICP. A lower IOP induces generally smaller strains, as expected; however, keeping the TLPD fixed maintains the exhibited variation interval for all models as can be observed in Fig. 40, where the low IOP curves are practically left-shifted versions of the higher IOP ones. If we compare these results with the previous ones, we may argue that an elevated IOP dominates the phenomenon and TLPD values бидetermine the distribution of strains in the area of interest.

A

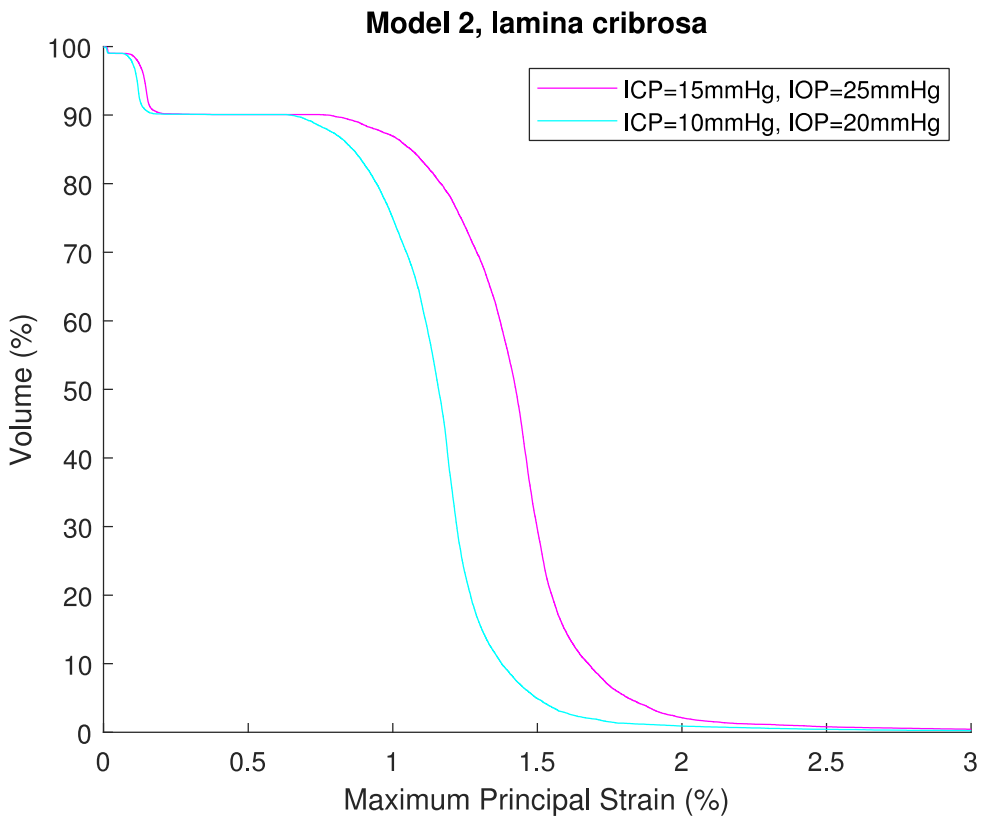
Model 2, lamina cribrosa
ICP=15mmHg, IOP=25mmHg
ICP=10mmHg, IOP=20mmHg
Volume (%)
Maximum Principal Strain (%)
0
10
20
30
40
50
60
70
80
90
100
0
0.5
1
1.5
2
2.5
3

B

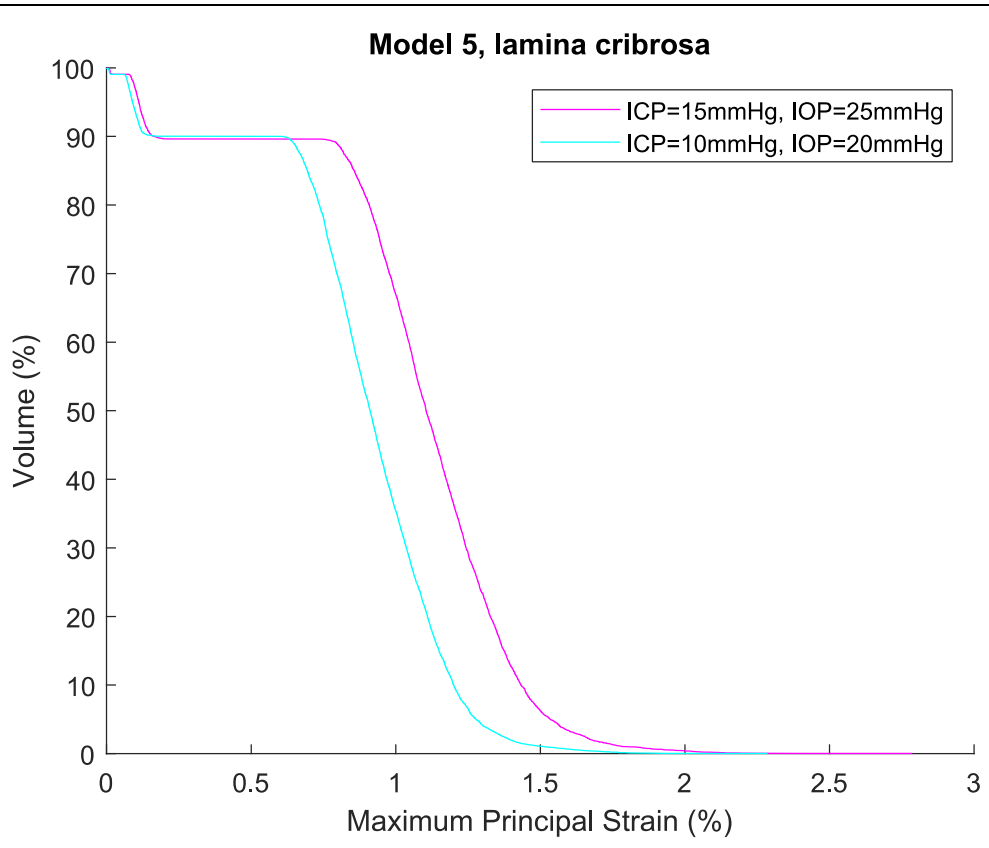
Model 5, lamina cribrosa
ICP=15mmHg, IOP=25mmHg
ICP=10mmHg, IOP=20mmHg
Volume (%)
Maximum Principal Strain (%)
0
10
20
30
40
50
60
70
80
90
100
0
0.5
1
1.5
2
2.5
3

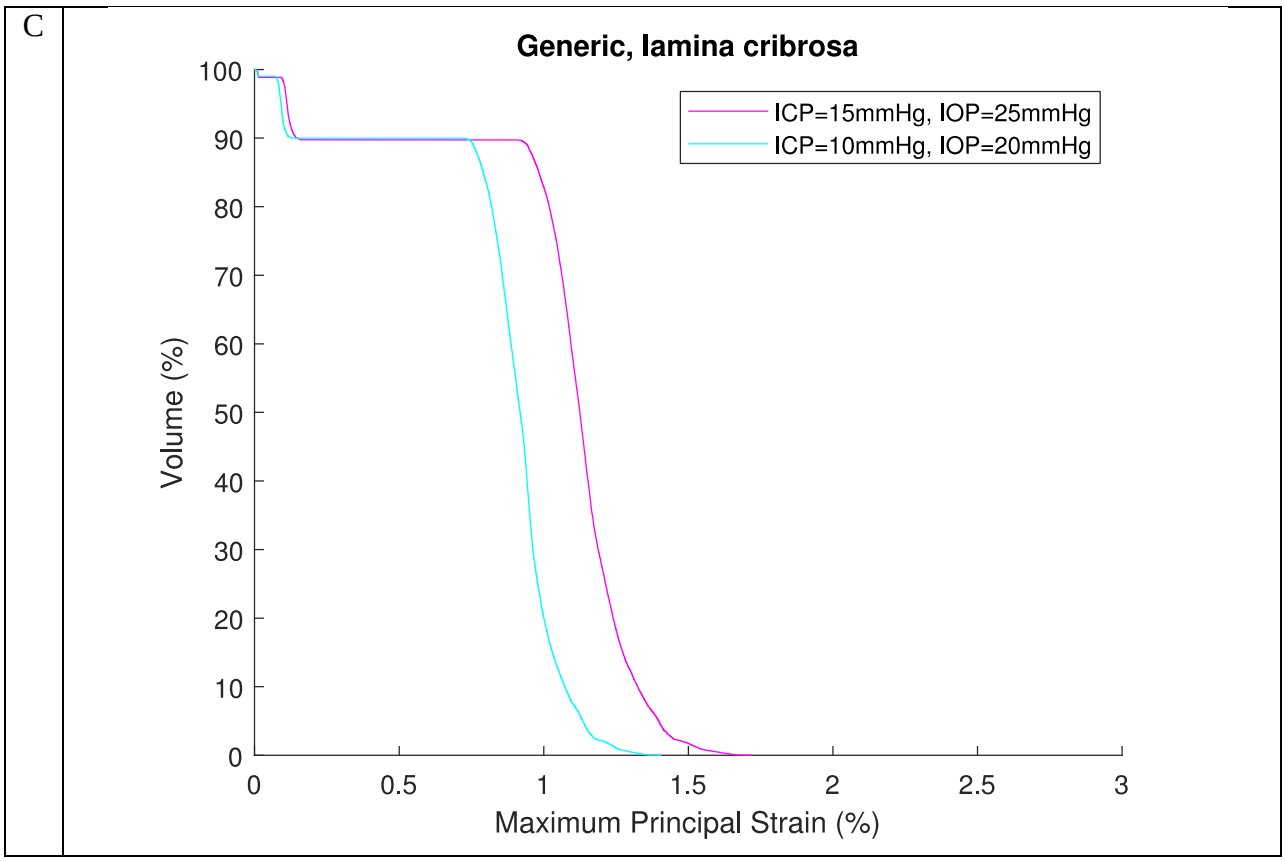

Figure 40. Strain distributions for TLPD = 10 mmHg

5.2.2. FE models with viscoelastic material properties for sclera and dura mater

To check the effect of viscoelastic material properties, we modeled sclera and dura mater as viscoelastic with the generic model. Prony series coefficients for sclera and dura mater were taken from table 9 and table 10. Viscoelastic properties were given from our experiment described above whereas the linear elastic part for sclera was 6MPa, dura mater was 4.5 MPa. Results for four cases of prescribed material properties are shown in figure 41 below. For the first case, all material properties were linear elastic. For the second case, sclera was simulated as viscoelastic from the experiment and all other materials were linear elastic taken from table 1. For the third case, dura mater was viscoelastic, and all others were

linear elastic and for the fourth case both dura and sclera were viscoelastic, and all others were linear elastic. From figure 41 A and B, it can be easily seen that change in ICP had greatly lowered strains in the lamina cribrosa. Figure 41 C and D show the relative percentage difference with models with all linear elastic. It is clear from C and D that the difference was greatest when ICP of 7mmHg was given especially for minimum principal strain. The relative percentage difference was zero when the dura mater was modeled as viscoelastic and ICP was set to 0 mmHg (Figure 41c). In general, the viscoelastic properties of the dura mater were not influential like sclera. Viscoelastic properties of sclera had the greatest relative difference when ICP was 7 mmHg.

A

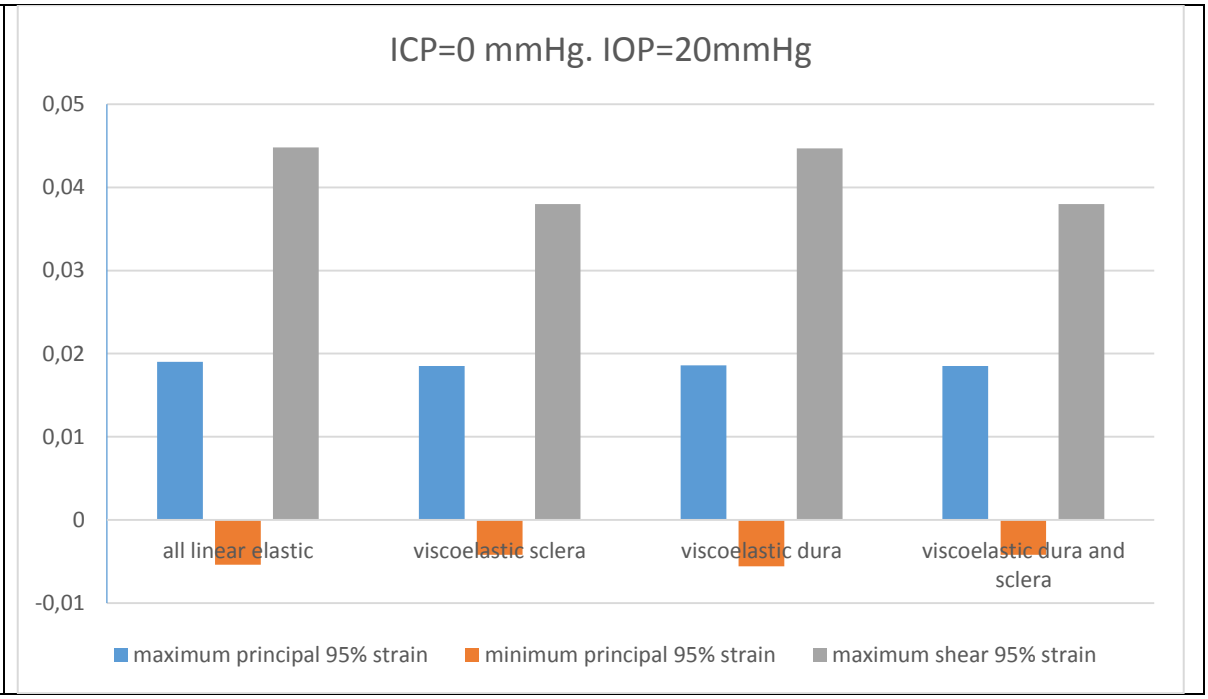

B

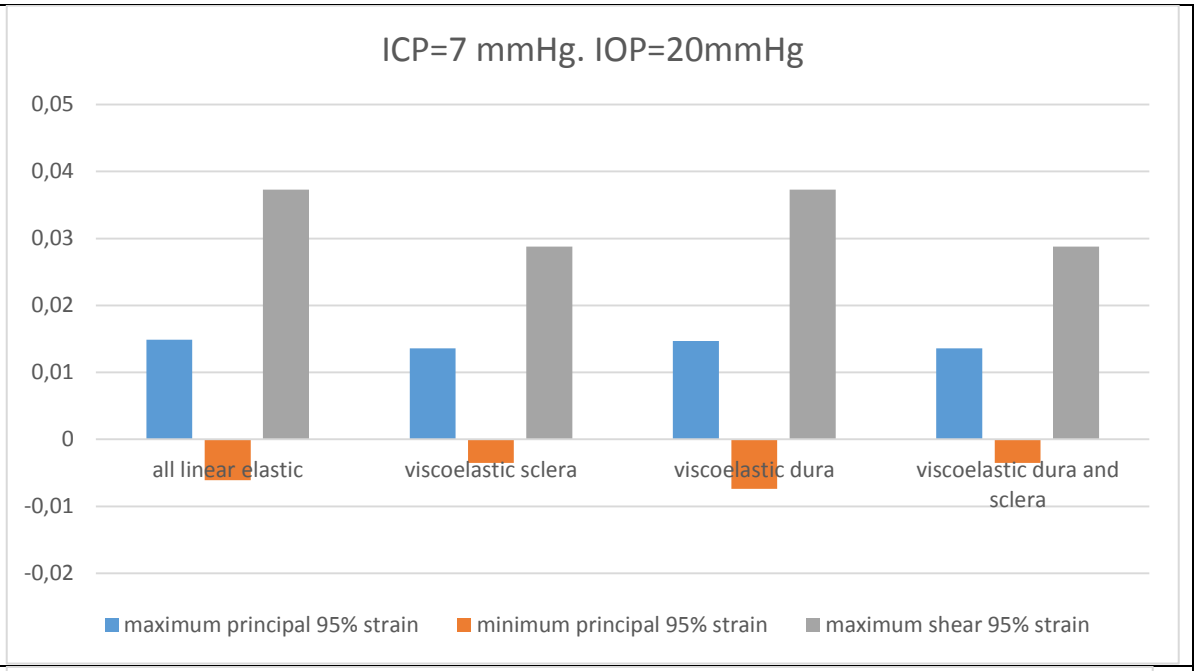
ICP=7 mmHg. IOP=20mmHg
0,05
0,04
0,03
0,02
0,01
0
-0,01
-0,02
all linear elastic
viscoelastic sclera
viscoelastic dura
viscoelastic dura and sclera
maximum principal 95% strain
minimum principal 95% strain
maximum shear 95% strain

C

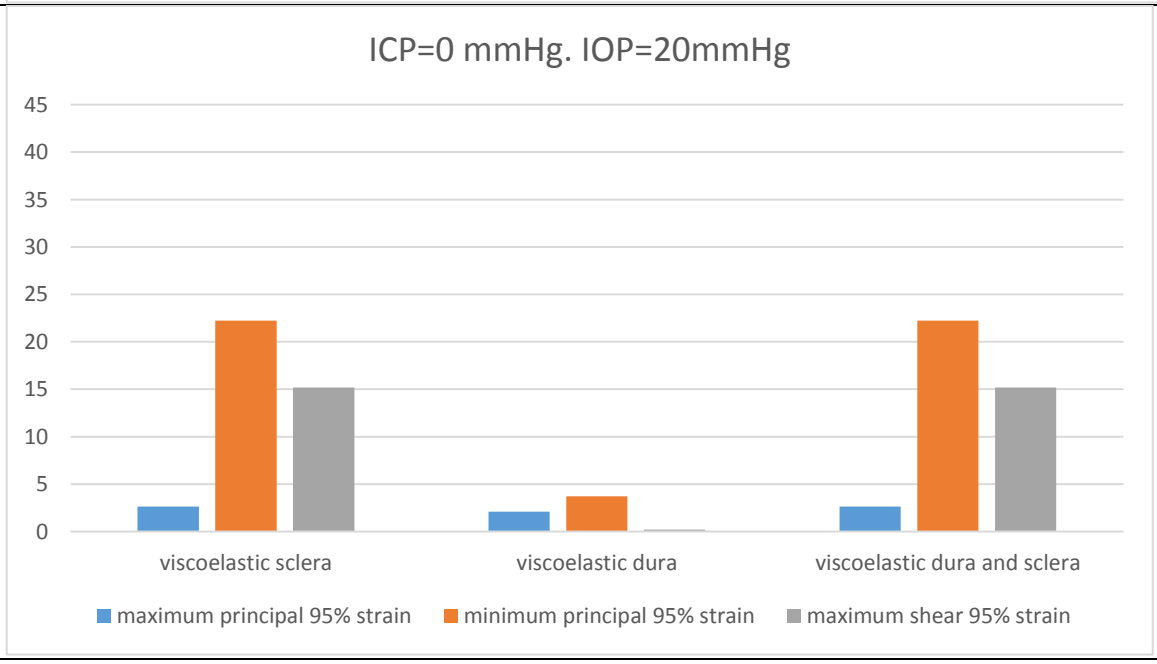
ICP=0 mmHg. IOP=20mmHg
45
40
35
30
25
20
15
10
5
0
viscoelastic sclera
viscoelastic dura
viscoelastic dura and sclera
maximum principal 95% strain
minimum principal 95% strain
maximum shear 95% strain

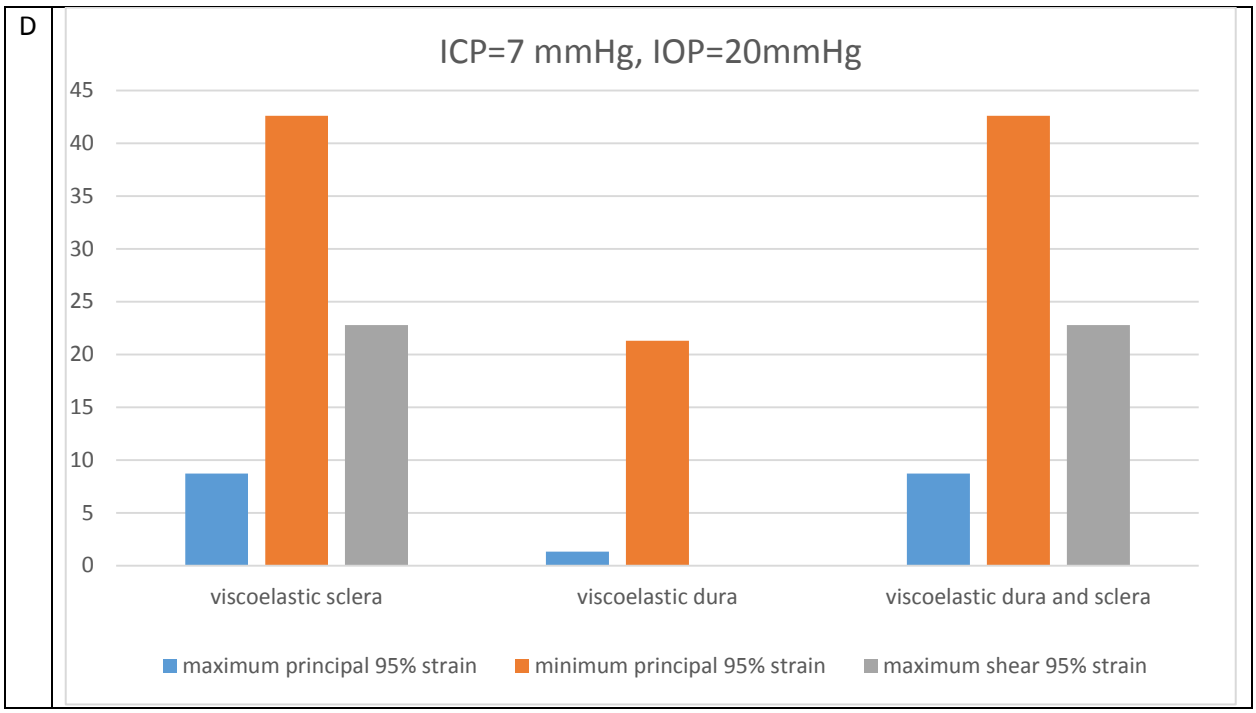

Figure 41. Effect of linear elastic and viscoelastic material properties a) ICP=0mmHg and b) ICP=7mmHg

5.6 Discussion

The aim of the chapter was twofold: 1) check the effect of patient-specific geometry in connection with elevated IOP/ICP induced stresses on ONH biomechanics; 2) check the effect of non-linear (viscoelastic) material properties on ONH biomechanics at certain levels of IOP/ICP.

5.6.1 Effect of ONH geometry

To check the effect of patient-specific ONH geometry results from finite element simulations using patient-specific and generic ocular models were provided to study the effect of intracranial/intraocular pressure on ONH biomechanics. By

patient-specific, we mean only the reconstructed optic nerve head geometry taken from OCT images embedded into the generic corneoscleral shell. Dura mater, PLNT, and pia were also generic. All models exhibit a similar strain pattern for both shear and principal strains (Figs. 37a,b). One of the characteristic features of all curves is a small flat area in the beginning and a larger, more prominent one later, which corresponds to around 90% of LC's volume. For this case, it can be inferred from our graphs that the major part of lamina cribrosa experiences strains that correspond to 2.5-5.5% of the maximum shear strain and 1-2% of the maximum principal strain. For both shear and principal strains, the generic model (dashed line) produces a generally steeper curve that corresponds to a narrower range of strain values when compared to the patient-specific models. This result provides evidence that the idealized geometry of a simple generic model cannot accurately capture the more widespread distribution of strains within the lamina cribrosa of real patients. Furthermore, the generic model seems to underestimate the upper bound of this strain range that is even more worrying as it can undermine its applicability in real-life patients.

The graphs in Fig. 39 shows that ICP's effect is more distinguished in the higher strain regions. For instance, 18% of the 2nd model's LC volume exhibits principal strains above 1.6% for a TLPD value equal to 10 mmHg, while this volume increases up to 42% when TLPD becomes 20 mmHg (Fig. 39a). The same increase in TLPD results in a jump from 10% to 35% for the volume of LC exhibiting strains above 1.4% for model 5 (Fig. 39b). Although we can also record the same type of change in strain distributions for the generic model (Fig 39c), it seems to be less

affected by the ICP's change as all curves are squeezed together. This study demonstrates that a decrease in ICP[3] will always bring an adverse effect in strain distributions with these effects being inadequately captured by the generic model.

5.6.2 Effect of viscoelastic material properties.

It is common practice to use all linear elastic material properties to study ocular biomechanics for simplification [45, 69, 87]. Other researchers also use non-linear material properties including hyperelastic material properties [130, 131] or even viscoelastic material properties in dynamic simulations [47]. We tried to understand how this simplification of linear material properties may give distorted results. It is well known that sclera material properties play an important role in ocular biomechanics [132] while dura mater material properties also play a prone role with induced ICP. Therefore, linear viscoelastic material properties of sclera and dura mater were extracted from stress relaxation tests. Results with viscoelastic material properties of sclera showed substantial difference with the results taken with all linear elastic properties. Inducing ICP increased the difference between strain results taken with linear and viscoelastic material properties. We believe that for dynamic time-dependent simulations, for example, when studying the effect of heart pulse on ONH, these differences maybe even higher.

[3] Under a constant IOP value of 25mmHg.

5.6.2. Limitations

Several limitations arise from our work. First, material properties were linear while it should be viscoelastic. Second, we only modeled ONH as patient-specific while sclera geometry and thickness also play a role especially peripapillary sclera [132]. Third, while comparison results of our patient-specific model did not have the greatest difference and in general agrees well with the generic model (which was validated by Sigal et al. [43]) it was not fully validated. Fourth, our viscoelastic properties were taken from ewes, future models should include the viscoelastic properties of human eyes. Fifth, it is also well known that IOP is pulsatile [133] while we modeled as static, future models should include dynamic time-dependent simulations with pulsatile IOP/ICP. Sixth, all tissues were assumed isotropic, however, several studies have shown that sclera is anisotropic especially in the peripapillary region [54, 134]. Seventh, we have experimentally measured biomechanical properties of ewe sclera and dura sheath only in the longitudinal direction. Collagen fibers in dura mater are mainly oriented axially when the tissue was loaded [135]. Future experiments on dura sheath should include quantifications of interactions between tissue deformations in the axial and circumferential dimensions. It is also possible that dura exhibits different biomechanical properties across different species.

5.7 Conclusion

In summary, this study highlights at least four different aspects that we believe deserve further consideration and investigation. First, although all employed

models were simulated with identical material properties, loads, and boundary conditions, strain estimations exhibited clear differences. This certainly indicates that ONH geometry does have a measurable effect on ONH biomechanics despite being rather modest in magnitude. Secondly, an increase in translaminar pressure difference is always followed by an increase in calculated strains. Moreover, this effect seems dependent on the geometry of the ONH models as calculations on patient-specific models have revealed a wider range of deformations in comparison to the generic case. Third, although IOP levels determine the magnitude of strain levels, their exact distribution is co-determined by the TLPD, i.e., the ICP value, when IOP remains fixed. Fourth, the difference between strains in models with linear elastic and viscoelastic properties was substantial especially for sclera; future models must incorporate viscoelastic material properties. All these observations require further investigation to fully capture and understand the mechanisms involved so that we can ultimately assess their significance in the identification of the conditions that lead to glaucoma.

Chapter 6. Statistical shape modeling of the optic nerve head

Optic nerve head morphology governs how mechanical stresses distribute, population-based models have the potential to be a powerful tool to understand glaucoma mechanism. Nevertheless, the development of a completely parameterized eye model with precise geometry remained a challenge. The current chapter used an automated segmentation algorithm to segment retinal pigment epithelium and internal limiting membrane layers with manually segmented lamina cribrosa anterior/posterior surface to create a statistical shape model of the optic nerve head for 26 patients. We analyzed ONH shape principal components biomechanically, qualitatively and quantitatively. Qualitative assessment was performed visually, quantitative analysis was implemented counting anatomical measurements. FE models were built using 3D reconstructions of ONHs from principal components. The reconstructed models were then analyzed biomechanically using the FE method. The method described herein describes a method which we believe will advance parametrized FE populations-specific ocular modeling in the future.

6.1. Introduction

Shape, as reported in pertinent literature and mentioned throughout this thesis, plays an important role in studying ocular biomechanics. We have so far used generic and patient-specific models to represent ONH geometry for finite element modeling in biomechanics. Specifically, in Chapter 3, a generic model was used with components geometry and mechanical properties according to averages reported in the pertinent literature. The employed geometry, in this case, is rather simplistic and does not include the shape complexity found in real layers. However, this simplicity allows its efficient parameterization, which is a powerful feature when factors affected eye biomechanics need to be identified. However, in some cases, the analysis of a generic model cannot produce accurate predictions regarding the biomechanics of a specific human eye. In Chapter 5, patient-specific models were developed to capture the corresponding ONH structures and better predict their biomechanics. However, patient-extracted models correspond to a specific, generally complicated geometry that hinders its parametrization and generation of geometric variations that would allow predictions for a bigger set of patients. Developing a fully-parametrized ocular model that can address both the needs of realistic geometry and application to a wide range of patients remains a challenge [127, 136]. Statistical shape modeling (SSM) has the potential to address this challenge and our focus in this chapter is to create and evaluate such a modeling approach.

SSM is a well-established technique to represent morphological variations in a population. SSM uses principal component analysis (PCA) to determine the normal shape variation among the class of training sets of data, which are then used as prior knowledge in an algorithm [137]. SSM has several applications in biomechanics from automatic segmentation in medical image processing to the creation of finite element models for the design of implants and surgery planning [138]. This method has been successfully applied to study the influence of shape in femur, tibia, knee, nasal cavity, liver and brain biomechanics; see [139, 140]. Furthermore, an SSM of the cornea-scleral shell was recently developed in [141], but the primary focus of that model was to segment the human eye in 3D magnetic resonance imaging for treatment planning in retinoblastoma. To the best of our knowledge, no SSM of eye or ONH has been previously used in FE modeling or biomechanical analysis.

6.2 Materials and Methods

Optical coherence tomography scans of optic nerve head B scans of 26 patients were analyzed. The internal limiting membrane was segmented using our developed hybrid algorithm [142]. Retinal pigment epithelium (RPE), anterior and posterior lamina cribrosa boundaries were segmented manually after application of the compensation algorithm in [143] to increase LC visibility. Each segmented layer is described with a fixed number of points (n=9882) in Cartesian coordinates (x_i, y_i),

i=1, 2, 3 n. After delineation, sections were rotated using the corresponding rotation matrix (see Eq. 8 in Chapter 4). The resulting sets of points are depicted in Fig. 42.

The statistical shape model was built based on these landmark identification point-sets. Specifically, each point-set was represented by a shape vector ($\boldsymbol{v}$) containing the complete set of point coordinates; see Eqs. 18, 19, 20. Finally, all shape vectors can be arranged as columns in the matrix representing the complete set of samples, $\mathbf{S} = (\mathbf{s}_1, \mathbf{s}_2, \ldots \mathbf{s}_{ns})$.

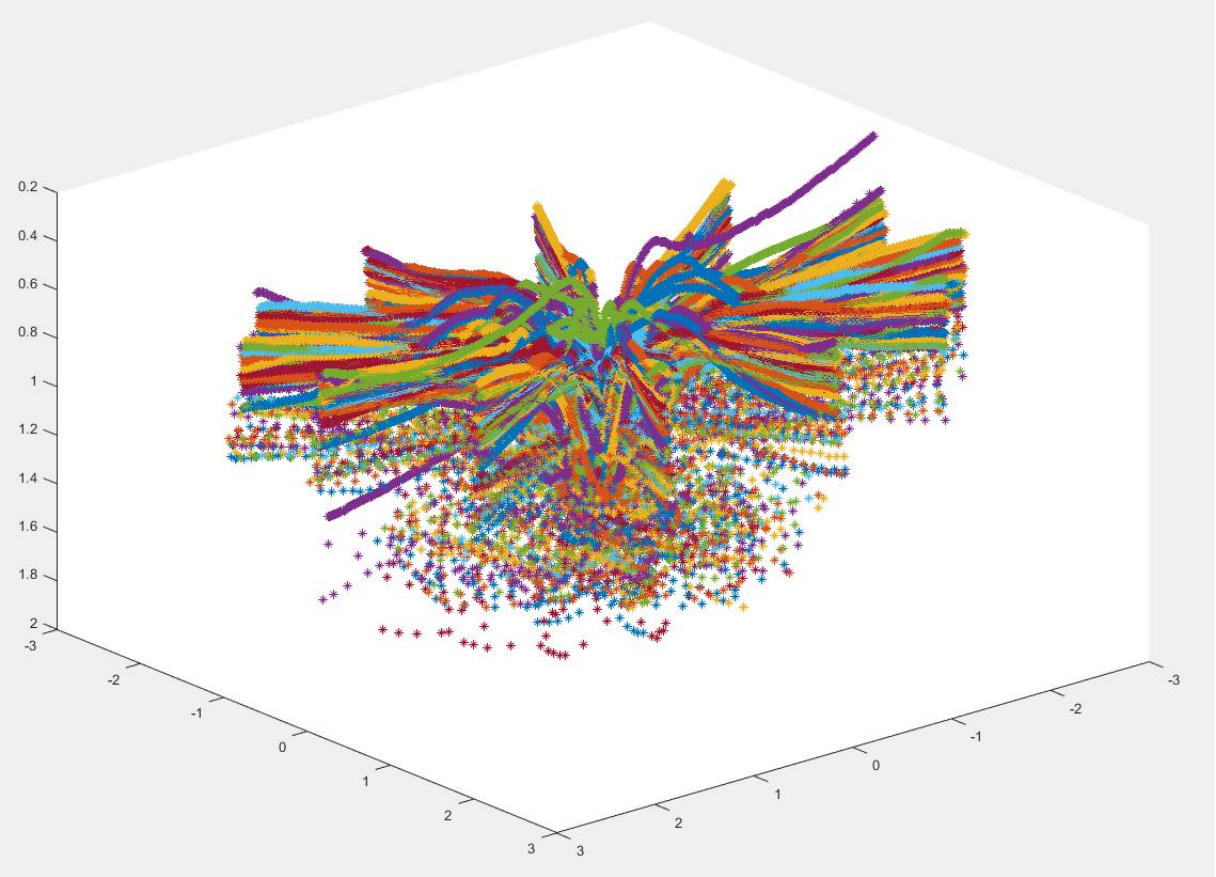

Figure 42. Segmented points for all 26 patients in one image.

$$\boldsymbol{x}=(x_1, x_2, \ldots x_n)^T \quad (18)$$

$$\boldsymbol{y}=(y_1, y_2, \ldots y_n)^T \quad (19)$$

$$\boldsymbol{x}=(z_1, z_2, \ldots z_n)^T \quad (20)$$

$$\boldsymbol{v} = \begin{pmatrix} \boldsymbol{x} \\ \boldsymbol{y} \\ \boldsymbol{z} \end{pmatrix}$$

The segmented points were aligned with an iterative approach that realigns data, excludes outliers and eliminates misplacements due to rotations and translations; see [144].

6.2.1 Statistical shape model creation

Principal component analysis using Singular Value Decomposition (SVD) was the next step performed resulting in the ONH shape model $\boldsymbol{s}$ and an orthogonal set of principal components (shape modes) [139]. The required calculations for SSM generation were carried out in MATLAB (2018a, MathWorks). The resulting modes / principal components can be linearly combined to produce any number of varying virtual specimens. Specifically,

$$\boldsymbol{s} = \overline{\boldsymbol{s}} + \boldsymbol{P}\boldsymbol{b}, \qquad (21)$$

where

$$\boldsymbol{b} = \boldsymbol{P}^T(\boldsymbol{s} - \overline{\boldsymbol{s}}). \qquad (22)$$

In the equations above, $\overline{\boldsymbol{s}}$ is the mean shape, $\boldsymbol{b}$ is the weighting shape vector, and P is the orthogonal shape variations matrix which contains eigenvectors of the covariance matrix. Commonly, $\boldsymbol{b}$ is limited to the range ±3 times the standard deviation $\sqrt{\lambda_i}$ (λ is the corresponding eigenvalue), so that it can generate shapes similar to these in the training set. The mean shape $\overline{\boldsymbol{s}}$ can be calculated as follows

$$\overline{s} = \frac{1}{n_s}\sum_{i=1}^{n_s} s_i, \qquad (23)$$

where n_s is the number of point-sets used in the process. Singular Matrix Decomposition (SVD) can be used to extract statistic weight and shape variation using the following equation:

$$S = UKV^T \qquad (24)$$

where K contains the singular values of S on the diagonal, and V and U are orthogonal matrices.

6.2.2 Model evaluation

The generalization ability and its compactness were used to evaluate the generated SSM model; see [145–147]. Generalization is the ability of the model to reconstruct unseen instances in the class of the sample (training) set and this is an important property as our goal is to be able to generate the geometrical variations exhibited in a big population. Generalization *(H)* was checked using a leave-one-out reconstruction. This means that an SSM was built by all than one patient dataset and the left-out member was fitted with the shape model. Deviations are measured using the Euclidean distance between shape vectors. The pseudo-code of the process is shown below:

For *J=1…n-2*

For *K=1…n*

Build SSM from the training set with leave one outpatient data $\boldsymbol{s_k}$;

Reconstruct the left outpatient data using J shape parameters:

$$s_k'(J) = \overline{s_k} + \sum_{l=1}^{J} P_k^m \, b_k^m$$

Calculate the sum of squares approximation error:

$$\varepsilon^2(J) = |s_k - s_k'|^2$$

End of *K*

Calculate the l^2 norm:

$$H(J) = \sqrt{\sum_{J=1}^{n} \varepsilon^2(J)}$$

End of *J*

where J represents the number of shape modes used each time and K runs over the number of sample datasets.

Compactness (S) is a measure of efficiency corresponding to the number of parameters needed to reconstruct the same models or variance. It is calculated as a plot of cumulative variance.

$$S(J) = \sum_{n=1}^{J} \lambda^n, \qquad (25)$$

where $S(J)$ is the cumulative variance and ϕ is the n^{th} largest eigenvalue of the J^{th} principal component.

6.2.3 Shape analysis

SSM model produces the principal components (modes) which allow the variation in the shape space. The SSM was analyzed biomechanically, quantitatively, and qualitatively. Qualitative assessment of SSM is usually performed by visual inspection of the modes [139, 148–150]. Standard deviations (SD) of ±3 for the first five principal components were inspected visually for qualitative assessment.

Using the SSM model, the required instances were built and their landmarks/points were used for analysis as in Chapter 5; see 5.2.2 for more details. This resulted in a finite element model for biomechanical analysis for each of the model instances. These models were then used in anatomical measurement and quantitative analysis. Quantitative assessment complements the visual qualitative assessment. Anatomical measurements of ±3 SD of each shape mode and mean shape were performed in quantitative analysis. A percentage contribution parameter was calculated as follows to analyze the influence of each shape mode on variation in anatomical measurements:

$$R=Abs(M_{n+}-M_{n-}) \qquad (26)$$

$$\%C = \frac{R_n}{\sum_{i=1}^{N} R_i} \qquad (27)$$

Where M is the anatomical measurement associated with ±3 SD of that PC, n is the number of principal components of interest, R is the total range of the M for principal component n. Overall, 15 principal components were calculated.

The SSM's biomechanical analysis was done by running finite element simulations with models following methodology described in chapter 5. Linear combination of mean shape and principal components can produce any number of virtual specimens which represents normal anatomical variation. A total of 22 FE ocular models based on ±3 standard deviations of the 11 principal components were generated. Linear elastic material properties were used for all calculations as in Table 1 and, as previously, all simulations were run in Ansys 19 (ANSYS, Canonsburg, PA). Each generated ONH ±3 SD shape modes were three-dimensionally reconstructed and embedded into the same generic cornea-scleral shell described in chapter 3. IOP of 25 mmHg was applied to the inner part of the cornea-scleral shell and ICP of 15 mmHg was applied in pia arachnoid complex. For each simulation strain values in LC were recorded. The %C given by Eq. 27 was calculated to analyze the contributions of each principal component to the biomechanical output.

6.2.4 Quantitative shape analysis

Optic Nerve Head Surface Depth

Measuring the *optic nerve head surface depth* (ONHSD) requires the existence of a reference line [99]. Bruch's membrane opening (BMO) can be a good candidate for such a reference line and two BMO points were used in the definition of the reference line used herein. ONHSD refers to the perpendicular distances from the reference plane to the surface of the ILM; see Fig. 43. ONHSD was calculated

with a customized script written in MATLAB (R2019a, The MathWorks, Inc., Natick, MA) [142]. The ONHSD was calculated as in 28:

$$ONHSD = \frac{\|\overrightarrow{BA} \times \overrightarrow{BC}\|}{\|\overrightarrow{BA}\|}, \quad (28)$$

where $\|\overrightarrow{BA} \times \overrightarrow{BC}\|$ is the magnitude of the cross product of the vectors. Figure 44 shows that the area of the parallelogram is the product of the height and its base. Which means the height is equal to equation 28.

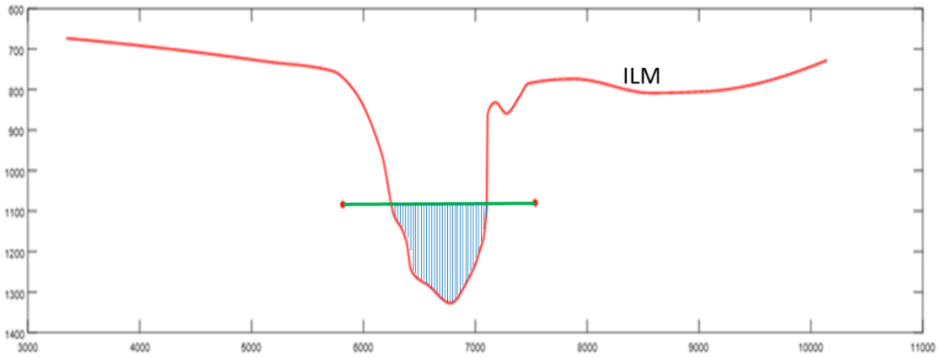

Figure 43. The reference line (green) created by joining two Bruch's membrane opening points (A and B red points). Blue lines are perpendicular lines to the reference line and represent the distance to the internal limiting membrane (ILM) layer surface.

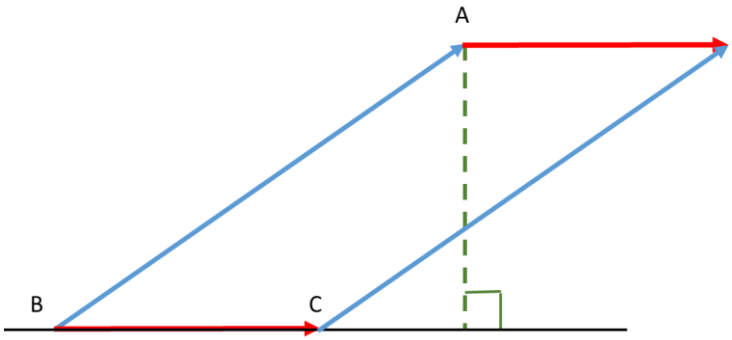

Figure 44. Scheme of the vectors showing how ONHSD (green) was calculated.

Anterior & Posterior Lamina Cribrosa Surfaces

Anterior and posterior lamina cribrosa surface areas were estimated: The processed points were used to generate the alpha shape – a bounding area that envelops the 3D data points. Creating alpha shapes allows estimating the area corresponding to the given point-set. An example alpha shape of the anterior lamina cribrosa surface is shown in Fig. 45.

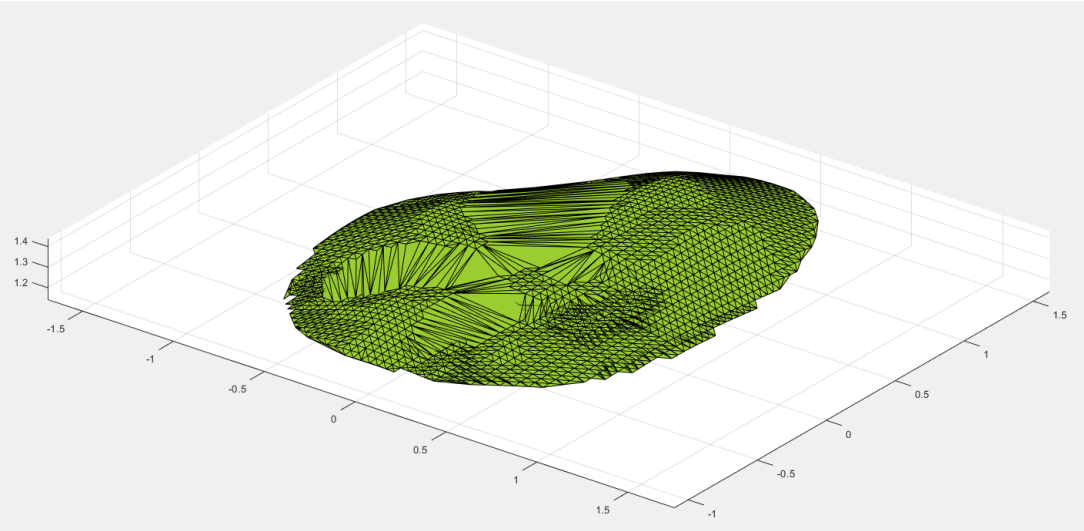

Figure 45. Example alpha shape of anterior lamina cribrosa surface.

Retinal Pigment Epithelium slope

RPE slope was used then to calculate the RPE angle with the x-axis.

Shape index, Gaussian curvature, Mean curvature, Curvedness.

Principal curvatures are eigenvalues of shape operator at the point of a surface and can be calculated as two roots of equation 29:

$$(EG - F^2)k_n^2 - (EN + GL - 2FM)k_n + (LN - M^2) = 0 \qquad (29)$$

Where E, F, G are coefficients of first and L, M, N the coefficients of the second fundamental form and can be calculated as follows:

$$E = \frac{ds}{du} \times \frac{ds}{du}$$

$$F = \frac{ds}{dv} \times \frac{ds}{dv}$$

$$G = \frac{ds}{dv} \times \frac{ds}{dv}$$

$$L = n \times \frac{ds^2}{du^2}$$

$$M = n \times \frac{ds^2}{dudv}$$

$$N = n \times \frac{ds^2}{dv^2}$$

s is surface, n is normal at the point, $\frac{ds}{du}$ the first partial derivative with respect to the first direction, $\frac{ds}{dv}$ the first partial derivative with respect to the other direction and $\frac{ds^2}{du^2}$, $\frac{ds^2}{dv^2}$, $\frac{ds^2}{dudv}$ the second-order partial derivatives of the surface.

Shape index and curvedness can be used to quantify lamina cribrosa shape morphology (alternatively, Gaussian and Mean curvature could be also used). Shape index was introduced by Koendrink and Doorn [151] and is a number in the range (-1,+1) where +1 indicates a locally spherical cap, -1 a locally spherical cup and 0 a locally symmetric saddle shape. Shape index is defined as the following:

$$s = \frac{2}{\pi} arctan \frac{k_2 + k_1}{k_2 - k_1} \quad (k_1 \geq k_2) \qquad (30)$$

where k_1 and k_2 are principal curvatures calculated as the two roots of Eq. 29. Curvedness is a positive number that measures the intensity/amount of curvature and was defined as follows [151]:

$$c = \sqrt{\frac{k_1^2 + k_2^2}{2}} \quad (31)$$

Alternatively, Gaussian and Mean curvature can be used to study the surface shape. Specifically, Gaussian curvature *(G)* is defined as:

$$G = k_1 k_2 \quad (32)$$

where k_1 and k_2 are maximum and minimum principal curvatures and Mean curvature *(M)* is the average of the two principal curvatures:

$$M = \frac{1}{2}(k_1 + k_2) \quad (33)$$

6.3 Results

The measures of generalization and compactness were used to evaluate the SSM. Figure 46 shows the plot of compactness; the first principal component counted for almost 40% of the optic nerve head shape variation. Seven shape modes captured over 80% of shape variation. Eleven principal components were required to capture over 90% of the shape variation. For the measure of generalization, l^2 norm in R^{3294} was 5.68 mm with one principal component and decreased to 4 mm with 10 principal components. The l^2 norm decreased to 3.4 mm with 22 principal components; see Fig 47. Average distances between ONH reconstructed from SSM and the actual ONH from images were also calculated; see Fig. 48.

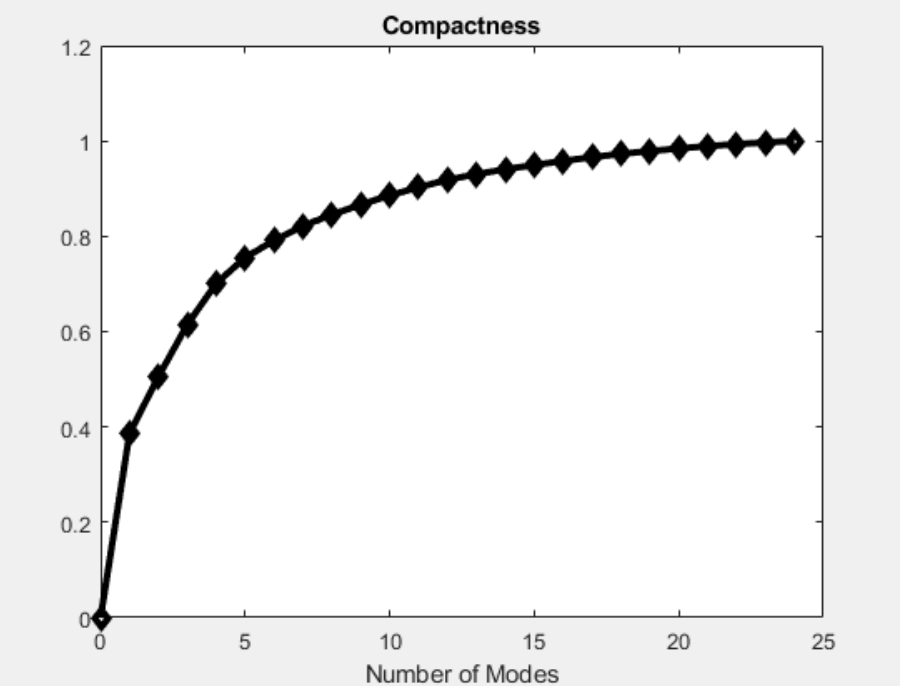

Figure 46. A plot of the statistical shape model's compactness.

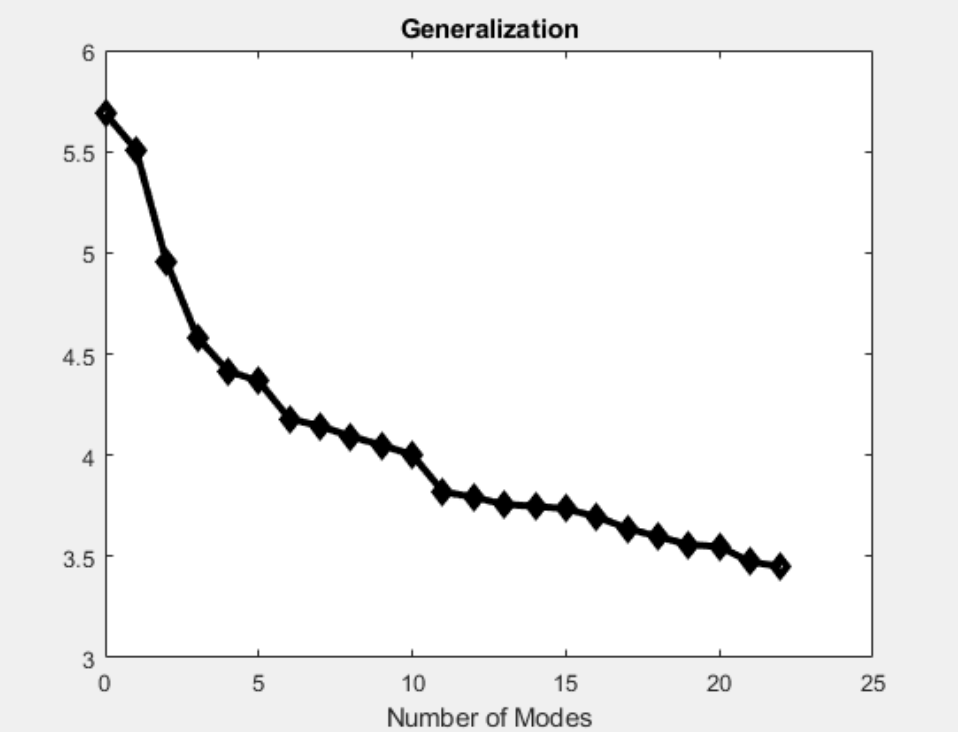

Figure 47. A plot of the generalization of the SSM.

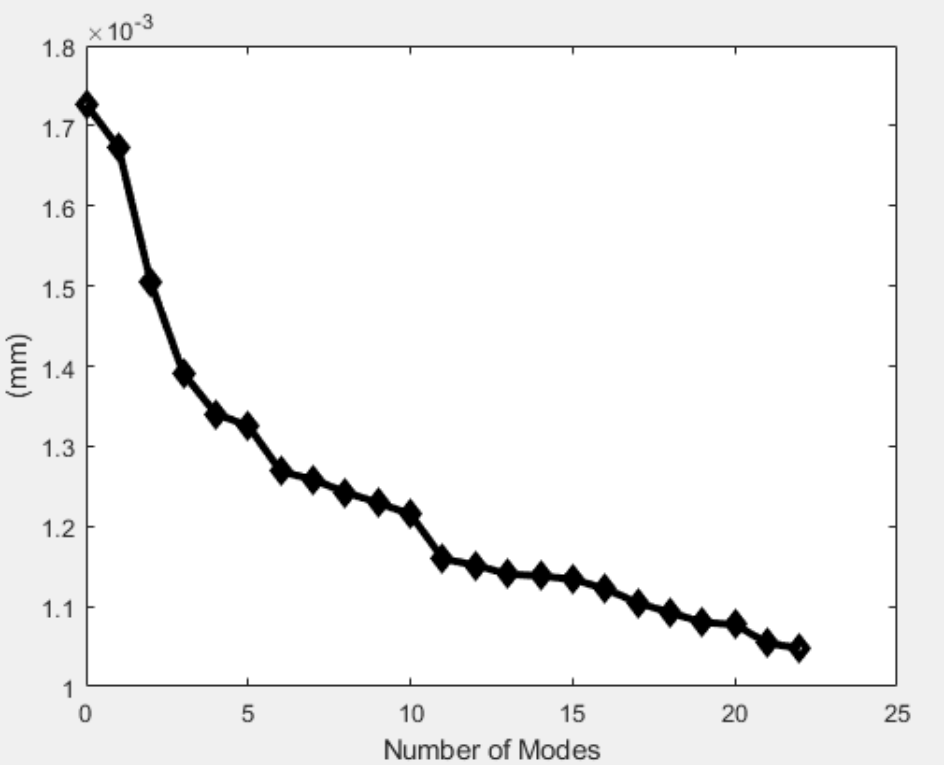

Figure 47. The average distance between points reconstructed from SSM and the actual ONH from image

6.3.1 Shape analysis

The first four shape principal components, with values of $\boldsymbol{b}$ ranging from $-3\sqrt{\lambda_i}$ to $+3\sqrt{\lambda_i}$ applied to the average optic nerve head shape using Eq. 22, are depicted in Fig. 48. The blue points correspond to the mean shape, whereas red and yellow point-sets mark the variation. The 1st PC appears to control the optic cup shape with the effect of lamina cribrosa curvature, Bruch's membrane opening (BMO) radius and angle of the RPE. The 2nd PC seems to affect ILM optic cup depth without scaling and without much effect to its curvature when it starts to bend to form the optic cup. Lamina cribrosa and BMO shrink and move in the nasal and

temporal axis. PC 3 affects largely a movement of the ILM in nasal and temporal axis with effect on its symmetry with large effect its bending region.

Principal component 1

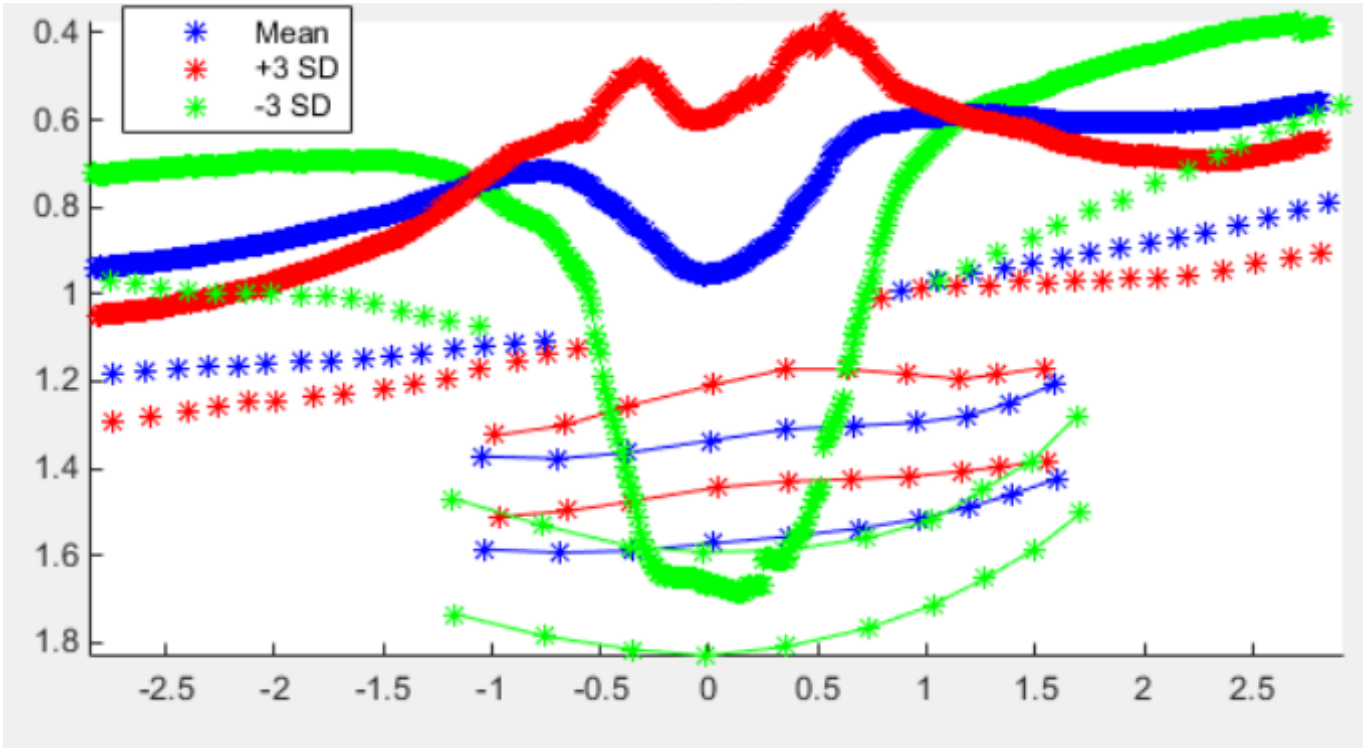

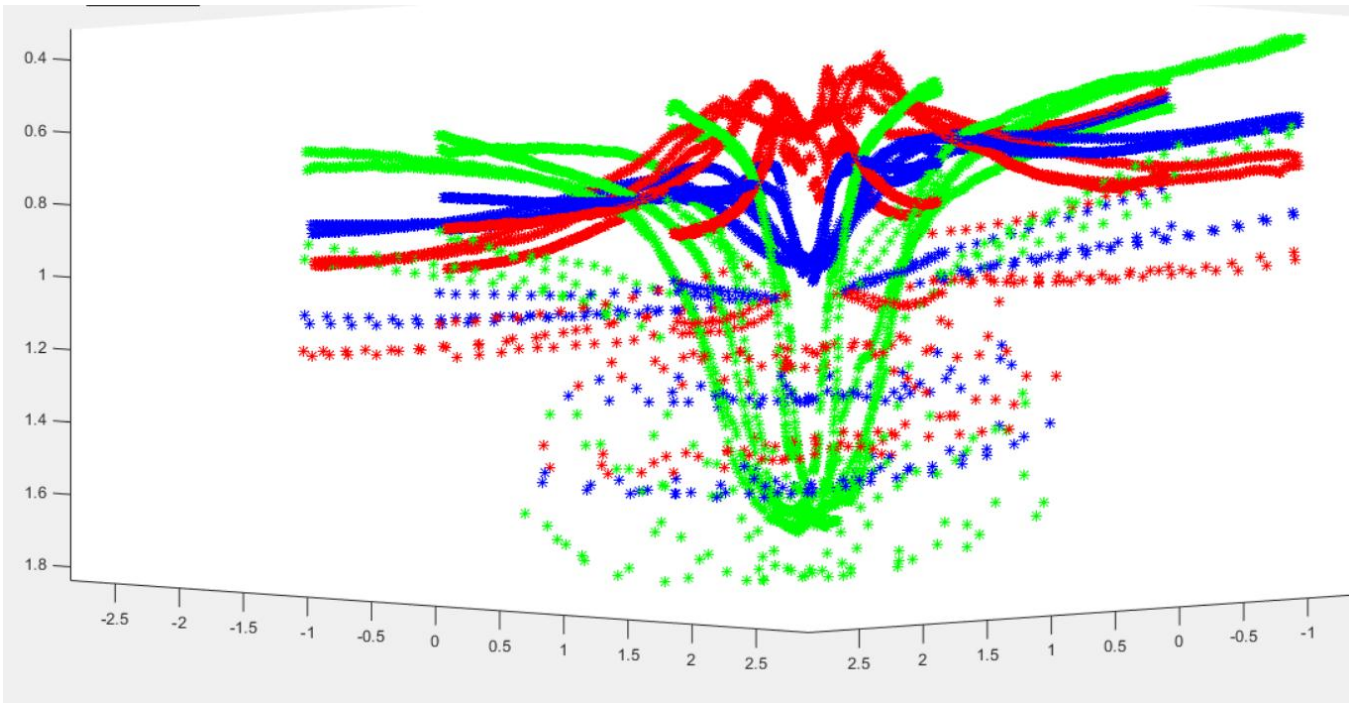

Principal component 2

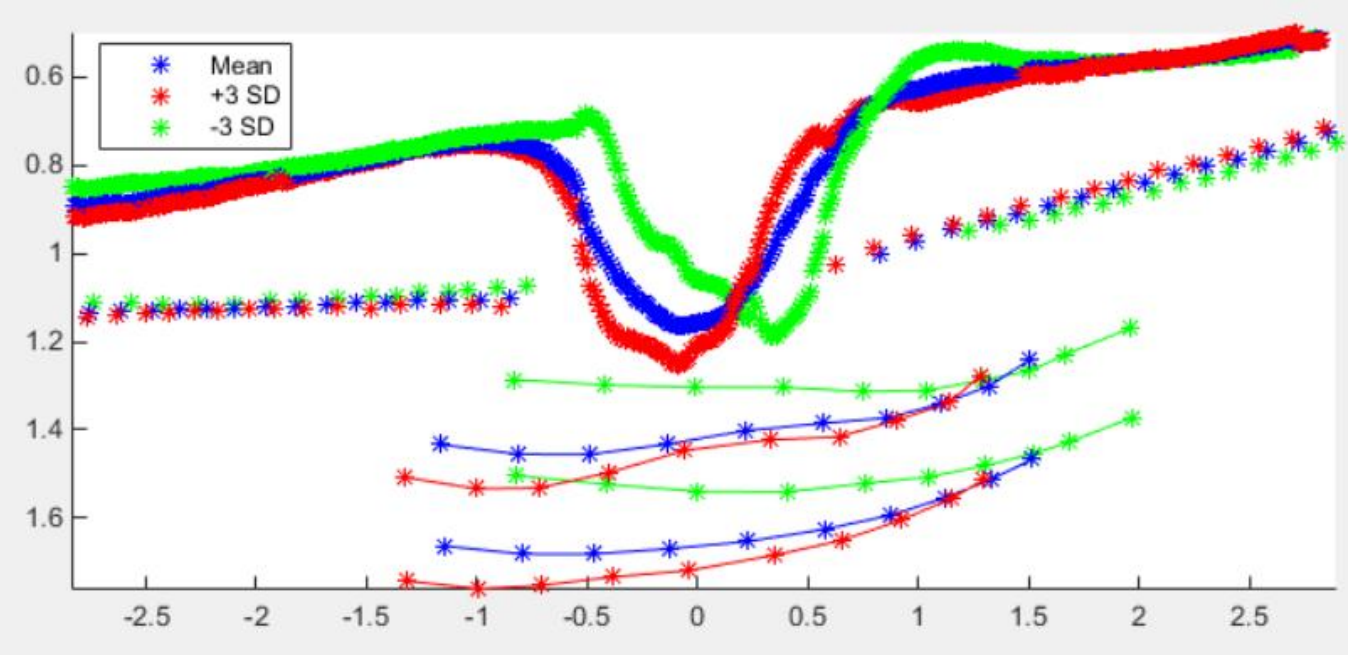

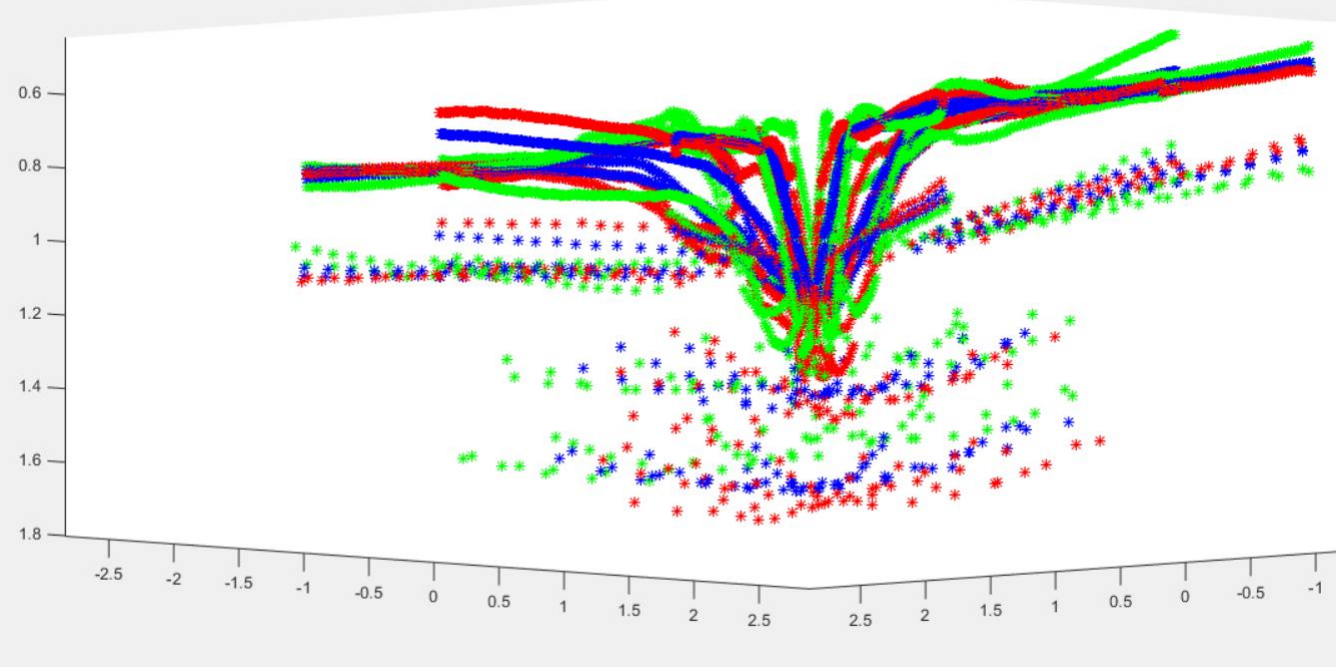

Principal component 3

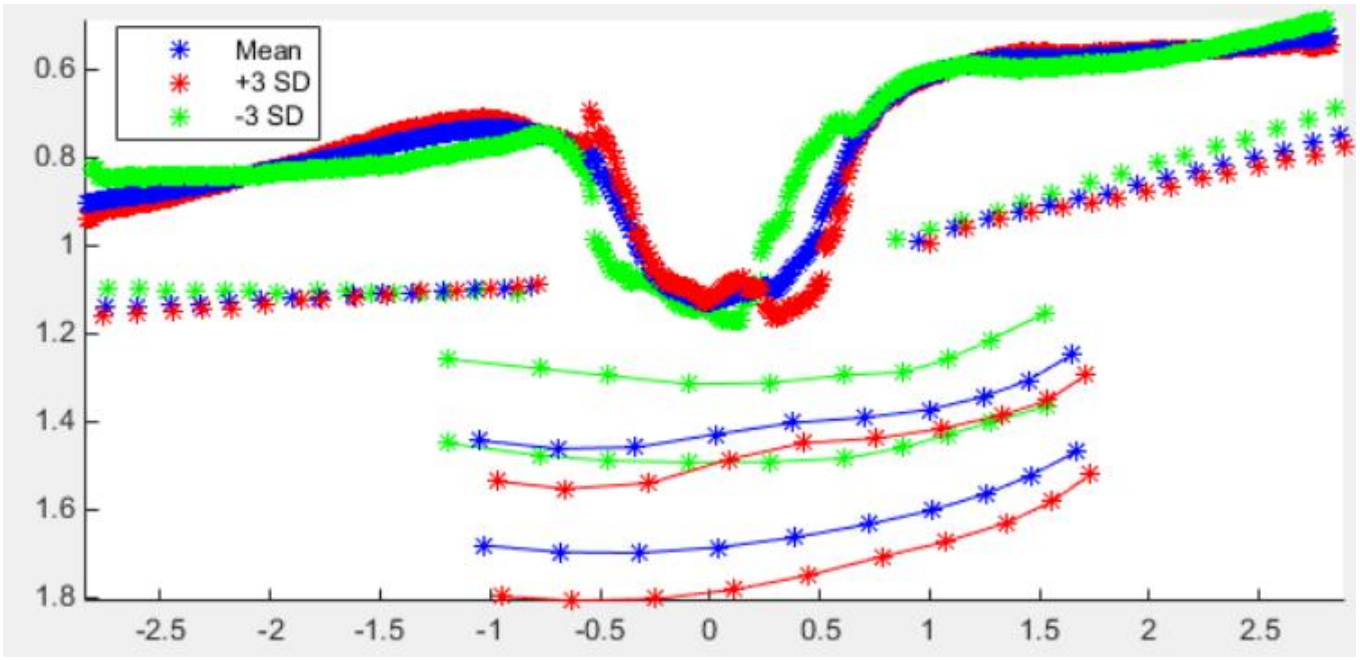

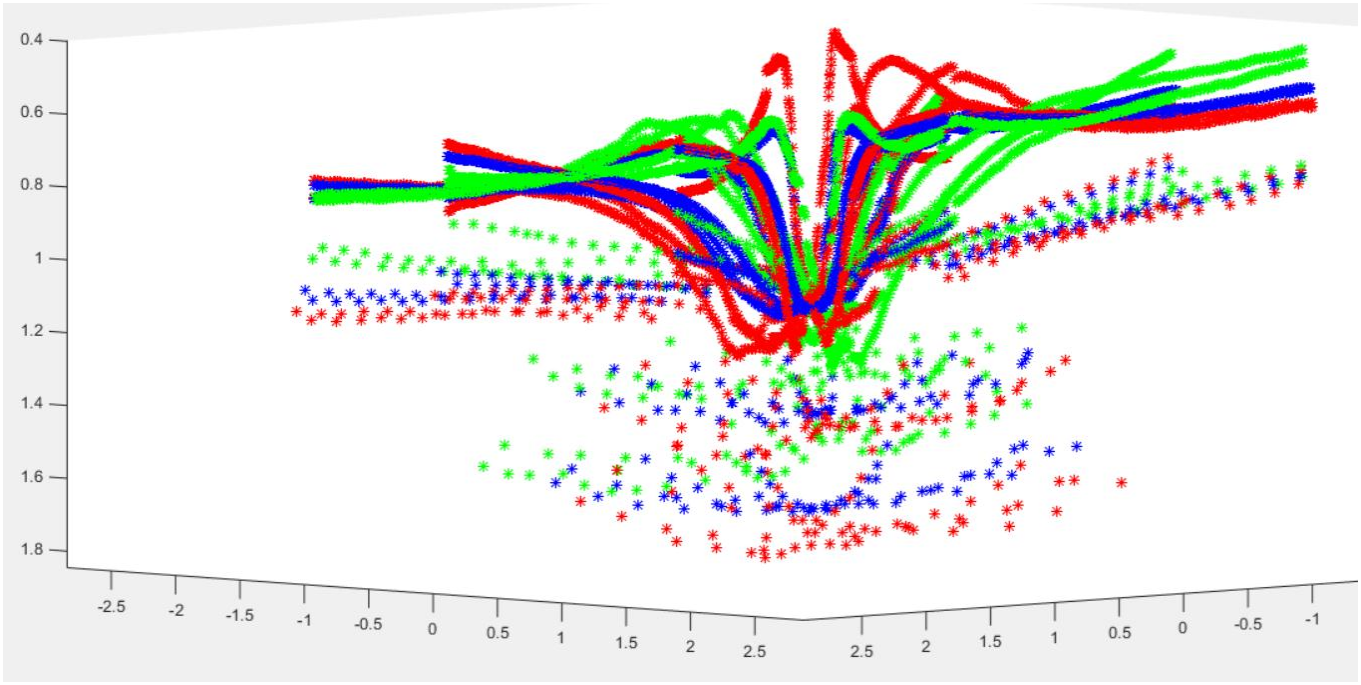

Principal component 4

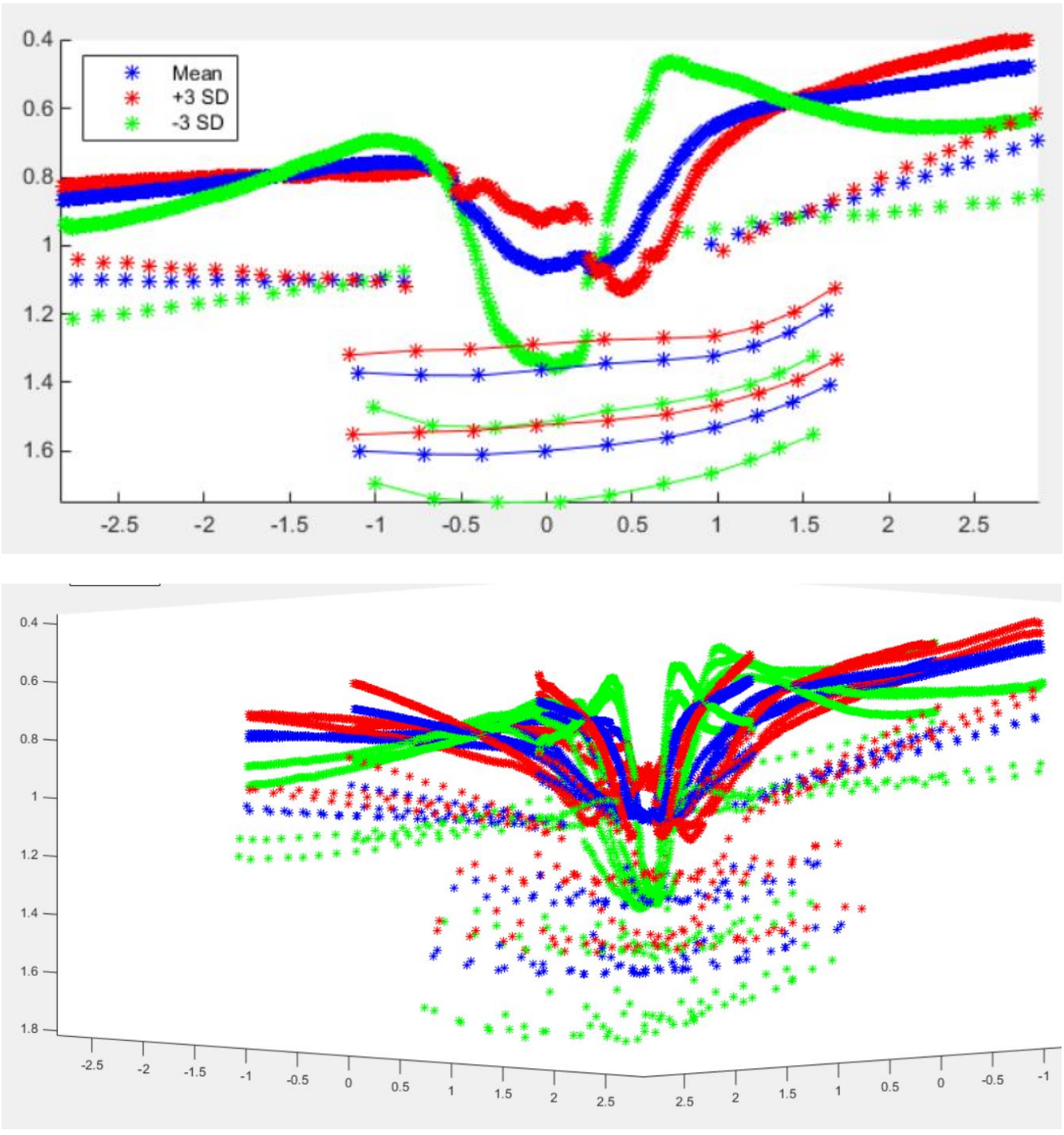

Figure 48. The first four principal components applied to the mean shape with a variation of ±3 SD in three-dimensional view. Data from one cross section represented in two dimensions. Blue characterizes mean, red represents +3 standard deviation and green shows -3 standard deviation.

This mode also affects the width of the LC shape, especially in the bending region. PC 4 appears to affect the height of the optic cup affecting its shape and the distance between ILM and LC in the Z-axis in the posterior and anterior direction. The shape of ILM is steep, flat and saddle-like. RPE curvature angle was also affected highly with this mode.

Principal components of the virtual specimens were three-dimensionally reconstructed to create surfaces with the method described in §5.2.2. After surfaces were created, the anatomical measurements were quantitatively analyzed. Table 12 provides the results of the quantitative analysis regarding the contribution of each principal component. The results show that PC1 contributed mostly to ONHSD, RPE angle, LC shape index and LC mean curvature. This confirmed suggestions from the visual assessment that PC1 is mostly scaling for optic cup shape with the effect of lamina cribrosa curvature, angle of the RPE and Bruch's membrane opening (BMO) radius. PC1 had also contributed mostly to Mean and Gaussian curvature being second after PC7. PC2 contributed primarily to ALCSD, mean BMO distance, PLCSD, ALCSD area slightly less than PC 7. PC3 contributed mostly to ONHSD and curvedness of LC slightly less than PC7. PC 4 was the biggest contributor to Mean BMO distance. The largest contributions to lamina cribrosa norms, Mean, Gaussian curvatures, and the area made by principal components higher than the five shown in table 12 – PC 6, 7, and 10 had the maximum contributions to the lamina cribrosa measures.

Table 13. Percent contribution (Eq. 18) for the first five principal components (PC) for anatomical measurements of ILM, RPE and lamina cribrosa. Max PC is the principal component with the highest percentage contribution. Values are shown with darkest at high values and white at lower values. Overall, calculations were made for eleven principal components since it corresponds to 90% compactness.

Measurement	Max PC	PC1	PC2	PC3	PC4	PC5
Mean ONHSD	1	28.71%	12.47%	11.15%	12.55%	4.83%
Mean BMO distance	4	0.64%	25.84%	1.27%	26.42%	2.71%
ALCSD	2	3.75%	19.45%	1.22%	18.46%	4.88%
PLCSD	7	1.14%	19.35%	4.30%	18.07%	5.80%
ALCS area	7	12.66%	14.59%	12.39%	7.85%	3.99%
PLCS area	7	0.95%	9.55%	12.34%	1.14%	2.35%
RPE angle	1	36.13%	18.42%	6.22%	5.87%	5.51%
ALCS and PLCS distance (norm) in X	7	7.71%	18.39%	4.34%	3.71%	0.31%
ALCS and PLCS distance (norm) in Y	6	3.83%	4.55%	14.51%	4.31%	5.03%
ALCS and PLCS distance (norm) in Z	10	0.69%	7.30%	15.84%	8.68%	4.82%
Shape index of LC	1	27.83%	4.11%	1.16%	6.56%	1.02%
Mean curvature of LC	1	21.18%	3.95%	10.24%	6.25%	4.36%
Gaussian curvature of LC	7	23.73%	3.63%	11.28%	5.51%	3.91%
Curvedness of LC	7	11.26%	1.26%	20.06%	5.38%	3.29%

The biomechanical analysis was once again performed with FE simulations. Twenty-two models based on ±3 SD of the shape components for each of the eleven principal components were generated. Results were taken for 95th percentile strains because they are a measure of the high strain that may cause tissue damage while avoiding numerical errors associated with mesh or badly shaped elements. Figure 49 shows results for the first, third principal and shear strain values. Results show that all of the five principal components have a different effect on ONH biomechanics. Table 13 presents the percent contribution results of FE models based on the first five principal components. Biomechanical analysis results show that PC 1 contributed the most for maximum and minimum principal strains. PC 6 contributed the most to shear strain.

Table 14. Percent contribution of eleven principal components for 95th percentile maximum principal, minimum principal and shear strains.

PC number	95th percentile maximum principal strain	95th percentile minimum principal strain	95th percentile shear strain
1	28.16	23.67	20.34
2	16.02	10.09	7.77
3	9.79	0.44	2.31
4	6.38	2.11	6.57
5	1.29	13.54	14.61
6	11.51	13.06	24.49
7	7.27	4.99	3.49
8	1.71	5.38	5.53
9	2.45	3.69	3.49
10	13.08	17.54	7.03
11	2.31	5.48	4.37

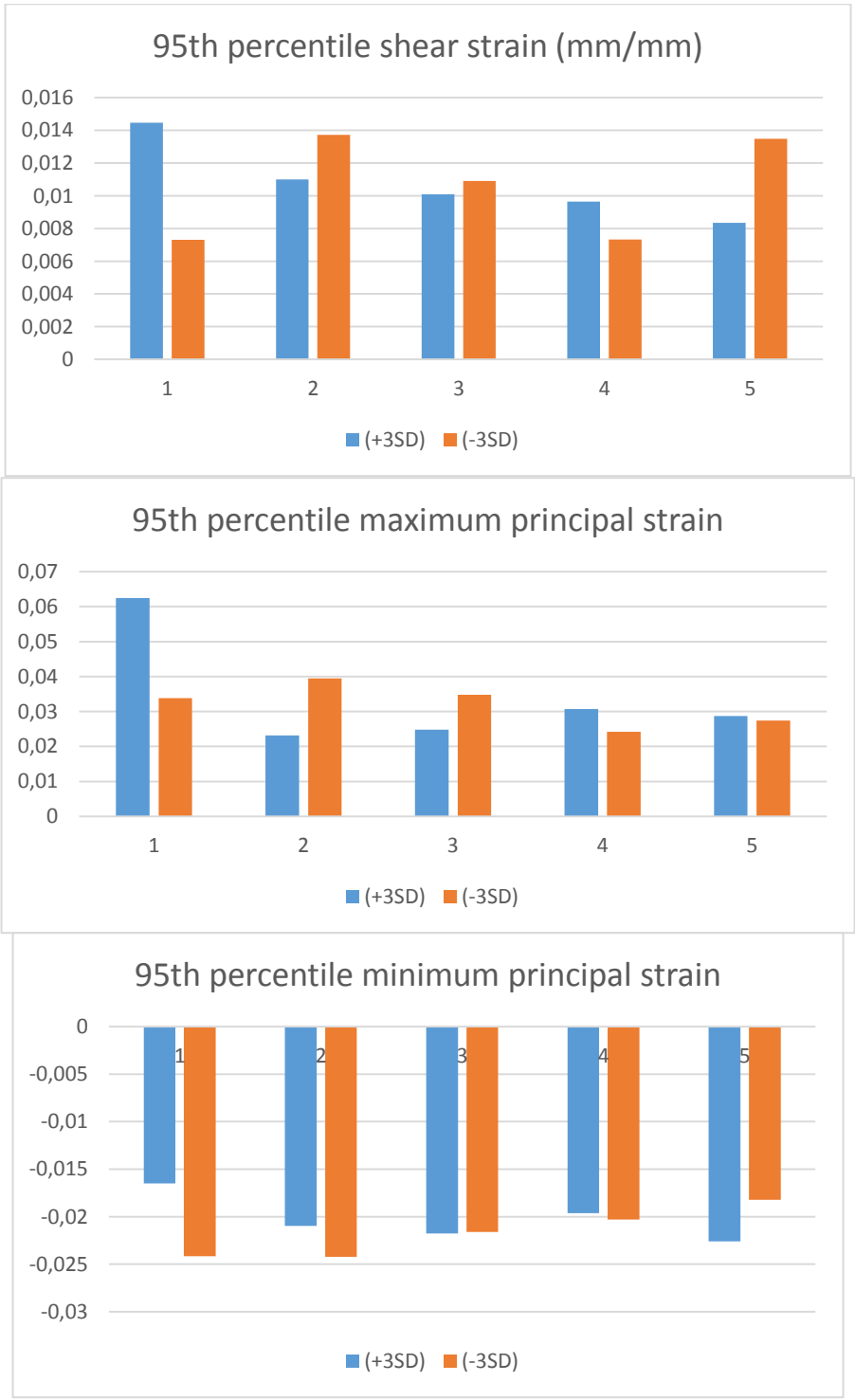

Figure 49. Biomechanical shape examination results based on finite element simulations based on the first five principal components.

6.4 Discussion

In this chapter, we introduced the use of a statistical shape modeling approach for parametrizing patient-specific models of the ONH region. Dura mater was not included since our focus was ONH shape variation analysis. The statistical shape model is based on the point-sets extracted from the segmentation of RPE, ILM and LC layers from OCT images of patients. An equal number of points of the segmented landmarks is a prerequisite for SSM generation. Lamina cribrosa was segmented manually, after an image enhancement algorithm was applied, which made visible the posterior part.

Our goal was to create an SSM of optic nerve head from points of optical coherence tomography images and generate a fully parametrized ocular finite element model to study the influence of intraocular pressure on the ONH biomechanical environment. We successfully created 22 FE ocular models from extreme values (±3 SD) of 11 principal components from a training set of images. We have demonstrated how FE and SSM can be combined to allow future population-based modeling. The statistical shape model was also assessed by examining its generalization and compactness. The first eleven principal components of optic nerve head covered over 90% of the variation where a similar area of variation was also found in other models [150, 152]. Sigal et al. [153] proposed a method to parametrize subject-specific finite element ocular model geometries, however, they used a morphing technique.

Initial principal components represent large-scale variation and the higher modes represent small variations. Therefore, SSM can be described with a small number of shape parameters and this is its one major advantage. For optic nerve head shape, the summative contribution of 14^{th} to 25^{th} principal components is around 5 percent. When shape models are used to study variation in IOP/ICP as a function of shape variation, one should be careful. Small variations in the ONH shape do not always lead to a small influence on IOP on the ONH biomechanics. This is why higher-order modes may be needed to achieve higher accuracy in the biomechanical analysis.

We analyzed ONH shape models biomechanically by varying each of the principal components. Each of the principal components generally contributed similarly except the first one. However, PC 6, which only contributed 3% of the total influence, did register the greatest influence on the shear strain. This shows that principal components with a low percentage of total variation can have a large effect on ONH biomechanics. Another issue that needs to be also addressed is the fact that higher principal components can be affected by noise during segmentation and imaging. This should be taken into account in future models when we consider the number of principal components to keep in the statistical model.

The SSM analyses and anatomical measures described above are given as an example of what can be done with future high-quality models of optic nerve head. Future SSM of ONH should include pathologies and large data size to be able to make remarkable conclusions. One can also include all other layers, for example, choroid, since choroid swelling had a high effect on ONH biomechanics [154]. This

chapter aimed to give an outlook of the SSM applied to ONH. Whereas future models should also include separate SSM for glaucoma and non-glaucoma subjects to be able to have a considerable conclusion.

Special high care should take place when modeling optic nerve head shape variation without peripapillary sclera for biomechanical analysis. Peripapillary sclera will also vary and it has a high influence on ONH biomechanical environment. In our models we used generic scleral shell, however, peripapillary sclera (sclera part near LC) shape also varied according to the reconstructed ONH geometry. Therefore, future models should also include peripapillary sclera.

Chapter 7. Dissertation synopsis

This Ph.D. dissertation proposes approaches to develop generic and patient-specific ocular models from OCT images to characterize the effect of intraocular/intracranial pressures on the optic nerve head biomechanics. The use of the generic model targeted the facilitation of parametric analysis and identification of the main contributing factors in relevant biomechanics. The patient-specific models were then compared with the generic model to qualitatively and quantitatively assess the deviations from the generic model and their effects on the analysis results. Finally, an attempt to generate and evaluate a statistical shape model based on patient-specific scans was also presented.

With regards to the aims set in §1.5 the following can be briefly stated:

- Aim 1: we performed parametric analysis with a generic ocular model and studied the effect of ICP on hypertensive subjects. The effect of cornea characteristics was also considered since it was hypothesized that cornea plays a role in hypertensive subjects. Simulation results indicate a significant role of ICP in post-laminar neural tissue and a possible role of the cornea in ocular hypertension. Future studies should consider the effect of blood pulse on ONH biomechanics including choroid.
- Aim 2: we developed an automated method for ONH segmentation and analysis. After developing the automated ONH segmentation tool, we found that segmentation with the hybrid algorithm had comparable

results with that of manual human delineation, but with significant time reduction; the hybrid algorithm allowed to segment RPE and ILM layers with reduced processing time for further development of patient-specific models. Future studies should consider segmenting lamina cribrosa and all other layers automatically.

- Aim 3: we utilized the segmentation algorithm developed in Aim 2 to delineate RPE and ILM layers and reconstruct patient-specific ONH models. Reconstructed ONHs were embedded into a generic cornea scleral shell utilized in Aim 1. We demonstrate significant interactions between IOP and ICP comparing generic and patient-specific models. Calculations indicate the importance of patient-specific modeling when considering both IOP and ICP for future studies. We also demonstrated the importance of viscoelastic properties. As expected, calculations with viscoelastic properties taken from experiments revealed measurable differences with calculation results taken with linear elastic properties. In the future, non-linear viscoelastic properties should also be considered.
- Aim 4: we developed a statistical shape model on the basis of the patient-specific scans using principal component analysis. Model instances were reconstructed and embedded into a generic cornea-scleral shell using the methodology developed in Aim 3 for further biomechanical assessment. In this way, we have demonstrated an alternative approach for parametric analysis of patient-specific models.

In the future, SSM for glaucoma and non-glaucoma subjects should be developed.

7.1 Limitations and future work

While patient-specific/generic FE models and SSM have the potential to significantly improve our understanding of glaucoma, there are technical limitations that must be considered of our calculations as well as future FE modeling.

The main limitation of this study is related to the inability of OCT to capture whole ONH region. Specifically, OCT could not fully capture peripapillary sclera, which is known to play an important role in the ONH biomechanical environment [118]. Although OCT examinations were carried with enhanced depth imaging (making posterior part of ONH more visible) and compensation algorithm [143] was applied to enhance LC visibility, the posterior layer of LC was 80% visible on average, which resulted in subjective delineations. Other important parts such as dura mater and pia mater were also non-visible. Despite that ONH geometry seems to have modest effects when compared to tissue material properties, our models still demonstrate significant changes in the LC due to ICP and IOP. While our calculations demonstrate a significant effect of IOP and ICP, it is important to remember that these effects come from acute changes only. Future models should also include patient-specific peripapillary sclera and dura mater geometry.

The second limitation is that the models were calculated with linear elastic properties. While it is well known that living tissues are viscoelastic. And it was also demonstrated in Aim 3 that viscoelastic properties have a measurable effect.

The third limitation: for simplicity, we modeled IOP/ICP as static, while it is known that IOP and ICP are pulsatile [133]. It is also known that ICP is out of phase with IOP and may sync with IOP and these fluctuations may cause glaucoma [21]. Future models should consider the pulsatile effects of IOP and ICP on ONH.

The fourth limitation: it is known that there are variations in sclera thickness and elastic stiffness [155]. Our models did not account for these variations. Such variations might affect ONH when considering pulsatile IOP/ICP. Future models should consider that effect of scleral thickness stiffness variations.

Fifth limitation: in SSM we did not consider all ONH layers; only ILM, RPE, and LC were considered. Future SSM models should also consider other ONH layers such as choroid, optical plexiform layer, etc.

Sixth limitation: SSM was constructed on the basis of 26 patients-scans. In future SSM, more OCT images should be used for training the model.

Seventh limitation: all tissues were assumed isotropic, however, several studies have shown that sclera is anisotropic especially in the peripapillary region [54, 55]. It was found that the tangential arrangement of fibers afforded better mechanical support to the tissues within the scleral canal as compared to a simple circumferential ring of fibers [55]. Scleral anisotropy was also found to change significantly as a function of depth [156]. Future modelling should consider

circumferential and tangential fiber orientation in peripapillary sclera, which is one of the critical factors in determining the mechanical response of the ONH.

7.2 Conclusion

A summary of our results and conclusion is briefly presented below:

We have performed parametric analysis with the generic model using Taguchi's method to screen important factors affecting ONH biomechanics.

ICP seems to counteract IOP effects in the lamina cribrosa region. We have also identified that it is important to consider both IOP and ICP when assessing ONH biomechanical environment as they both affect deformations in LC.

The effect of geometric and material properties of the cornea were also characterized. Cornea seems to have an effect on the laminar cribrosa region, although a rather modest one. It was also found that thinner cornea seems to be a potent risk factor for glaucoma.

An automatic algorithm was developed to segment retina layers from OCT images. A three-dimensional reconstruction algorithm was also developed and used to build patient-specific ocular models. Patient-specific models were employed to understand the effect of patient-specific ONH geometry on its biomechanical environment under induced IOP and ICP. Geometry seems to play a role in ONH biomechanics, however, from the relative percentage volume, it is not clear which geometric factors are the important ones. To understand this, we have developed a

fully parametrized patient-specific model and discussed principal components from the developed statistical shape model. These were assessed qualitatively, quantitatively, and biomechanically. The assessment of ONH geometry with SSM holds great promise for both improving our understanding of glaucoma pathogenesis and diagnosis.

References:

1. ROBINSON KA (1997) Dictionary of Eye Terminology. Br J Ophthalmol. https://doi.org/10.1136/bjo.81.11.1021c

2. Midgett DE, Pease ME, Jefferys JL, et al (2017) The pressure-induced deformation response of the human lamina cribrosa: Analysis of regional variations. Acta Biomater. https://doi.org/10.1016/j.actbio.2016.12.054

3. Quigley HA (1999) Neuronal death in glaucoma. Prog Retin Eye Res. https://doi.org/10.1016/S1350-9462(98)00014-7

4. Minckler DS, Bunt AH, Johanson GW (1977) Orthograde and retrograde axoplasmic transport during acute ocular hypertension in the monkey. INVESTOPHTHALVISUAL SCI

5. Foster PJ, Buhrmann R, Quigley HA, Johnson GJ (2002) The definition and classification of glaucoma in prevalence surveys. Br. J. Ophthalmol.

6. Tham YC, Li X, Wong TY, et al (2014) Global prevalence of glaucoma and projections of glaucoma burden through 2040: A systematic review and meta-analysis. Ophthalmology. https://doi.org/10.1016/j.ophtha.2014.05.013

7. Friedman DS, Jampel HD, Muñoz B, West SK (2006) The prevalence of open-angle glaucoma among blacks and whites 73 years and older: The Salisbury Eye Evaluation glaucoma study. Arch Ophthalmol. https://doi.org/10.1001/archopht.124.11.1625

8. Rotchford AP, Johnson GJ (2002) Glaucoma in Zulus: A population-based cross-sectional survey in a rural district in South Africa. Arch Ophthalmol

9. Leske MC, Connell AMS, Schachat AP (1994) The Barbados Eye Study: Prevalence of Open Angle Glaucoma. Arch Ophthalmol. https://doi.org/10.1001/archopht.1994.01090180121046

10. Boland M V., Zhang L, Broman AT, et al (2008) Comparison of Optic Nerve Head Topography and Visual Field in Eyes with Open-angle and Angle-closure Glaucoma. Ophthalmology. https://doi.org/10.1016/j.ophtha.2007.03.086

11. Hollows FC, Graham PA (1966) Intra-ocular pressure, glaucoma, and glaucoma suspects in a defined population. Br J Ophthalmol. https://doi.org/10.1136/bjo.50.10.570

12. Mackenzie W (1854) A Practical Treatise on the Diseases of the Eye. Longman

13. Girard MJA, Beotra MR, Chin KS, et al (2016) In Vivo 3-Dimensional Strain Mapping of the Optic Nerve Head Following Intraocular Pressure Lowering by Trabeculectomy. Ophthalmology. https://doi.org/10.1016/j.ophtha.2016.02.008

14. Leske MC (2007) Open-angle glaucoma - An epidemiologic overview. In: Ophthalmic Epidemiology

15. Lam D, Lee J, Jonas J, et al (2016) Glaucoma: Today and tomorrow. Asia-Pacific J. Ophthalmol.

16. Sigal IA, Bilonick RA, Kagemann L, et al (2012) The optic nerve head as a robust

biomechanical system. Investig Ophthalmol Vis Sci 53:2658–2667. https://doi.org/10.1167/iovs.11-9303

17. Asrani S, Zeimer R, Wilensky J, et al (2000) Large diurnal fluctuations in intraocular pressure are an independent risk factor in patients with glaucoma. J Glaucoma. https://doi.org/10.1097/00061198-200004000-00002

18. Burgoyne CF, Crawford Downs J, Bellezza AJ, et al (2005) The optic nerve head as a biomechanical structure: A new paradigm for understanding the role of IOP-related stress and strain in the pathophysiology of glaucomatous optic nerve head damage. Prog. Retin. Eye Res.

19. Feola AJ, Myers JG, Raykin J, et al (2016) Finite Element Modeling of Factors Influencing Optic Nerve Head Deformation Due to Intracranial Pressure. Investig Opthalmology Vis Sci. https://doi.org/10.1167/iovs.15-17573

20. Berdahl JP, Fautsch MP, Stinnett SS, Allingham R (2008) Intracranial pressure in primary open angle glaucoma, normal tension glaucoma, and ocular hypertension: A case-control study. Investig Ophthalmol Vis Sci. https://doi.org/10.1167/iovs.08-2228

21. Morgan WH, Yu DY, Cooper RL, et al (1995) The influence of cerebrospinal fluid pressure on the lamina cribrosa tissue pressure gradient. Investig Ophthalmol Vis Sci

22. Killer HE, Laeng HR, Flammer J, Groscurth P (2003) Architecture of arachnoid trabeculae, pillars, and septa in the subarachnoid space of the human optic nerve: Anatomy and clinical considerations. Br J Ophthalmol. https://doi.org/10.1136/bjo.87.6.777

23. Wu SY, Leske MC (1997) Associations with intraocular pressure in the Barbados Eye

Study. Arch Ophthalmol. https://doi.org/10.1001/archopht.1997.01100160742012

24. Morgan WH, Lind CRP, Kain S, et al (2012) Retinal vein pulsation is in phase with intracranial pressure and not intraocular pressure. Investig Ophthalmol Vis Sci. https://doi.org/10.1167/iovs.12-9837

25. Jain MR, Marmion VJ (1976) Rapid pneumatic and Mackay-Marg applanation tonometry to evaluate the postural effect on intraocular pressure. Br J Ophthalmol. https://doi.org/10.1136/bjo.60.10.687

26. Ren R, Zhang X, Wang N, et al (2011) Cerebrospinal fluid pressure in ocular hypertension. Acta Ophthalmol. https://doi.org/10.1111/j.1755-3768.2010.02015.x

27. Huang D, Swanson EA, Lin CP, et al (1991) Optical Coherence Tomography HHS Public Access. Sci Novemb. https://doi.org/10.1002/jcp.24872.The

28. Quigley HA, Addicks EM, Green WR, Maumenee AE (1981) Optic nerve damage in human glaucoma: Ii. The Site of Injury and Susceptibility to Damage. Arch Ophthalmol. https://doi.org/10.1001/archopht.1981.03930010635009

29. Downs JC, Roberts MD, Burgoyne CF (2008) Mechanical Environment of the Optic Nerve Head in Glaucoma. Optom. Vis. Sci.

30. Sigal IA, Flanagan JG, Ethier CR (2005) Factors influencing optic nerve head biomechanics. Investig Ophthalmol Vis Sci. https://doi.org/10.1167/iovs.05-0541

31. Burgoyne CF, Morrison JC (2001) The anatomy and pathophysiology of the optic nerve head in glaucoma. J. Glaucoma

32. Fechtner RD, Weinreb RN (1994) Mechanisms of optic nerve damage in primary open angle glaucoma. Surv. Ophthalmol.

33. Burgoyne CF, Downs JC (2008) Premise and prediction-how optic nerve head biomechanics underlies the susceptibility and clinical behavior of the aged optic nerve head. J. Glaucoma

34. Bellezza AJ, Hart RT, Burgoyne CF (2000) The optic nerve head as a biomechanical structure: Initial finite element modeling. Investig Ophthalmol Vis Sci 41:2991–3000

35. Dandona L, Quigley HA, Brown AE, Enger C (1990) Quantitative Regional Structure of the Normal Human Lamina Cribrosa: A Racial Comparison. Arch Ophthalmol. https://doi.org/10.1001/archopht.1990.01070050091039

36. Quigley HA, Addicks EM (1981) Regional Differences in the Structure of the Lamina Cribrosa and Their Relation to Glaucomatous Optic Nerve Damage. Arch Ophthalmol. https://doi.org/10.1001/archopht.1981.03930010139020

37. Radius RL, Gonzales M (1981) Anatomy of the lamina cribrosa in human eyes. Arch Ophthalmol. https://doi.org/10.1001/archopht.1981.03930021035010

38. Roberts MD, Hart RT, Liang Y, et al (2007) Continuum-level finite element modeling of the optic nerve head using a fabric tensor based description of the lamina cribrosa. In: Proceedings of the ASME Summer Bioengineering Conference 2007, SBC 2007

39. Downs JC, Blidner RA, Bellezza AJ, et al (2002) Peripapillary scleral thickness in perfusion-fixed normal monkey eyes. Investig Ophthalmol Vis Sci

40. Chung CW, Girard MJA, Jan NJ, Sigal IA (2016) Use and misuse of laplace's law in ophthalmology. Investig Ophthalmol Vis Sci. https://doi.org/10.1167/iovs.15-18053

41. K-J. Li J (1986) Comparative cardiac mechanics: Laplace's law. J Theor Biol. https://doi.org/10.1016/S0022-5193(86)80064-9

42. Ethier CR, Johnson M, Ruberti J (2004) Ocular Biomechanics and Biotransport.

Annu Rev Biomed Eng. https://doi.org/10.1146/annurev.bioeng.6.040803.140055

43. Sigal I a, Flanagan JG, Tertinegg I, Ethier CR (2004) Finite element modeling of optic nerve head biomechanics. Invest Ophthalmol Vis Sci. https://doi.org/10.1167/iovs.04-0133

44. Sigal IA, Flanagan JG, Tertinegg I, Ethier CR (2009) Modeling individual-specific human optic nerve head biomechanics. Part I: IOP-induced deformations and influence of geometry. Biomech Model Mechanobiol. https://doi.org/10.1007/s10237-008-0120-7

45. Sigal IA, Flanagan JG, Ethier CR (2005) Factors influencing optic nerve head biomechanics - A finite element analysis. In: Proceedings of the 2005 Summer Bioengineering Conference

46. Girard MJA, Downs JC, Burgoyne CF, Suh JKF (2009) Peripapillary and posterior scleral mechanics - Part I: Development of an anisotropic hyperelastic constitutive model. J Biomech Eng. https://doi.org/10.1115/1.3113682

47. Perez BC, Morris HJ, Hart RT, Liu J (2013) Finite element modeling of the viscoelastic responses of the eye during microvolumetric changes. J Biomed Sci Eng. https://doi.org/10.4236/jbise.2013.612a005

48. Ayyalasomayajula A, Park RI, Simon BR, Vande Geest JP (2016) A porohyperelastic finite element model of the eye: the influence of stiffness and permeability on intraocular pressure and optic nerve head biomechanics. Comput Methods Biomech Biomed Engin. https://doi.org/10.1080/10255842.2015.1052417

49. Sigal IA, Flanagan JG, Tertinegg I, Ethier CR (2007) Predicted extension, compression and shearing of optic nerve head tissues. Exp Eye Res.

https://doi.org/10.1016/j.exer.2007.05.005

50. Sigal IA, Flanagan JG, Tertinegg I, Ethier CR (2009) Modeling individual-specific human optic nerve head biomechanics. Part I: IOP-induced deformations and influence of geometry. Biomech Model Mechanobiol. https://doi.org/10.1007/s10237-008-0120-7

51. Norman RE, Flanagan JG, Rausch SMK, et al (2010) Dimensions of the human sclera: Thickness measurement and regional changes with axial length. Exp Eye Res. https://doi.org/10.1016/j.exer.2009.11.001

52. Coudrillier B, Boote C, Quigley HA, Nguyen TD (2013) Scleral anisotropy and its effects on the mechanical response of the optic nerve head. Biomech Model Mechanobiol. https://doi.org/10.1007/s10237-012-0455-y

53. Campbell IC, Coudrillier B, Mensah J, et al (2015) Automated segmentation of the lamina cribrosa using Frangi's filter: A novel approach for rapid identification of tissue volume fraction and beam orientation in a trabeculated structure in the eye. J R Soc Interface. https://doi.org/10.1098/rsif.2014.1009

54. Zhang L, Albon J, Jones H, et al (2015) Collagen microstructural factors influencing optic nerve head biomechanics. Invest Ophthalmol Vis Sci. https://doi.org/10.1167/iovs.14-15734

55. Voorhees AP, Jan NJ, Hua Y, et al (2018) Peripapillary sclera architecture revisited: A tangential fiber model and its biomechanical implications. Acta Biomater. https://doi.org/10.1016/j.actbio.2018.08.020

56. Quigley H, Broman AT (2006) The number of people with glaucoma worldwide in 2010 and 2020. Br. J. Ophthalmol.

57. Sigal IA, Ethier CR (2009) Biomechanics of the optic nerve head. Exp. Eye Res.

58. Hattar S, Liao HW, Takao M, et al (2002) Melanopsin-containing retinal ganglion cells: Architecture, projections, and intrinsic photosensitivity. Science (80-). https://doi.org/10.1126/science.1069609

59. Yan DB, Coloma FM, Metheetrairut A, et al (1994) Deformation of the lamina cribrosa by elevated intraocular pressure. Br J Ophthalmol. https://doi.org/10.1136/bjo.78.8.643

60. Hernandez MR (2000) The optic nerve head in glaucoma: Role of astrocytes in tissue remodeling. Prog. Retin. Eye Res.

61. Hiraoka M, Inoue K, Ninomiya T, Takada M (2012) Ischaemia in the Zinn-Haller circle and glaucomatous optic neuropathy in macaque monkeys. Br J Ophthalmol. https://doi.org/10.1136/bjophthalmol-2011-300831

62. Kharmyssov C, Abdildin YG, Kostas K V. (2019) Optic nerve head damage relation to intracranial pressure and corneal properties of eye in glaucoma risk assessment. Med Biol Eng Comput. https://doi.org/10.1007/s11517-019-01983-2

63. Johnson CS, Mian SI, Moroi S, et al (2007) Role of corneal elasticity in damping of intraocular pressure. Investig Ophthalmol Vis Sci. https://doi.org/10.1167/iovs.06-0719

64. Herndon LW, Weizer JS, Stinnett SS (2004) Central Corneal Thickness as a Risk Factor for Advanced Glaucoma Damage. Arch. Ophthalmol.

65. Gordon MO, Beiser JA, Brandt JD, et al (2002) The Ocular Hypertension Treatment Study: Baseline factors that predict the onset of primary open-angle glaucoma. Arch Ophthalmol. https://doi.org/10.1001/archopht.120.6.714

66. Leung LKK, Ko MWL, Lam DCC (2012) Effect of age-stiffening tissues and intraocular pressure on optic nerve damages. Mol Cell Biomech

67. Todd B a, Thacker JG (1994) Three-dimensional computer model of the human buttocks, in vivo. J Rehabil Res Dev

68. Power E, Stitzel J, West R, Herring I (2001) A non linear finite element model of the human eye for large deformation loading. Proc. 25th …

69. Hua Y, Tong J, Ghate D, et al (2017) Intracranial Pressure Influences the Behavior of the Optic Nerve Head. J Biomech Eng. https://doi.org/10.1115/1.4035406

70. Weller RO (2005) Microscopic morphology and histology of the human meninges. Morphologie

71. Ren R, Wang N, Li B, et al (2009) Lamina cribrosa and peripapillary sclera histomorphometry in normal and advanced glaucomatous chinese eyes with various axial length. Investig Ophthalmol Vis Sci. https://doi.org/10.1167/iovs.07-1429

72. Allingham RR, Damji K, Freedman S, et al (2011) Shields Textbook of Glaucoma, 6th Edition.

73. Ren R, Wang N, Zhang X, et al (2012) Cerebrospinal fluid pressure correlated with body mass index. Graefe's Arch Clin Exp Ophthalmol. https://doi.org/10.1007/s00417-011-1746-1

74. Shimmyo M, Ross AJ, Moy A, Mostafavi R (2003) Intraocular pressure, Goldmann applanation tension, corneal thickness, and corneal curvature in Caucasians, Asians, Hispanics, and African Americans. Am J Ophthalmol. https://doi.org/10.1016/S0002-9394(03)00424-0

75. Sing NM, Anderson SF, Townsend JC (2000) The normal optic nerve head . Optom

Vis Sci

76. Hamilton KE, Pye DC (2008) Young's modulus in normal corneas and the effect on applanation tonometry. Optom Vis Sci. https://doi.org/10.1097/OPX.0b013e3181783a70

77. G. Taguchi A productivity organization (1986) Introduction to quality engineering: Designing quality into products and processes

78. Ferreira SLC, Bruns RE, Ferreira HS, et al (2007) Box-Behnken design: An alternative for the optimization of analytical methods. Anal. Chim. Acta

79. Box GEP, Hunter JS, Hunter WG (2005) Statistics of Experimenters 2nd Edition. John Wiley sons. https://doi.org/10.1080/00401706.1979.10489788

80. Neto BB (2005) Statistical Design – Chemometrics

81. McEwan W, Belavendram N, Abou-Ali M (1992) Taguchi methods and expert systems in fabrication design. Int J Press Vessel Pip. https://doi.org/10.1016/0308-0161(93)90103-Z

82. Edwards ME, Wang SSS, Good TA (2001) Role of viscoelastic properties of differentiated SH-SY5Y human neuroblastoma cells in cyclic shear stress injury. Biotechnol Prog. https://doi.org/10.1021/bp010040m

83. Grytz R, Meschke G, Jonas JB (2011) The collagen fibril architecture in the lamina cribrosa and peripapillary sclera predicted by a computational remodeling approach. Biomech Model Mechanobiol. https://doi.org/10.1007/s10237-010-0240-8

84. Grytz R, Sigal IA, Ruberti JW, et al (2012) Lamina cribrosa thickening in early glaucoma predicted by a microstructure motivated growth and remodeling approach. Mech Mater. https://doi.org/10.1016/j.mechmat.2011.07.004

85. Ionescu I, Guilkey JE, Berzins M, et al (2006) Simulation of Soft Tissue Failure Using the Material Point Method. J Biomech Eng. https://doi.org/10.1115/1.2372490

86. Caselli RJ, Boeve BF (2007) Textbook of Clinical Neurology

87. Hua Y, Voorhees AP, Sigal IA (2018) Cerebrospinal Fluid Pressure: Revisiting Factors Influencing Optic Nerve Head Biomechanics. Invest Ophthalmol Vis Sci. https://doi.org/10.1167/iovs.17-22488

88. Berdahl JP, Fautsch MP, Stinnett SS, Allingham RR (2008) Intracranial pressure in primary open angle glaucoma, normal tension glaucoma, and ocular hypertension: a case-control study. Invest Ophthalmol Vis Sci. https://doi.org/10.1167/iovs.08-2228

89. Ren R, Jonas JB, Tian G, et al (2010) Cerebrospinal Fluid Pressure in Glaucoma. A Prospective Study. Ophthalmology. https://doi.org/10.1016/j.ophtha.2009.06.058

90. Woo SLY, Kobayashi AS, Schlegel WA, Lawrence C (1972) Nonlinear material properties of intact cornea and sclera. Exp Eye Res. https://doi.org/10.1016/0014-4835(72)90139-X

91. Brandt JD, Beiser JA, Kass MA, Gordon MO (2001) Central corneal thickness in the Ocular Hypertension Treatment Study (OHTS). Ophthalmology. https://doi.org/10.1016/S0161-6420(01)00760-6

92. Thornton IL, Dupps WJ, Roy AS, Krueger RR (2009) Biomechanical effects of intraocular pressure elevation on optic nerve/lamina cribrosa before and after peripapillary scleral collagen cross-linking. Investig Ophthalmol Vis Sci. https://doi.org/10.1167/iovs.08-1960

93. Gordon MO, Beiser JA, Brandt JD, et al (2002) The Ocular Hypertension Treatment Study: Baseline factors that predict the onset of primary open-angle glaucoma. Arch

Ophthalmol. https://doi.org/10.1001/archopht.120.6.714

94. Drance SM (1972) The glaucomatous visual field. Br J Ophthalmol. https://doi.org/10.1136/bjo.56.3.186

95. Edwards ME, Wang SSS, Good TA (2001) Role of viscoelastic properties of differentiated SH-SY5Y human neuroblastoma cells in cyclic shear stress injury. Biotechnol Prog. https://doi.org/10.1021/bp010040m

96. Berdahl JP, Allingham RR (2010) Intracranial pressure and glaucoma. Curr Opin Ophtalmol 21:106–111. https://doi.org/10.1097/WNO.0000000000000295

97. Hou R, Zhang Z, Yang D, et al (2016) Intracranial pressure (ICP) and optic nerve subarachnoid space pressure (ONSP) correlation in the optic nerve chamber: The Beijing Intracranial and Intraocular Pressure (iCOP) study. Brain Res. https://doi.org/10.1016/j.brainres.2016.01.011

98. Johnson M, Kass MA, Moses RA, Grodzki WJ (1978) Increased Corneal Thickness Simulating Elevated Intraocular Pressure. Arch Ophthalmol. https://doi.org/10.1001/archopht.1978.03910050360012

99. Wu Z, Xu G, Weinreb RN, et al (2015) Optic Nerve Head Deformation in Glaucoma. Ophthalmology. https://doi.org/10.1016/j.ophtha.2015.02.035

100. DeBuc DC (2011) A review of algorithms for segmentation of retinal image data using optical coherence tomography. Image Segmentation. https://doi.org/10.5772/628

101. Xiang D, Chen G, Shi F, et al (2019) Automatic retinal layer segmentation of OCT images with central serous retinopathy. IEEE J Biomed Heal Informatics. https://doi.org/10.1109/JBHI.2018.2803063

102. Koozekanani D, Member S, Boyer K, et al (2001) Coherence Tomography Using a

Markov Boundary Model. IEEE Trans Med Imaging. https://doi.org/10.1109/42.952728

103. Baroni M, Fortunato P, La Torre A (2007) Towards quantitative analysis of retinal features in optical coherence tomography. Med Eng Phys. https://doi.org/10.1016/j.medengphy.2006.06.003

104. Hacker M, Abràmoff M, Kardon R, Sonka M (2006) Segmentation of the surfaces of the retinal layer from OCT images. Med Image Comput Comput Assist Interv. https://doi.org/10.1007/11866565_98

105. Qiu J, Qian X, Cui Q, et al (2012) Three-dimensional reconstruction and finite element modeling analysis of the rabbit optic nerve head in acute high intraocular pressure. Jpn J Appl Phys. https://doi.org/10.1143/JJAP.51.067001

106. Girard MJA, Beotra MR, Chin KS, et al (2016) In Vivo 3-Dimensional Strain Mapping of the Optic Nerve Head Following Intraocular Pressure Lowering by Trabeculectomy. Ophthalmology. https://doi.org/10.1016/j.ophtha.2016.02.008

107. Chiu SJ, Li XT, Nicholas P, et al (2010) Automatic segmentation of seven retinal layers in SDOCT images congruent with expert manual segmentation. Opt Express. https://doi.org/10.1364/oe.18.019413

108. Fabritius T, Makita S, Miura M, et al (2009) Automated segmentation of the macula by optical coherence tomography. Opt Express. https://doi.org/10.1364/oe.17.015659

109. Chen TC, Cense B, Pierce MC, et al (2005) Spectral domain optical coherence tomography ultra-high speed, ultra-high resolution ophthalmic imaging. Arch Ophthalmol. https://doi.org/10.1001/archopht.123.12.1715

110. Otsu N (1979) THRESHOLD SELECTION METHOD FROM GRAY-LEVEL

HISTOGRAMS. IEEE Trans Syst Man Cybern. https://doi.org/10.1109/tsmc.1979.4310076

111. Dijkstra EW (1959) A note on two problems in connexion with graphs. Numer Math. https://doi.org/10.1007/BF01386390

112. Shi J, Malik J (2000) Normalized cuts and image segmentation. IEEE Trans Pattern Anal Mach Intell. https://doi.org/10.1109/34.868688

113. Leung CKS, Liu S, Weinreb RN, et al (2011) Evaluation of retinal nerve fiber layer progression in glaucoma: A prospective analysis with neuroretinal rim and visual field progression. Ophthalmology. https://doi.org/10.1016/j.ophtha.2010.12.035

114. Kobatake H, Masutani Y (2017) Computational Anatomy Based on Whole Body Imaging: Basic Principles of Computer-Assisted Diagnosis and Therapy

115. Newson T, El-Sheikh A (2006) Mathematical modeling of the biomechanics of the lamina cribrosa under elevated intraocular pressures. J Biomech Eng 128:496–504. https://doi.org/10.1115/1.2205372

116. Sigal IA, Ethier CR (2009) Biomechanics of the optic nerve head. Exp. Eye Res.

117. Schwaner SA, Kight AM, Perry RN, et al (2018) A Methodology for Individual-Specific Modeling of Rat Optic Nerve Head Biomechanics in Glaucoma. J Biomech Eng 140:1–10. https://doi.org/10.1115/1.4039998

118. Morrison JC, Cepurna Ying Guo WO, Johnson EC (2011) Pathophysiology of human glaucomatous optic nerve damage: Insights from rodent models of glaucoma. Exp Eye Res 93:156–164. https://doi.org/10.1016/j.exer.2010.08.005

119. Pazos M, Yang H, Gardiner SK, et al (2015) Rat optic nerve head anatomy within 3D histomorphometric reconstructions of normal control eyes. Exp Eye Res 139:1–12.

https://doi.org/10.1016/j.exer.2015.05.011

120. Kim JS, Ishikawa H, Gabriele ML, et al (2010) Retinal nerve fiber layer thickness measurement comparability between time domain optical coherence tomography (OCT) and spectral domain OCT. Investig Ophthalmol Vis Sci 51:896–902. https://doi.org/10.1167/iovs.09-4110

121. Giani A, Deiro AP, Staurenghi G (2012) Repeatability and reproducibility of retinal thickness measurements with spectral-domain optical coherence tomography using different scan parameters. Retina 32:1007–1012. https://doi.org/10.1097/IAE.0b013e31822f5660

122. Matlach J, Wagner M, Malzahn U, Göbel W (2014) Repeatability of peripapillary retinal nerve fiber layer and inner retinal thickness among two spectral domain optical coherence tomography devices. Investig Ophthalmol Vis Sci 55:6536–6546. https://doi.org/10.1167/iovs.14-15072

123. Girard MJA, Strouthidis NG, Ross Ethier C, Mari JM (2011) Shadow removal and contrast enhancement in optical coherence tomography images of the human optic nerve head. Investig Ophthalmol Vis Sci. https://doi.org/10.1167/iovs.10-6925

124. Strouthidis NG, Grimm J, Williams GA, et al (2010) A comparison of optic nerve head morphology viewed by spectral domain optical coherence tomography and by serial histology. Investig Ophthalmol Vis Sci. https://doi.org/10.1167/iovs.09-3984

125. Girard MJA, Tun TA, Husain R, et al (2015) Lamina cribrosa visibility using optical coherence tomography: Comparison of devices and effects of image enhancement techniques. Investig Ophthalmol Vis Sci. https://doi.org/10.1167/iovs.14-14903

126. Brown R (2007) fitellipse.m

127. Sigal IA, Flanagan JG, Tertinegg I, Ethier CR (2009) Modeling individual-specific human optic nerve head biomechanics. Part I: IOP-induced deformations and influence of geometry. Biomech Model Mechanobiol 8:85–98. https://doi.org/10.1007/s10237-008-0120-7

128. Goetz CG (2007) Textbook of Clinical Neurology: Third Edition

129. Machiraju C, Phan A V., Pearsall AW, Madanagopal S (2006) Viscoelastic studies of human subscapularis tendon: Relaxation test and a Wiechert model. Comput Methods Programs Biomed 83:29–33. https://doi.org/10.1016/j.cmpb.2006.05.004

130. Eilaghi A, Flanagan JG, Simmons CA, Ethier CR (2010) Effects of scleral stiffness properties on optic nerve head biomechanics. Ann Biomed Eng. https://doi.org/10.1007/s10439-009-9879-7

131. Jin Y, Wang X, Zhang L, et al (2018) Modeling the origin of the ocular pulse and its impact on the optic nerve head. Investig Ophthalmol Vis Sci. https://doi.org/10.1167/iovs.17-23454

132. Norman RE, Flanagan JG, Sigal IA, et al (2011) Finite element modeling of the human sclera: Influence on optic nerve head biomechanics and connections with glaucoma. Exp Eye Res. https://doi.org/10.1016/j.exer.2010.09.014

133. Jin Y, Wang X, Irnadiastputri SFR, et al (2019) Effect of Changing Heart Rate and Body Posture on the Ocular Pulse Amplitude and Optic Nerve Head Deformations. Investig Ophthalmol Vis Sci 60:

134. Pijanka JK, Coudrillier B, Ziegler K, et al (2012) Quantitative mapping of collagen fiber orientation in non-glaucoma and glaucoma posterior human sclerae. Investig Ophthalmol Vis Sci. https://doi.org/10.1167/iovs.12-9705

135. Raykin J, Forte TE, Wang R, et al (2017) Characterization of the mechanical behavior of the optic nerve sheath and its role in spaceflight-induced ophthalmic changes. Biomech Model Mechanobiol. https://doi.org/10.1007/s10237-016-0800-7

136. Sigal IA, Yang H, Roberts MD, Downs JC (2010) Morphing methods to parameterize specimen-specific finite element model geometries. J Biomech. https://doi.org/10.1016/j.jbiomech.2009.08.036

137. Jolliffe IT (2002) Principal Component Analysis, Second Edition. Encycl Stat Behav Sci. https://doi.org/10.2307/1270093

138. Sarkalkan N, Weinans H, Zadpoor AA (2014) Statistical shape and appearance models of bones. Bone

139. Bischoff JE, Dai Y, Goodlett C, et al (2014) Incorporating population-level variability in orthopedic biomechanical analysis: A review. J Biomech Eng. https://doi.org/10.1115/1.4026258

140. Keustermans W, Huysmans T, Danckaers F, et al (2018) High quality statistical shape modelling of the human nasal cavity and applications. R Soc Open Sci. https://doi.org/10.1098/rsos.181558

141. Ciller C, De Zanet SI, Rüegsegger MB, et al (2015) Automatic segmentation of the eye in 3D magnetic resonance imaging: A novel statistical shape model for treatment planning of retinoblastoma. Int J Radiat Oncol Biol Phys. https://doi.org/10.1016/j.ijrobp.2015.02.056

142. C. Kharmyssov CK, M. W. L. Ko MWLK, J. R. Kim JRK (2019) Automated segmentation of optical coherence tomography images. Chinese Opt Lett. https://doi.org/10.3788/col201917.011701

143. Mari JM, Strouthidis NG, Park SC, Girard MJA (2013) Enhancement of lamina cribrosa visibility in optical coherence tomography images using adaptive compensation. Investig Ophthalmol Vis Sci. https://doi.org/10.1167/iovs.12-11327

144. Spoor CW, Veldpaus FE (1980) Rigid body motion calculated from spatial co-ordinates of markers. J Biomech. https://doi.org/10.1016/0021-9290(80)90020-2

145. Heimann T, Meinzer HP (2009) Statistical shape models for 3D medical image segmentation: A review. Med Image Anal. https://doi.org/10.1016/j.media.2009.05.004

146. Rasoulian A, Rohling R, Abolmaesumi P (2013) Lumbar spine segmentation using a statistical multi-vertebrae anatomical shape+pose model. IEEE Trans Med Imaging. https://doi.org/10.1109/TMI.2013.2268424

147. Styner MA, Rajamani KT, Nolte LP, et al (2003) Evaluation of 3D correspondence methods for model building. Inf Process Med Imaging. https://doi.org/10.1007/978-3-540-45087-0_6

148. Fitzpatrick CK, Baldwin MA, Laz PJ, et al (2011) Development of a statistical shape model of the patellofemoral joint for investigating relationships between shape and function. J Biomech. https://doi.org/10.1016/j.jbiomech.2011.06.025

149. Peloquin JM, Yoder JH, Jacobs NT, et al (2014) Human L3L4 intervertebral disc mean 3D shape, modes of variation, and their relationship to degeneration. J Biomech. https://doi.org/10.1016/j.jbiomech.2014.04.014

150. Rao C, Fitzpatrick CK, Rullkoetter PJ, et al (2013) A statistical finite element model of the knee accounting for shape and alignment variability. Med Eng Phys. https://doi.org/10.1016/j.medengphy.2013.03.021

151. Koenderink JJ, van Doorn AJ (1992) Surface shape and curvature scales. Image Vis

Comput. https://doi.org/10.1016/0262-8856(92)90076-F

152. Baldwin MA, Langenderfer JE, Rullkoetter PJ, Laz PJ (2010) Development of subject-specific and statistical shape models of the knee using an efficient segmentation and mesh-morphing approach. Comput Methods Programs Biomed. https://doi.org/10.1016/j.cmpb.2009.07.005

153. Sigal IA, Yang H, Roberts MD, Downs JC (2010) Morphing methods to parameterize specimen-specific finite element model geometries. J Biomech. https://doi.org/10.1016/j.jbiomech.2009.08.036

154. Feola AJ, Nelson ES, Myers J, et al (2018) The impact of choroidal swelling on optic nerve head deformation. Investig Ophthalmol Vis Sci. https://doi.org/10.1167/iovs.18-24463

155. Coudrillier B, Campbell IC, Read AT, et al (2016) Effects of peripapillary scleral stiffening on the deformation of the lamina cribrosa. Investig Ophthalmol Vis Sci. https://doi.org/10.1167/iovs.15-18193

156. Danford FL, Yan D, Dreier RA, et al (2013) Differences in the region- and depth-dependent microstructural organization in normal versus glaucomatous human posterior sclerae. Investig Ophthalmol Vis Sci. https://doi.org/10.1167/iovs.13-12262